HUMAN-ROBOT COLLABORATIVE MASTOIDECTOMY: COMBINING HUMAN PATH ADAPTATION WITH ROBOTIC ACCURACY

By

Patrick Smith Wellborn

Dissertation
Submitted to the Faculty of the
Graduate School of Vanderbilt University
in partial fulfillment of the requirements
for the degree of

DOCTOR OF PHILOSOPHY
in
Mechanical Engineering

January 31, 2021

Nashville, Tennessee

Approved:
Robert J. Webster III, Ph.D.
Robert F. Labadie, M.D., Ph.D.
Jason E. Mitchell, Ph.D.
Michael I. Miga, Ph.D.
Eric J. Barth, Ph.D.

ACKNOWLEDGEMENTS

The work in this dissertation was a collaborative effort and would not have been possible without the support, mentorship, and assistance from multiple people.

First and foremost, a huge thank you to my family for their unwavering support and encouragement throughout graduate school. Especially to my wife, Patricia, thank you for keeping me grounded and keeping me motivated. Even in the most stressful moments, your constant encouragement kept my spirits high and kept me on track to complete this dissertation.

I would like to thank my advisor, Bob Webster, for his consistent guidance throughout my time at Vanderbilt. Along with being a great researcher, Bob's genuine care both for me as a person and for my research helped bring about much of this work. I admire that no matter what he had going on, his door was always open, and he would make time to meet. Whether talking about goals or specific research, Bob gave valuable advice that elevated my work and helped me grow as a researcher.

I would also like to thank my entire dissertation committee: Bob Webster, Rob Labadie, Jason Mitchell, Mike Miga, and Eric Barth. Rob was extremely influential to my research and this work, and I'm lucky to have him as a second advisor as I worked in his Computer-Assisted Otologic Surgery (CAOS) lab. Despite being a practicing surgeon, Rob's clear passion for research and willingness to help in the lab brought a valuable medical perspective to this work. Jason was a joy to work with, and I learned a great deal from his expertise in mechanical design. Mike and Eric were two of the best instructors I have ever had. Not only did I learn a great deal from their classes, but their expertise in image-guidance and control, as well as their advice throughout the writing of this dissertation, helped elevate this work. Thank you all for your time, advice, and discussions which have enriched my entire graduate school experience.

I would like to thank the other students in both MED Lab and CAOS, who beyond being a great group of people to work with every day, were instrumental to the completion of this work. Neal Dillon was a great mentor to me when I first got to Vanderbilt and joined him in working on the Acoustic Neuroma Surgical Robot (ANSR) seen in Chapter 2. Thank you to Michael Siebold for the many late nights we spent to complete the cadaver bone drilling experiments in Chapter 2. To Trevor Bruns, Katy Riojas, Loris Fichera, and Miriam Smetak, thank you for making COAS a great place to work and for always being willing to give your advice and help when I needed it. Thank you to Max Emerson who helped me learn ROS for the control of the Cooperative Surgical Drill (CoSD) in Chapter 5. To the rest of the members of MED Lab that I had the pleasure to work with, including Ray Lathrop, Raul Wirz, Isuru Godage, Hunter Gilbert, Phil Swaney, Art Mahoney, Rich Hendrick, Josh Gafford, Andria Remirez, Patrick Anderson, Margaret Rox, James Ferguson, Tayfun Ertop, Bryn Pitt, Stephanie Amack, and Dom Ropella, thank you for making our lab such a welcoming and enjoyable place to work and collaborate.

Finally, I would like to thank the National Science Foundation and the National Institutes of Health for the research funding that gave me the freedom to complete this work.

TABLE OF CONTENTS

LIST OF TABLES

LIST OF FIGURES

Chapter 1

Introduction

The term “surgical robots” often conjures up the sci-fi images of an autonomous one-stop-shop robotic device for fixing all your surgical needs, such as that portrayed in Ridley Scott’s film, Prometheus. While portrayed as a futuristic development that would replace surgeons and perform any desired surgery, the reality of surgical robots in today’s world is 1) they often directly assist surgeons (rather than replace them) and give them extra capabilities to improve surgical outcomes, and 2) they are often good at operating on a certain part of the body, but one system cannot do everything.

The most popular and probably most well-known surgical “robot” being used clinically is the da Vinci Surgical System (Intuitive Surgical, Sunnyvale, CA, USA), which has been most successful in enhancing various minimally-invasive laparoscopic surgeries. Built as a generalized system that can address multiple different surgeries (most commonly for prostatectomies and increasingly for cardiac valve repair and gynecological procedures, among others), the da Vinci System is the closest surgical system to an all-in-one.

However, the da Vinci System is far from being able to do it all. Multiple other surgical robotic systems exist for performing specific surgeries, most notably in the fields of orthopaedics, neurosurgery, cardiac surgery, and endovascular surgery. The Mako system (Stryker Corp., Kalamazoo, MI, USA; acquired MAKO Surgical in 2013) and ROBODOC® Surgical System (THINK Surgical, Inc., Fremont, CA, USA; formerly Curexo Technology Corp.) assist with bone milling in knee and hip arthroplasty. In spine surgery, the Mazor X™ Stealth Edition (Medtronic, Minneapolis, Minnesota, USA; acquired Mazor Robotics in 2018) and ExcelsiusGPS® (Globus Medical Inc., Audubon, PA, USA) are used for image-guided, robotic placement of pedicle screws. The ROSA® Brain surgical robot (Zimmer Biomet Robotics, Montpellier, France; formerly Medtech SA) assists with a variety of neurosurgical procedures including Stereo Electroencephalography (SEEG), Deep Brain Stimulation (DBS), and stereotactic biopsy. The Monarch™ platform (Auris Health Inc., Redwood City, CA; acquired Hansen Medical in 2016 and is now owned by Johnson and Johnson) aims to bring visualization where it could not go before, namely to peripheral areas of the lungs with the use of robotic endoscope technology.

One field that is underrepresented, despite being inherently well-suited for robotic assistance, is otologic surgery and in particular temporal bone milling procedures such as a mastoidectomy. Even though there are orthopaedic systems, such as the Mako and ROBODOC® systems mentioned above, that use image-guidance to assist surgeons with bone milling, translation of this technology to temporal bone milling has not afforded a commercial device yet. Some obstacles that prevent direct translation of the existing orthopaedic bone drilling surgical robots to use in temporal bone milling is the significantly increased accuracy needed, the greater consequence of damage to vital anatomy, and the much smaller surgical workspace of the temporal bone compared to a femur or tibia. Human-robot collaboration could help bridge the gap for robotic-assisted milling in otologic surgery.

By combining the best of surgeons (excellent intraoperative judgment and ability to adapt to changing surgical conditions), and robots (capable of high accuracy, endurance, and repeatability), this dissertation presents two different approaches that converge towards a viable device for enhancing mastoidectomy. The first approach starts with an autonomous robot for mastoidectomy and gives it a human surgeon path adaptation by using a novel patient-specific algorithm. Conversely, the second approach starts with the surgeon, and using a completely passive, cooperative device, it gives the surgeon enhanced robotic accuracy. As determined through this work, the autonomous device is the best approach for a commercial device in the long-term due to its accuracy, newly informed path that takes into account patient variation just like a surgeon, and repeatability. However, clinical adoption of this technology is likely to take a long time. As the more immediate solution, the cooperative device that only augments the surgeon passively for increased accuracy has a quicker route to clinical adoption. Below, the clinical motivation for robot-assisted mastoidectomy is given, followed by the technologies that have come before and motivated this work. Lastly, the dissertation overview and contributions of this work towards a human-robot collaborative device for mastoidectomy are presented.

1.1 Surgical Overview and Challenges

Mastoidectomy, a common procedure in otologic surgery, is often performed to gain access to the middle and inner ear. It involves the removal of bone behind the ear in the mastoid region of the skull using a high-speed surgical drill, and it is performed either on its own for the treatment of disease and infection (e.g. mastoiditis or cholesteatoma) or as part of another procedure such as a translabyrthine approach for acoustic neuroma removal or a facial recess approach for cochlear implantation. Multiple vital anatomical structures are embedded within the mastoid bone, the most important of which include the facial nerve, which is responsible for facial movement, the chorda tympani nerve, which supplies the sense of taste to the tongue, the tegmen, which is the bone separating the brain from the inner ear, and the sigmoid sinus, which is a large blood vessel connecting to the jugular vein in the neck (see Figure 1.1). Since damage to any of these embedded structures can lead to morbidity and other severe complications (e.g. damage to the facial nerve results in facial paralysis), otologic surgeons must carefully mill away bone layer-by-layer. Requiring surgeons to uncover visual landmarks as they rely on auditory and tactile feedback to safely maneuver around the vital anatomical structures, the surgery can be difficult, time-consuming, and in some cases, overly invasive.

There are approximately 160,000 (extrapolating to the present time and accounting for both in- and outpatient procedures as well as cochlear implant data from company annual reports) mastoidectomies performed per year in the United States [5]. Given the precision and visualization challenges associated with mastoidectomy as well as long operating time

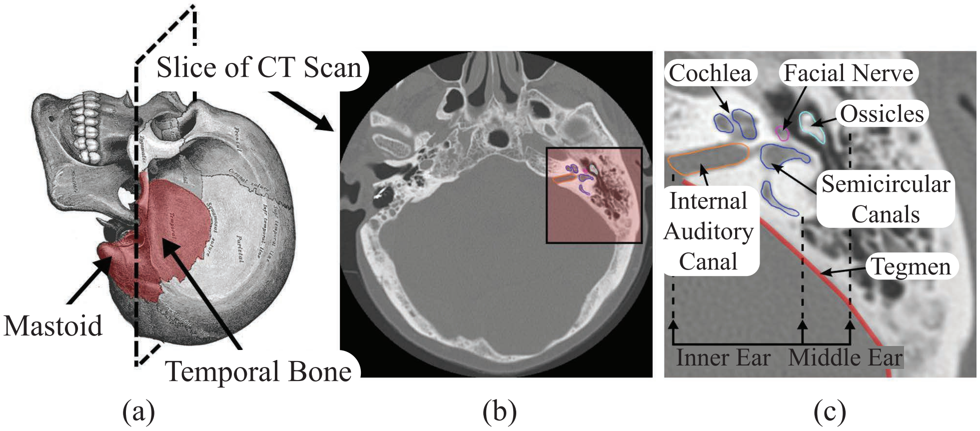

Figure 1.1: (a) The temporal bone and mastoid region of the skull, (b) a CT slice looking at the various segmented ear structures, and (c) the vital anatomical structures embedded within the mastoid bone.

in some cases, procedure efficiency and precision could benefit from both image-guidance and robotic assistance. One procedure that requires a particularly deep mastoidectomy, the translabyrinthine approach to vestibular schwannoma removal, is a good candidate for robotic assistance. Details of the procedure and the challenges associated with it are explained below.

1.1.1 Translabyrinthine Approach for Vestibular Schwannoma

A vestibular schwannoma (VS), also referred to as an acoustic neuroma (AN), is a benign and usually slow-growing tumor that develops on the vestibular nerve that leads from the internal auditory canal (IAC) to the brain (Figure 1.2). Tumors can become dangerous when they grow large since pressure from the tumor on the surrounding nerves and other structures can cause hearing loss, tinnitus, dizziness, and facial numbness or weakness, among other symptoms. Recently, the incidence of VS has risen, most likely due to advancements in imaging, increased access to imaging, and improved medical awareness of the disease [6, 7]. There are currently three treatment modalities for VS: observation and monitoring, radiotherapy, and surgery. Tumor size and symptoms determine which

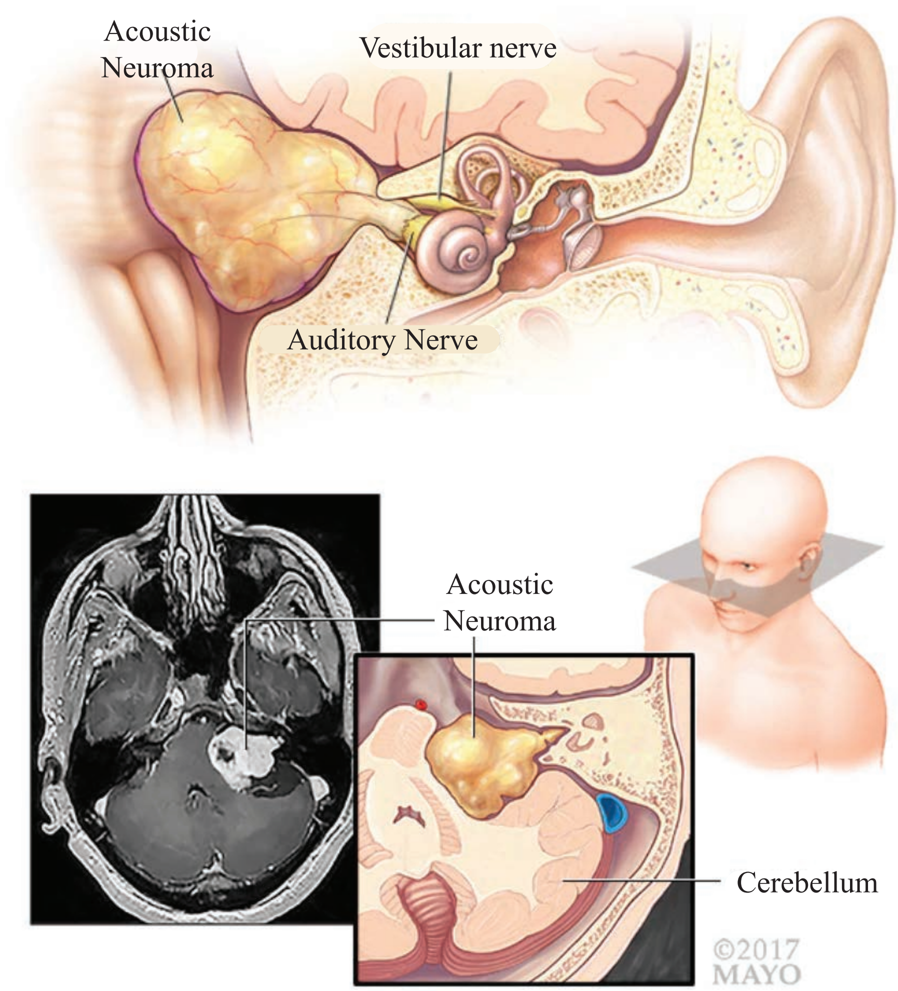

Figure 1.2: Depiction of an acoustic neuroma. It can be seen growing on the vestibular nerve extending from the inner ear into the brain (image from www.mayoclinic.org).

treatment option is best. For smaller tumors that are either not growing or growing slowly with few signs or symptoms, monitoring the tumor or radiotherapy may be best. However, larger tumors with multiple symptoms may require surgery to remove the tumor.

In the cases where the tumor is large, radiotherapy is not effective, or the tumor causes extreme discomfort to the patient, surgery is needed. The translabyrinthine approach is a common surgical procedure for VS removal, and it requires a deep mastoidectomy through the mastoid and labyrinth. Compared to other approaches, such as the middle fossa or retrosigmoid approach which require brain retraction, the majority of the translabryinthine approach is extradural and brain retraction is avoided. This lessens any chance of brain injury, but sacrifices any hearing, therefore, this approach is ideal for resecting any size tumor when patient hearing is poor or for when the chance of hearing preservation is low [8].

The translabyrinthine approach requires extensive bone milling to reach the IAC and access the tumor. Both the mastoid and the labyrinth are milled away and the bone covering the IAC and posterior fossa (cranial bone separating the inner ear from the brain) is thinned to the thickness of an eggshell, called skeletonization. This allows the surgeon to manually remove the remaining skeletonized bone and access the IAC, so that the tumor may be delicately separated and removed from the nerves [8]. Milling through the mastoid and labyrinth may take several hours due to the embedded vital anatomy (e.g. facial nerve).

1.1.2 Technical Challenges and Motivation

Mastoidectomy is a challenging procedure due to the precision requirements, the lack of visualization until vital structures are uncovered, the severe consequences if any vital structures are damaged, and in some cases, the long amount of drilling time required (see the translabyrinthine approach to vestibular schwannoma removal surgery above). On top of this, anatomic variability of the temporal bone among different patients requires surgeons to adapt and search for vital anatomical structures within the bone before proceeding safely through the procedure [9]. It is hypothesized that image-guidance and robotics could aid surgeons in performing mastoidectomies by decreasing invasiveness, shortening operating time, and/or reducing complications.

There are two approaches to a robotic surgical system that utilizes image-guidance for mastoidectomy: automated and cooperative, each with its own advantages to aid surgeons during this procedure. For the automated approach, the robotic system performs the surgery automatically based on a preoperative plan defined by the surgeon and is overseen by the surgeon during the procedure without direct contact. To create the preoperative plan, the surgeon uses a preoperative computed tomography (CT) scan, defines the boundaries to be drilled away, and segments the vital anatomical structures to not be drilled. Robotic automation is ideal for cases such as the translabyrinthine approach, where drilling requires great precision and takes multiple hours to complete before the more delicate portion of the surgery, the tumor removal from the vestibular nerve, can be done. Due to the precision required along with hours of drilling, mastoidectomy has been shown to impose a significant cognitive load on surgeons [10]. Given that the most delicate portion of the surgery, the tumor resection, occurs when the surgeon may be mentally fatigued, there is a heightened risk of injury during this stage. An automated robotic approach to remove a bulk of the bone in order to save the surgeon for the more delicate task of tumor resection could prove to be significantly beneficial to patient safety and surgical outcome. Additionally, the patient could benefit from reduced invasiveness and potentially faster operative times. Since the location of vital anatomy is known, the robotic system will not drill any bone outside the preoperative plan and can speed up its motions in areas where the risk of damage to vital anatomy is low.

Alternatively, for a cooperative approach, the robotic system and surgeon collaboratively hold the drill and the surgeon manually drills as normal. Again, image-guidance from a preoperative plan is implemented to both give the surgeon additional anatomical information while drilling (i.e. instead of solely relying on uncovering vital anatomical features to avoid them, information of the subsurface anatomy is readily available to the surgeon during the surgery) and as a safety mechanism. Since the robotic system cooperatively holds the drill and has preoperative knowledge of the underlying vital anatomy, the robot can create boundaries and stop the motion of the drill before hitting vital anatomical structures (e.g. the facial nerve) or before going beyond the predefined surgical boundaries. A robotic system with cooperative control is beneficial since it gives manual control back to the surgeon to perform the surgery as usual, but it will stop motion in the case that the drill gets too close to something that should not be drilled. Thus, while operating time may be the same, it has the potential for increased safety, reduced complications, and decreased invasiveness as only the necessary bone is removed.

Despite the potential benefits outlined above, robotic systems for temporal bone milling have lagged behind similar bone milling surgeries in orthopaedics and neurosurgery. This is likely due to the aforementioned greater accuracy requirements and severe consequences of damage to vital anatomy that is inherent to operating on the temporal bone. Therefore, for translation of robotic surgical milling to otologic surgery, greater accuracy through robotic design and more work to increase the safety of automated approaches must be done.

1.2 Image-Guided and Robotic Approaches to Surgical Drilling

Most of the prior robotic systems which have inspired the progression of robotic bone drilling and milling, and consequently the work in this dissertation, can be categorized as surgical CAD/CAM (Computer Assisted Design and Computer-Assisted Manufacturing) systems [11]. As a subset of medical robots, these CAD/CAM systems execute a plan based on preoperative imaging and modeling in a manner analogous to computer-integrated manufacturing. Some of the earliest research within CAD/CAM systems include robot-assisted orthopaedic bone milling for knee and hip arthroplasty [12, 13, 14, 15, 16, 17], bone drilling for pedicle screw placement in spine surgery [18], and stereotactic neurosurgery [19]. More recently, many of these orthopaedic surgical robots have received regulatory approval and are currently in clinical use: the Mako system (Stryker Corp., Kalamazoo, MI, USA; acquired MAKO Surgical in 2013), ROBODOC® Surgical System (THINK Surgical, Inc., Fremont, CA, USA; formerly Curexo Technology Corp.), the Mazor X™ Stealth Edition (Medtronic, Minneapolis, Minnesota, USA; acquired Mazor Robotics in 2018), and ExcelsiusGPS® (Globus Medical Inc., Audubon, PA, USA). Figure 1.3 shows the ROBODOC® Surgical System and the Mako system.

Due to the rigidity of bone and the great contrast between bone and tissue within a CT scan, a preoperative plan of the surgical task can be made with minimal risk of tissue defor-

(a) (b)

Figure 1.3: Two orthopaedic, robot-assisted bone milling systems that are in clinical use today. Both of these systems are used to perform total knee and hip arthroplasty. (a) shows the ROBODOC® Surgical System (THINK Surgical, Inc., Fremont, CA, USA), which mills the bone automatically according to a preoperative plan. (b) depicts the Mako system (Stryker Corp., Kalamazoo, MI, USA), which is a cooperative bone-milling system that imparts active constraints to the drill position to keep it within a predefined area.

mation during surgery. Robot-assisted orthopaedic bone milling can mill a more accurate cavity for the implant to be placed, which leads to better implant fixation [16]. Also, the use of a robot-assisted system in knee arthroplasty is shown to have better alignment compared with conventional surgery. This improves the positioning of the prosthesis and ultimately leads to improvement in joint performance [20].

Given the technical similarities of milling and drilling bone in different parts of the body, a logical extension would be to use similar systems to the robot-assisted orthopaedic systems in otologic surgery. However, due to the aforementioned technical challenges associated with temporal bone milling, translation of these prior technologies is difficult and necessitates more research to realize robot-assisted otologic surgery.

1.2.1 Robotic Mastoidectomy

Robot-assisted temporal bone milling has been a growing research focus for many groups in recent years. Looking specifically at robotic mastoidectomy, there are three different types of robotic systems: active systems, semi-active systems, and passive systems. The active system refers to a robotic structure that utilizes motors for actuated movement in a completely automated device. The semi-active and passive systems are both cooperatively-controlled manual devices, with the difference between them being the actuator used. The semi-active system uses motors in its design to actively inhibit drill motion against the surgeons intended motion (creating virtual fixtures or "no-fly zones"), while the passive system uses brakes or other devices that can solely inhibit motion, not impart any motion of their own, to accomplish the same task.

With these three different robotic approaches in mind, the earliest research of robot-assisted temporal bone milling utilized a robot arm for automated drilling based on pre-planned trajectories. Federspil et al. were the first group to use an industrial robot holding


(a) (b)

Figure 1.4: (a) Force-controlled robot for milling a cavity in temporal bone for a CI receiver (developed by Federspil et al.) with an inset showing closeup of the surgical drill end-effector and force sensor. (b) The milled out cavity with the CI receiver placed into it (images from [1]).

a surgical drill to mill on otologic bone (Figure 1.4) [1]. The target of this research was to mill out a pocket of bone for implantation of a cochlear implant (CI) receiver using force feedback to control the speed of the drill. Along with this, they researched how different milling path parameters (depth of cut and vertical vs. horizontal milling paths) affected the forces imparted on the drill and the speed to complete the drilling.

After the feasibility of robotic otologic bone milling shown by Federspil et al., many research groups proposed and tested robotic mastoidectomy. Compared to milling a shallow pocket of bone for a CI receiver, performing a mastoidectomy is a significantly more challenging task. The drill must come into very close proximity with vital anatomy (e.g. the facial nerve) embedded in the mastoid bone, and the milling cavity for each patient is unique based on their specific anatomy. Danilchenko et al. performed the first robotic mastoidectomy using an image-guided industrial robotic arm to mill a cavity in cadaveric temporal bone (Figure 1.5) [2]. To align the robot to the temporal bone specimen, three markers were implanted into the temporal bone and a CT scan was taken. An optically tracked probe was used to register the markers in physical space to the markers in the CT image. In addition, three optically tracked coordinate frames were attached to the robot base, the tool, and the patient, respectively, to track the movement of the robot relative to the bone in real-time. Thus, the target anatomy could be represented relative to the robot throughout the procedure. Limitations of this approach include the large size of the industrial robot compared to the small workspace needed for performing a mastoidectomy. This design would take up a large space in the OR, block close visualization of the surgical site due to its size, and would be difficult to monitor. Also, it relies on image-guidance to maintain accuracy and is subject to tracking errors as well as registration errors, which would make the submillimetric accuracy necessary for a mastoidectomy difficult or nearly impossible to achieve.

In addition to the early robotic mastoidectomy approaches that used active systems, recently there has been a growing interest in semi-active [21, 3, 22] or passive systems for cooperative control [23]. Lim et al. developed a cooperative 5 degree of freedom (DOF) robot that has five motors, three of which drive a 3-axis linear stage for positioning, and the remaining two control two rotational axes of the drill end-effector [3]. Designed to be semi-active, the robot uses a force-torque sensor attached to the drill to employ admittance control. This means that the forces imparted on the drill from the surgeon intending to move it are translated to joint velocities on the robot, such that the robot freely moves in the direction the surgeon moves it. With an optical marker coordinate frame attached to the drill, image-guidance is employed so that when the drill reaches a forbidden area (virtual fixture), the actuators will actively block drill motion.

A similar design by Olds et al. seeks to be a more general surgical robotic system for head and neck surgery [22]. Just like the cooperative robot by Lim et al., it is a 5-DOF semi-active, cooperative robot that utilizes a force/torque sensor attached to the drill for admittance control. While it similarly decouples linear positioning from the rotation of the end-effector, the design by Olds et al. uses a linear delta stage with preloaded components

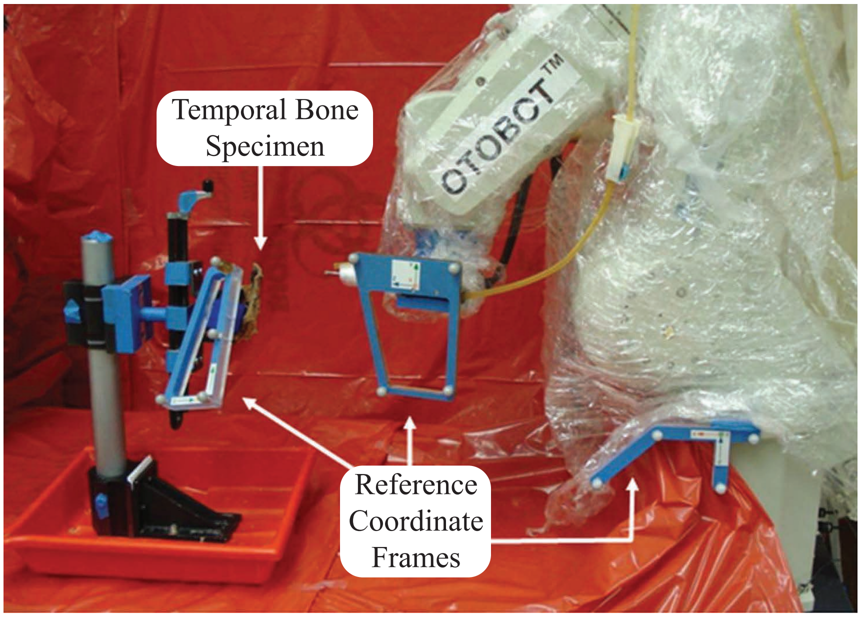

Figure 1.5: Experimental setup of the OTOBOT to perform mastoidectomy on a temporal bone specimen. Coordinate frames with optical tracking markers are placed on the robot base, robot end-effector, and bone specimen for motion tracking (images from [2]).

and no gearheads to minimize backlash. This results in a stiff design for high accuracy.

While these cooperative approaches are all smaller than the automated industrial robotic approach described above, they still all rely on image-guidance for operation and have the same accuracy limitations associated with tracking and registration error. The cooperative approach described in Chapter 4 is designed to be bone-attached to eliminate image-guidance as a source of error.

1.2.2 Bone-Attached Robotic Systems

Despite improvements in surgical navigation technology, which have decreased localization error of tracked markers to under a millimeter, the tracking and alignment inherently add some level of error to the surgical system. Additionally, tracking systems increase the complexity and cost of any image-guided surgical robot. As an alternative, bone-attached robots can be used, especially when submillimetric accuracy is required. By rigidly affixing the robot to the patient, there is minimal relative motion and, thus, no need to track the robot throughout the procedure (other than for a redundant safety check). If bone-implanted fiducial markers that also serve as attachment points for the robot are inserted before the

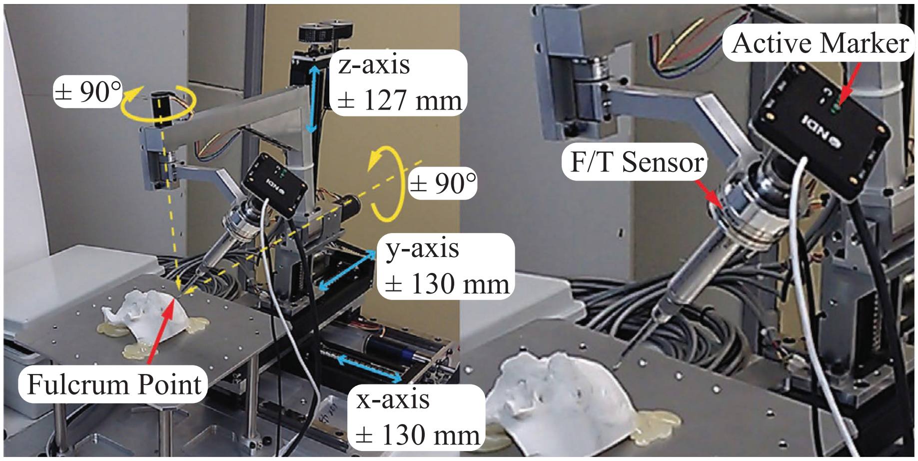

Figure 1.6: Design of a 5 degree of freedom cooperative robot for mastoidectomy. A force sensor attached to the drill allows for admittance control, so that when the surgeon applies force to the drill, the motors move the drill in the intended direction (images from [3]).

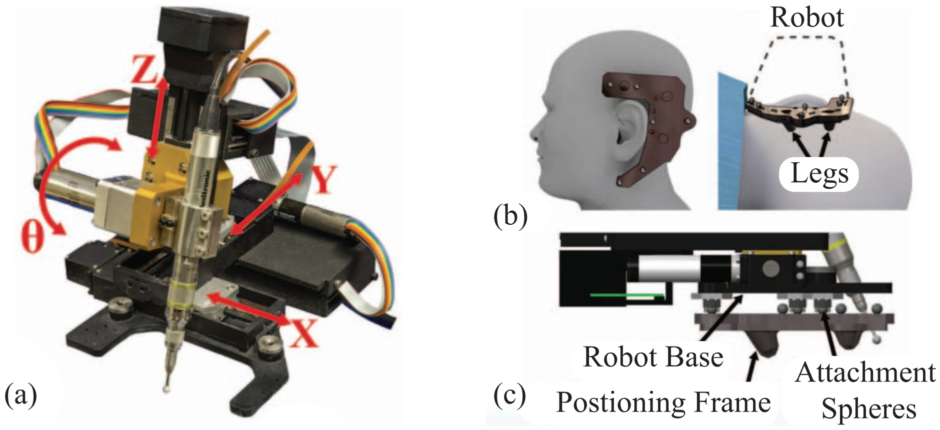

Figure 1.7: (a) The Acoustic Neuroma Surgical Robot (ANSR), with each of its joints labeled in red. (b) The positioning frame used for both registration and for the attachment of ANSR. (c) View of how ANSR attaches to the positioning frame (images from [4]).

pre- or intra-operative image acquisition, the robot can be aligned directly to the image according to the locations of these attachment points with a simple rigid registration.

Prior work using bone-attached robots has shown them to be capable of milling bone in orthopaedic surgery [24, 25, 26], as well as aligning a drill for minimally invasive pedicle screw placement for spinal surgery [27, 18]. Shoham et al. show that their MiniAture Robot for Surgery (MARS, which is the precursor to Mazor's Renaissance robot), a bone-attached 6 degree of freedom parallel platform, is capable of placing pedicle screws with high accuracy (mean placement error of 0.2 mm) [18]. More recently, bone-attached robots have been used as adjustable stereotactic frames for minimally invasive cochlear implantation surgery [28, 29].

Of particular interest is a bone-attached robot for automated mastoidectomy developed by Dillon et al., as this is the system that the patient-specific trajectory planning algorithm detailed in Chapter 2 is tested on [30]. Coined the Acoustic Neuroma Surgical Robot (ANSR), this system is a 4-DOF robot with three translational DOF and one rotational DOF (Figure 1.7). ANSR was tested on human cadaver heads to show that it could safely remove the bulk of bone during a translabyrinthine approach to acoustic neuroma removal [4]. Although it has the accuracy advantage of being a compact, bone-attached design, ANSR still requires much more testing to be used clinically. A step in this direction is to ensure the safety of the system and reduce the risk of injury to vital structures. A new algorithm in Chapter 2 programs ANSR to drill with human surgeon technique, and it is shown to reduce forces below a threshold that could damage vital structures, such as the facial nerve.

1.3 Dissertation Overview and Contributions

Despite the benefits in accuracy and patient outcomes seen for robot-assisted bone milling systems in orthopaedics [20], translation of similar devices for temporal bone milling have lagged behind, and there are currently no clinical devices available. This is likely due to the aforementioned greater accuracy requirements, severe consequences of damage to vital anatomy that is inherent to operating on the temporal bone, and much smaller workspace of the mastoid region of the temporal bone compared to a femur or tibia. A possible solution to the translation of robot-assisted drilling technology to otologic surgery is human-robot collaboration.

The purpose of the work described in this dissertation is to combine the best aspects of surgeons and robots in a collaborative system aimed at enhancing mastoidectomy. Surgeons, through years of education, training, and countless repetitions of procedures, have excellent intraoperative judgment and the ability to adapt to changing conditions during surgery. Alternatively, robots are capable of high precision, accuracy, endurance, and repeatability, and they have the capacity to integrate various imaging and sensing modalities into the execution of the surgical task. With the ultimate goal of a combined system with the ability to adapt to the procedure on-the-fly for improved mastoidectomy, this dissertation presents two approaches that converge on this objective.

The first approach starts with an automated robot for mastoidectomy and gives it a human surgeon path adaptation by using a novel patient-specific algorithm. The second approach starts with the surgeon, and using a completely passive, cooperative device, it gives the surgeon enhanced robotic accuracy. As determined through this work, the automated device is the best approach for a commercial device in the long-term due to its accuracy, newly informed path that takes into account patient variation just like a surgeon, and repeatability. However, clinical adoption of this technology is likely to take a long time. As the more immediate solution, the cooperative device that only augments the surgeon passively for increased accuracy has a quicker route to clinical adoption.

1.3.1 Making Robots Mill More Like Human Surgeons

Looking first at the automated approach, the main goal in Chapter 2 is to make the acoustic neuroma surgical robot (ANSR) mill more like a human surgeon and less like an industrial computer numeric controlled (CNC) machine. Automated approaches for mastoidectomy to date use constant speed, CNC-type paths, which can lead to higher cutting forces than a surgeon would impart, especially near vital anatomical structures [1, 2, 30]. Several methods have been previously proposed for incorporating variations in bone density in the planning and/or control of bone drilling and milling. In orthopaedic bone milling, Sugita et al. used a control scheme that took into account transitions between different bone types (cortical and cancellous) and air to reduce procedure time and minimize force spikes [31] Using force-based control along with knowledge of typical force levels in different parts of the vertebrae, Wang et al. were able to avoid drill penetration beyond the targeted bone [32]. Specific to otologic surgery, Williamson et al. used the relationship between drilling force and bone density to predict the pose of a robot-controlled drill based on density estimates gathered from preoperative images and real-time force measurements [33].

Specific contributions of this work include a new trajectory planning algorithm based on patient-specific CT scan data to reduce forces in the direction of vital anatomical structures. Image-based density estimates, locations of vital anatomy, and force modeling are used to optimize tool orientation and velocity. Experiments in both phantom bone models and cadaver temporal bone demonstrate that the proposed algorithm reduces mean and peak forces near vital structures.

1.3.2 Giving Surgeons Robotic Precision and Augmenting Spatial Awareness

While the automated approach in Chapter 2 provides many benefits (e.g. increased repeatability, increased accuracy, decreased chance of damage to vital anatomy, the potential to decrease procedure time) that make it the best solution for the long run, clinical adoption of this technology is likely to take a long time. Given the surgery is currently performed manually, an automated approach that takes the drill out of the surgeon's hand will face a high barrier to clinical adoption. Additionally, regulatory pathways for an automated approach face higher scrutiny. For this reason, a cooperative approach is presented that has the potential for quicker clinical adoption.

Looking at the second approach in Chapters 3 and 4, the overarching goal is to give an otologic surgeon enhanced precision and intraoperative image-guidance through an inherently safe, collaborative milling robot. Like ANSR, in Chapter 2, this robot is designed to be bone-attached, so that tracking error can be eliminated for increased robotic system accuracy. Additionally, to ensure the inherent safety of the system, the robot is designed to be completely passive utilizing brakes at each joint, eliminating any risk of errant motion from actuators such as motors. This approach proves to be the more immediate of the two approaches for a quicker route to clinical adoption.

In Chapter 3, to enable this robotic design, we develop a new miniature magnetorheological (MR) brake design with high braking torque and fast response time. For the robot to be bone-attached, a small and lightweight brake is necessary, and it needs to be powerful enough to overcome the surgeon's drill motion as well as not hinder the surgical workspace with its size. With no commercially available brake fitting these specifications, we develop a new brake, choosing an MR-type for its superior torque-to-mass ratio and controllability.

Contributions of Chapter 3 include a new miniature MR brake design that has the fastest time constant and highest torque-to-mass ratio compared to other similarly-sized

MR brakes in the literature.

A few research groups have developed collaborative robots for mastoidectomy, with two groups using semi-active serial robots to actively implement virtual fixtures [22, 3] and one group using a passive serial robotic arm to stop drill motion from damaging vital anatomy [23]. Another group simply augmented a surgical drill to turn off when it got too close to vital structures [34]. All four of these systems require active optical tracking of the surgical drill and the patient to accomplish this. Tracking errors from the optical tracking add to inherent robot compliance errors making it difficult to achieve the submillimetric accuracy required for mastoidectomy. A master-slave system, which aims to combine the best of robotic precision to surgical technique, is another consideration for improving mastoidectomy. A group using the da Vinci Surgical System proved the feasibility of this system to perform a mastoidectomy. However, they remarked the lack of haptic feedback to the surgeon was a major drawback and the procedure time increased significantly [35].

The contributions of Chapter 4 include the design of an inherently safe device to improve the safety and accuracy of mastoidectomy. This design highlights the first instance of a bone-attached cooperative milling robot for mastoidectomy, and the core kinematic unit, a five-bar linkage mechanism, has been developed for testing and feasibility of the design.

Chapter 2

Patient-Specific Planning for Mastoidectomy

2.1 Chapter Overview

Human-robot collaboration has the potential to improve mastoidectomy, and one approach is to give an automated bone-milling robot the ability to mill bone more like a surgeon and adapt to specific patient anatomy. The work in Chapter 2 improves the milling plan of an automated approach to robotic mastoidectomy by incorporating novel, patient-specific algorithms. By incorporating both force modeling and proximity to vital anatomy, this algorithm reduces forces towards vital structures by controlling both the speed and incident angle of the surgical drill. Experimentation was done in both phantom test blocks and cadaver temporal bone. Portions of this work were published in the 2016 IEEE/RSJ International Conference on Intelligent Robots and Systems (IROS) [36].

2.2 Introduction

The motivation for the planning algorithm discussed in Chapter 2 comes from how surgeons actually mill bone during mastoidectomy. To most efficiently mill the porous mastoid bone, surgeons constantly adjust their speed and tool incidence angle, preferring to use the side of the spherical cutting burr as much as possible. It has been experimentally shown that cutting with the distal tip leads to higher maximum forces, which is undesirable [37]. Additionally, surgeons adjust their accuracy requirements, such as speed and depth of cut, when in close proximity to vital structures like nerves and blood vessels to limit the risk of damage (see Figure 2.1a).

On the other hand, robots are usually programmed to mill bone like an industrial Computer Numeric Control (CNC) milling machine, which typically operates at a constant velocity and cut depth. This approach does not take into account bone variability, which is especially prevalent in the highly porous mastoid bone (see Figure 2.1b). Both size and frequency of air cells within the mastoid bone is highly variable between patients, and the density of the bone can vary spatially for each patient. Based on these inter- and intra-patient bone variations, a trajectory planning algorithm is detailed in Chapter 2 to create a patient-specific path plan. The plan takes into account bone density as well as proximity to vital anatomical structures through the use of preoperative CT scans and force modeling. As opposed to the constant velocity of the CNC milling strategy, this plan speeds up the milling in less dense bone and when the drill is not close to vital anatomy and preferentially chooses to cut with the side of the milling burr for more efficiency. When the drill approaches vital structures, both drill incidence angle and speed are chosen such that forces are minimized in the direction of that structure. This reduces the risk that the robot will deflect in that direction and damage the structure.

Several methods have been previously proposed for incorporating bone density variations into the planning and/or control of robotic bone drilling and milling. Sugita et al. employed a control scheme that accounted for the transitions between different bone types (cortical and cancellous) and air for reduction of procedure time and minimization of large force spikes in orthopaedic bone milling [31]. Wang et al. used force-based control and knowledge of typical force levels in different areas of the vertebrae to avoid drill penetration beyond the targeted bone and damage to nerves [32]. In the field of otologic surgery, Williamson et al. used the correlation between drilling force and bone density to predict the pose of a robot-controlled drill based on density estimates from the pre-operative images and real-time force measurements [33]. Additionally, forces in otologic bone milling have been modeled in the development of a physics-based haptic simulator [38]. The voxelized model developed in [38] is used in the present work to adjust the cutting tool orientation and velocity along the trajectory for automated temporal bone milling such that the forces are decreased when the tool is in close proximity to vital anatomy and the tool is oriented for improved cutting efficiency.

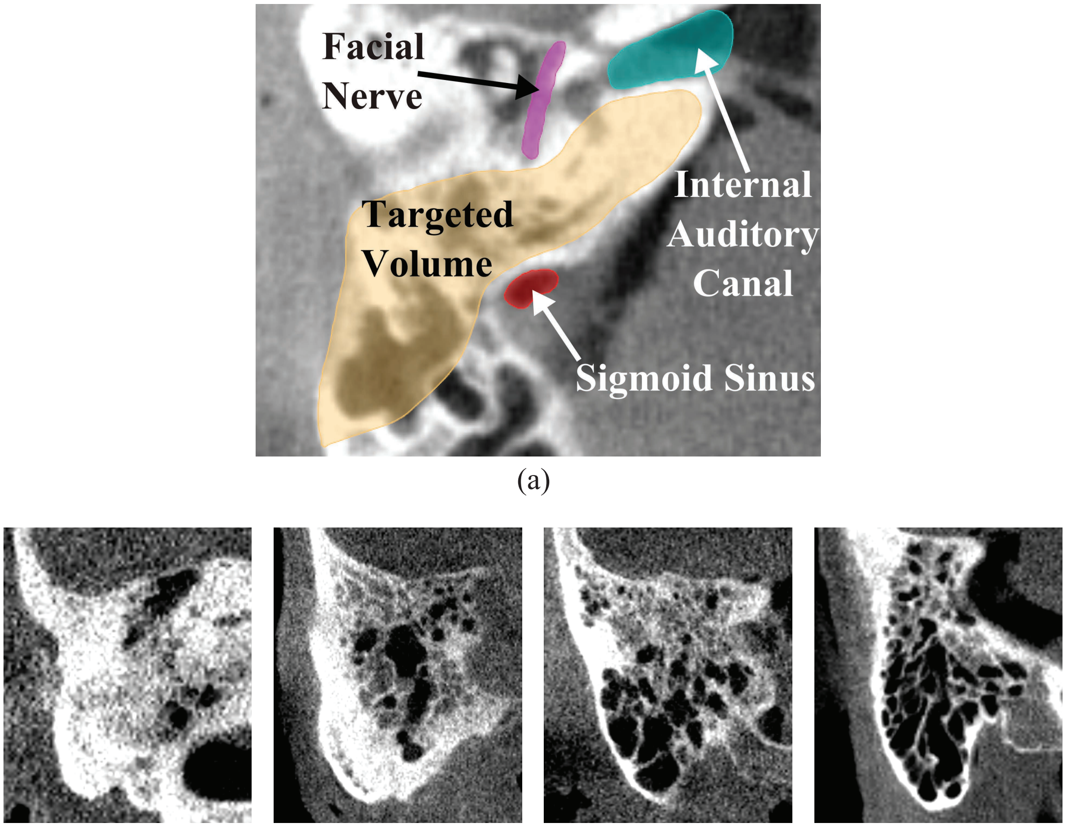

(a)

(b)

Figure 2.1: (a) A slice of a computed tomography (CT) scan of the temporal bone region. Both the target and vital anatomy that must be avoided are illustrated. Note the pneumatization, or presence of air cells, within the targeted bone volume to be removed. (b) Temporal bone CT scans of several patients. Note the inter- and intra-patient variation of pneumatization. Here, the inter-patient pneumatization increases from left to right.

During a mastoidectomy, it is common for surgeons to drill within very close proximity to vital anatomical structures, most notably, the facial nerve. Often the facial nerve is surgically skeletonized during the procedure, meaning the bone surrounding it is thinned within a millimeter or less (surgeons refer to this as “eggshelling”), either for access to other structures, to positively identify the course of the nerve, or to remove all infected tissue [8]. This requires expert accuracy by the surgeon to avoid injury to the facial nerve; the incidence of injury has been cited to be from 1% to 4% in primary otologic procedures, and as high as 4% to 10% in revision procedures [39]. Through experimentation in this work, it was determined that a small 0.3 N force by a surgical drill rotating at 20,000 rpm was enough to break through the surgically skeletonized bone surrounding the facial nerve and damage it. Therefore, for a robotic approach to be safe, it must reduce forces below this threshold when in close proximity to the facial nerve. With a new patient-specific algorithm, which incorporates both force modeling and proximity to vital anatomy, the automated robotic approach described in this chapter shows reduced maximum forces overall and reduced forces toward the facial nerve below the breakthrough threshold.

2.3 Patient-Specific Motion Planning

2.3.1 Cartesian Path

The first step in the planning procedure is to generate a three-dimensional milling path through the bone that covers as much of the target volume as possible without crossing into untargeted regions (bone that need not be removed, or other anatomy). The output of this portion of the planning procedure is a list of N target points in the image coordinate frame. The only restriction on this path is that the current target point is reachable by the cutting burr and not beneath unmilled bone (i.e. target points 1 to i-1 must provide access to point i for the drill). This path can be calculated using a number of approaches, including a simple "lawnmower" approach (see e.g. [1, 31]), contour parallel tool paths [40], etc. Given this tool path, the remainder of Chapter 2 focuses on selecting the tool orientation and cutting velocity using patient-specific data.

For each step along the 3D path, a range of permissible drill orientations can be calculated. This is done by examining the volume of bone previously removed in proximity to the point under consideration. Any shaft orientation that reaches the point, without colliding with unmilled bone, is considered a permissible orientation. Since the cutting burr is constantly rotating about its axis, only two orientation angles must be considered: ϕ and θ (see Figure 2.2).

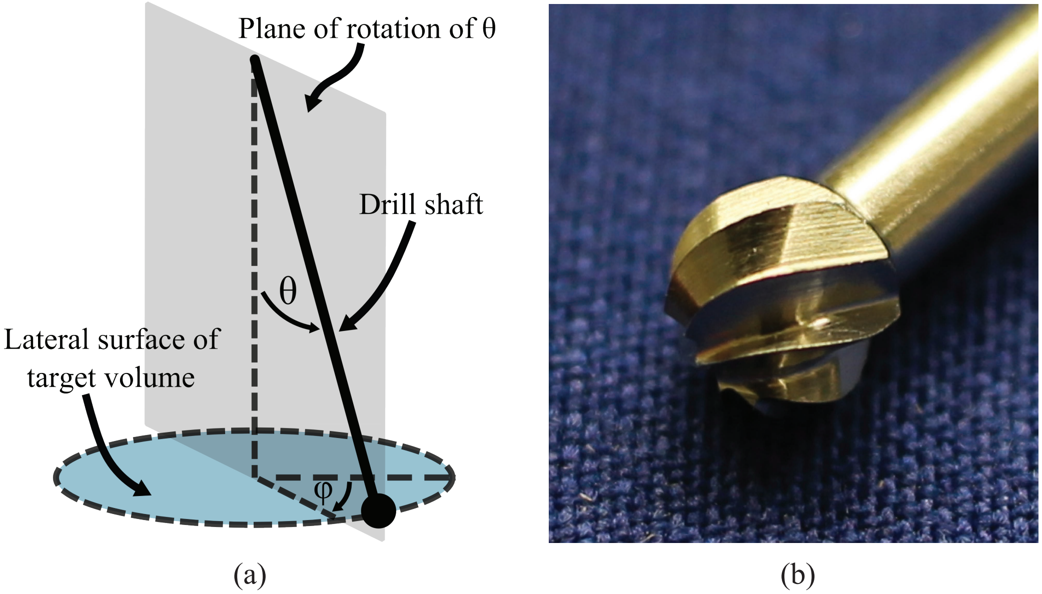

(a) (b)

Figure 2.2: (a) Orientation angles of surgical drill with respect to bone surface. Since the drill rotates continuously, only two angles must be considered: θ and ϕ; (b) Photograph of fluted cutting burr for otologic surgery.

2.3.2 Efficient Cutting Angle

Surgical cutting burrs are typically spherical in shape with either a fluted or diamond-coated surface. Due to its shape, the side of the burr (i.e. near its equator) cuts more efficiently than the distal tip. In a study evaluating the forces during milling of the temporal bone, large force spikes (well beyond the mean forces for the parameters) were observed for spherical otologic burrs when primarily cutting with the distal tip [37]. In clinical practice, surgeons use the side of the burr whenever possible to increase cutting efficiency. As a simple metric for quantifying the amount of bone being cut with the side of the burr compared to the tip of the burr, the following quantity can be used:

$$I = \sum_{i=1}^{n} \rho_i V_i d_i^2 = \sum_{i=1}^{n} \rho_i V_i (r^2 - z_i^2), \tag{2.1}$$

where $i = 1...n$ represents all of the voxels that are at least partially covered by the cutting burr, ρ_i is the voxel density, V_i represents the partial volume of a given voxel, and d_i is

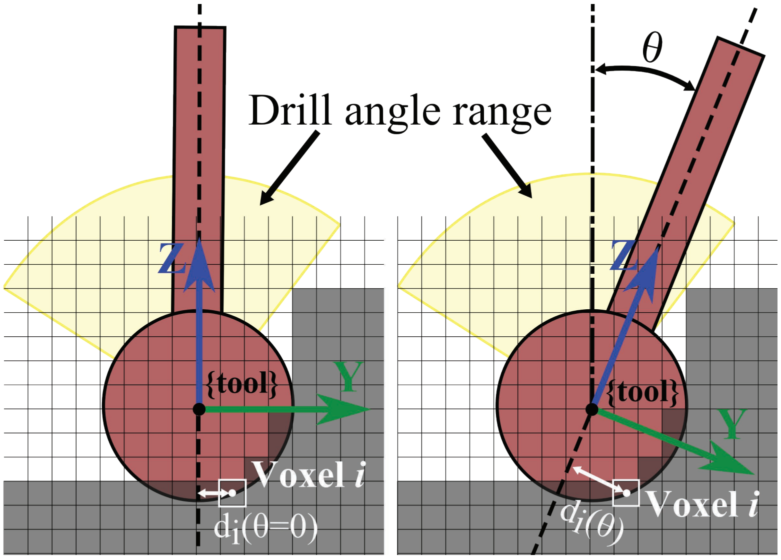

(a) (b)

Figure 2.3: Cross-sectional illustration of the range of permissible angles at a given point along the path. Optimal shaft angle (θ) is determined based on the intensity and location of each voxel with respect to the drill shaft (d_i). Note that d_i also has a component in the x-direction in the 3D case and all of the voxels being cut are at the surface of the spherical burr. The figure shows how the distance between the shaft axis and the center of a single voxel changes with θ.

the perpendicular distance from the shaft axis to the center of the voxel. The rightmost expression in (2.1) gives d_i^2 in terms of the radius of the burr, r, and the z-coordinate of the voxel, z_i, in the tool coordinate frame shown in Figure 2.3. Density is estimated based on the intensity of the voxel in the pre-operative CT scan. For different shaft orientations, the density and partial volume remain the same while d_i varies (see Figure 2.3). I is maximized when the side of the burr is removing the largest quantity of bone possible. To account for varying quantity of bone along the path, I can be normalized based on the total amount of bone (calculated based on volume of voxel covered by the burr and intensity in image) that is to be removed at the given step:

$$I_n = \frac{\sum_{i=1}^{n} \rho_i V_i (r^2 - z_i^2)}{\sum_{i=1}^{n} \rho_i V_i r^2}, \tag{2.2}$$

which gives a value between 0 and 1. The normalization keeps the magnitude of this component of the orientation calculation in the same range for all points so the contribution of this component is consistent throughout the trajectory.

2.3.3 Reducing Forces Near Vital Anatomy

The orientation of the burr also influences the magnitude and the direction of the cutting force between the burr and the bone. This is particularly true for spherical surgical burrs and non-homogeneous bone, where there can be considerable differences in cutting force direction with orientation change. When milling near vital anatomical structures in the temporal bone (e.g. the facial nerve), it is desirable to reduce the forces for two reasons. First, the reduction of force in the direction of the structure decreases the likelihood of the burr deviating from the plan and colliding with the structure that needs to be preserved. Second, lower forces reduce the heat generation, decreasing the likelihood of thermal damage.

The model developed by Arbabtafti et al. [38] as part of their haptic simulator for bone machining using a spherical fluted cutting burr enables force estimation based on the position of the burr and the voxel intensity values. This model can be used to aid in robotic trajectory planning by predicting the forces based on the pre-operative images. From [38], the total force acting on each blade at any instant is given by:

$$\begin{bmatrix} F_x \\ F_y \\ F_z \end{bmatrix} = \oint_s \begin{bmatrix} dF_x \\ dF_y \\ dF_z \end{bmatrix} = \oint_s \left(T_{local}^{tool} \begin{bmatrix} K_t \\ K_r \\ K_a \end{bmatrix} t \right) ds, \tag{2.3}$$

where K_t, K_r, and K_a represent the specific cutting energy for the material in the tangential, radial, and axial directions of the local coordinate frame, respectively, T_{local}^{tool} is the transformation between the local coordinate frame at the cutting position and the tool coordinate frame, and t is the chip thickness or depth of cut. Note that T_{local}^{tool} is unique for each position on the surface of the cutting burr (see Figure 2.4). The cutting energies can be calibrated

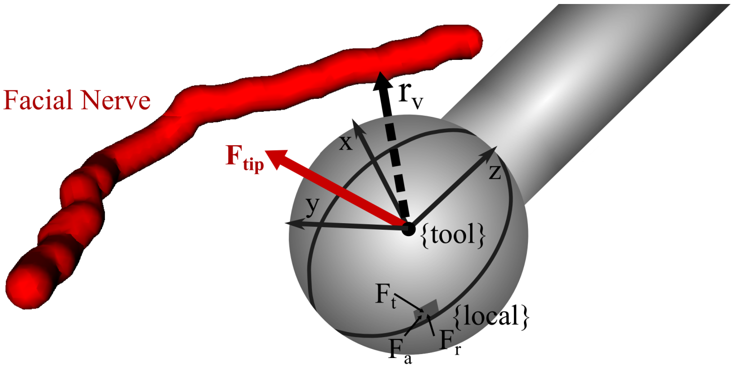

Figure 2.4: Cutting burr in a position close to vital anatomy (facial nerve) showing the vector, $\mathbf{r_v}$, pointing from the burr center to the nearest point on the nerve. The tool coordinate frame and force vectors in the local coordinate frame for a single point along a blade are shown in the figure. F_t, F_r, and F_a represent the tangential, radial, and axial components of the force in the local coordinate frame, respectively.

for the particular material by recording forces at various depths and tool orientations. The cutting tool also impacts the calibration since its geometry can influence how chips are removed, which can affect the forces on the tool.

Using (2.3), the differential forces acting along the blade are integrated over the entire surface of the blade engaged in cutting. This equation is expanded in discrete form in [38] for use in voxelized images and to account for all cutting blades. The forces along each discretized element of a blade are integrated along the z-direction at N_γ angular increments as the blade moves through a total angle of Ψ, which is the angle between two blades. This calculation is performed for each of the blades $(1 \ldots N_\beta)$ and averaged for each of the angular increments to obtain the total force on the burr:

$$\begin{bmatrix} F_x \\ F_y \\ F_z \end{bmatrix} = \left(\sum_{i=1}^{N_\beta} \sum_{j=1}^{N_\gamma} \sum_{k=1}^{N_z} T_{local}^{tool} \begin{bmatrix} K_t \\ K_r \\ K_a \end{bmatrix} t(i,j,k)\, dz \right) / N_\gamma \tag{2.4}$$

where N_z represents the number of differential elements along the cutting blade in the z-direction and dz is the height of each element. See [38] for a more detailed derivation of the above equation.

The direction of the force, $\mathbf{F} = [F_x, F_y, F_z]^T$, can be compared to the vector between the cutting burr and the nearest point on the vital structure, $\mathbf{r}_v$, to determine if the cutting force is pushing the burr towards the structure (see Figure 2.4). The component of the force in the direction of the vital structure is:

$$F_v = \mathbf{F} \cdot \hat{\mathbf{u}}_v \tag{2.5}$$

where $\hat{\mathbf{u}}_v$ is the unit vector along $\mathbf{r}_v$ (F_v is set to 0 for $\mathbf{F} \cdot \hat{\mathbf{u}}_v < 0$). This information can be used to adjust the orientation of the drill such that the resultant force in the direction of the vital structure is minimized. Therefore, if there is a deflection of the robot, the likelihood of that deflection causing damage to the patient is reduced.

2.3.4 Orientation Selection

Given a range of shaft orientations for which the robot can safely reach the current target point, knowledge of what bone has been removed thus far in the path, and the CT scan of the patient, a desired shaft orientation can be calculated by minimizing a cost function that incorporates (2.2) and (2.5):

$$C = \alpha_1 \frac{F_v}{||\mathbf{F}||} + \alpha_2 (1 - I_n) \tag{2.6}$$

$$\begin{bmatrix} \theta_{desired} \\ \phi_{desired} \end{bmatrix} = \operatorname{argmin}(C, [\theta, \phi]). \tag{2.7}$$

The coefficients α_1 and α_2 are varied based on the proximity to the nearest vital structure. When the burr is close to a structure that must be avoided, the first term of the cost function is the primary consideration. As the burr moves further away from the structure, the second term becomes the primary consideration. The scaling for a given point is based on the distance away from the vital structure at that point compared to the minimum allowable distance, $r_{v,min}$, as follows:

$$\alpha_1 = 0.5e^{-\kappa_\alpha(r_v - r_{v,min})} \tag{2.8}$$

$$\alpha_2 = 1 - \alpha_1 \tag{2.9}$$

where κ_α determines how quickly the value of α_1 drops off with distance away from the structure. If multiple vital structures are used in the planning algorithm, the closest one can be chosen for a given calculation. If multiple structures are in close proximity to the burr at any point in time, the higher priority structure can be used in the calculation. Alternatively, an additional term can be added to (2.6) to represent the force directed toward the second structure.

2.3.5 Incorporating Robot Deflection

Instead of simply using the direction of the force on the cutting burr, the deflection of the burr can be estimated given knowledge of robot stiffness. Assuming quasi-static loading and that the robot links are rigid relative to the joints, tip deflection can be approximated for a given force as:

$$\Delta\mathbf{p} = \begin{bmatrix} \Delta x \\ \Delta y \\ \Delta z \end{bmatrix} \approx C(q)\mathbf{F} \tag{2.10}$$

where $C(q) = J\chi^{-1}J^T$ is the compliance matrix of the robot. J is the robot Jacobian and $\chi = \mathrm{diag}[k_1, ..., k_m]$ is a matrix of joint stiffnesses, where k_i $(i = 1...m)$ are the stiffness values for each of the m robot joints. Stiffness values representing "virtual joints" as described in [41] can also be included to account for off-axis joint compliance. Then, (2.5) and (2.6) become:

$$\Delta p_v = \Delta\mathbf{p} \cdot \hat{\mathbf{u}}_v \tag{2.11}$$

$$C = \alpha_1 \frac{\Delta p_v}{||\Delta\mathbf{p}||} + \alpha_2(1 - I_n) \tag{2.12}$$

Δp_v is set to 0 for $\Delta \mathbf{p} \cdot \hat{\mathbf{u}}_v < 0$.

2.3.6 Cutting Velocity

The velocity of the cutting burr along the trajectory is selected based on two factors: the amount of bone being removed and the orientation of the shaft at that point. When there is more bone (in terms of both volume and density), the robot should be programmed to cut slower. Since the total force is proportional to the mass of bone in contact with the burr and inversely proportional to the cutting velocity, an inverse relationship between mass and velocity is used ($v_{cut} \propto \frac{1}{m}$). The "mass" of bone can be calculated from image intensity and the partial volume of voxels within the burr as $m = \sum_{i=1}^{n} \rho_i V_i$. To also account for the orientation-based cutting effectiveness and proximity to vital anatomy, the value determined from (2.6) or (2.12) is used. A low minimum cost function value means that there is an achievable orientation that provides good cutting performance. Thus, the velocity should be higher for lower values of C.

$$v_{cut} = k_{vel} \frac{1}{m} (1 - C) \tag{2.13}$$

where k_{vel} is a constant value that accounts for the magnitude of the intensity mapping such that the mean calculated velocity falls in the center of the allowed velocity range ($v_{min} \leq v_{cut} \leq v_{max}$). The above equation yields high velocities at points when the amount of bone in contact with the burr is low or the bone to be cut is located at the side of the burr. Lower velocities are commanded when the burr is in contact with a large amount of dense bone, close to a vital anatomical structure, or it is not oriented well for efficient cutting. Due to the presence of air cells, the commanded v_{cut} values can fluctuate rapidly as the burr moves in and out of air cells. A simple weighted, moving average filter is applied to the v_{cut} data to ensure smooth motion and avoid very high accelerations at bone/air transition points.

2.3.7 Joint Trajectory Generation

The joint trajectory is generated from the target points ($\mathbf{p}_{burr}$), velocities (v_{cut}), and desired orientation values (θ_{des}, ϕ_{des}). The desired drill orientation, as determined from minimizing the cost function, may change suddenly due to variable bone density and porosity. Thus, it is necessary to smooth these values to avoid rapid angle changes that may require joint velocities beyond the limits of the robot and reduce the ability of the surgeon to safely monitor the procedure. This smoothing can be applied directly to the desired angular values by using a low-pass filter. Alternatively, the orientation could be accounted for by considering only the Cartesian path positions as the task space and steering the orientation towards the desired value as a subtask in a redundancy resolution approach.

2.4 Experimental Methods

The algorithm described in Chapter 2 was tested on a four degree-of-freedom (DOF), bone-attached robot designed for mastoidectomy (see Figure 2.5) [30]. Bone-attached robots can achieve higher positional accuracy since they do not require intra-operative tracking, which inherently introduces some level of registration error. However, they must be made small enough to mount on the patient without causing too much stress on the mounting points. Thus, these robots may not be as stiff as a larger robot and can therefore benefit from a planning algorithm that incorporates the minimization of deflection towards vital anatomy. Since the robot used in these experiments has three linear joints and one rotational joint, the drill shaft orientation is defined by this joint and the cost function is minimized over one variable, θ.

2.4.1 Phantom Test Block Experiments

The first set of experiments were performed using Sawbones (Pacific Research Laboratories, Vashon Island, WA USA) mechanical test blocks made from solid rigid polyurethane

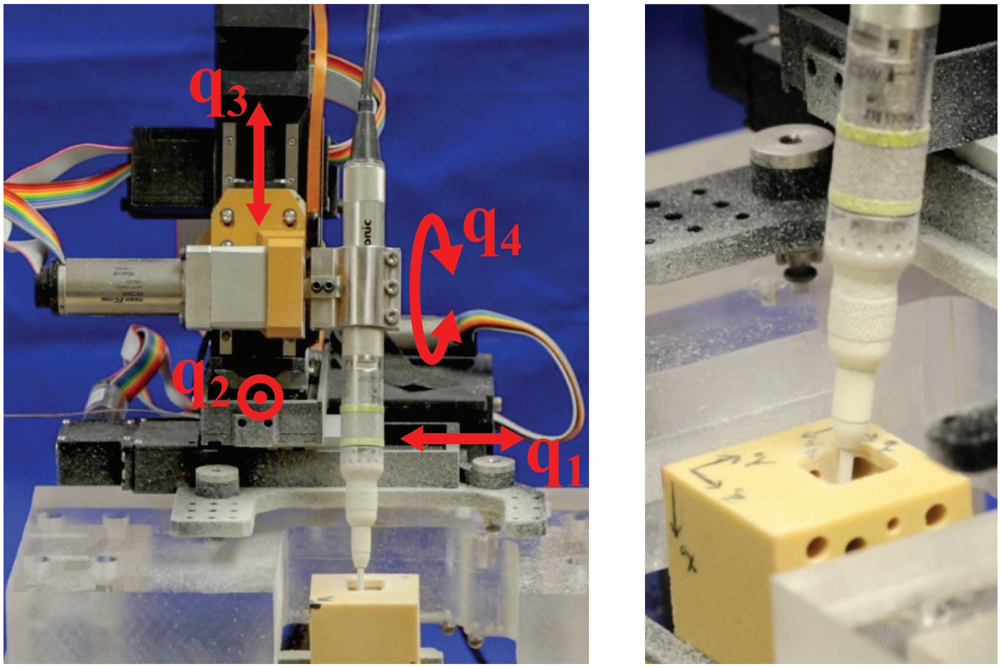

(a) (b)

Figure 2.5: (a) Custom four DOF bone-attached robot for mastoidectomy mounted to the test platform. The fourth joint (q_4), which controls the drill orientation (θ) is determined by the optimization algorithm. (b) Close-up of the surgical drill milling temporal bone phantom during an experiment.

foam ($\rho = 0.8\frac{g}{cm^3}$). The blocks were custom-machined to add holes (3-5 mm in diameter) that mimic the air cells found in the mastoid region of the temporal bone. Figure 2.6 shows a photograph of the test blocks and a slice of the image used for planning. To simplify the experimental protocol, the image was generated from a model of the custom-machined test blocks. To make the image-based planning more realistic, Gaussian noise with a standard deviation of 5% of the mean voxel intensity was added to the generated image. A virtual facial nerve was added to the image (see Figure 2.6b) and its position was used in the trajectory planning algorithm. The block was placed in an experimental jig at a known location with respect to the robot. The same planning process would be used if the image was acquired using a CT scanner with the additional steps of localizing the structures and registering the anatomy to the robot.

A total of three experimental trials were performed. All trials were performed with the

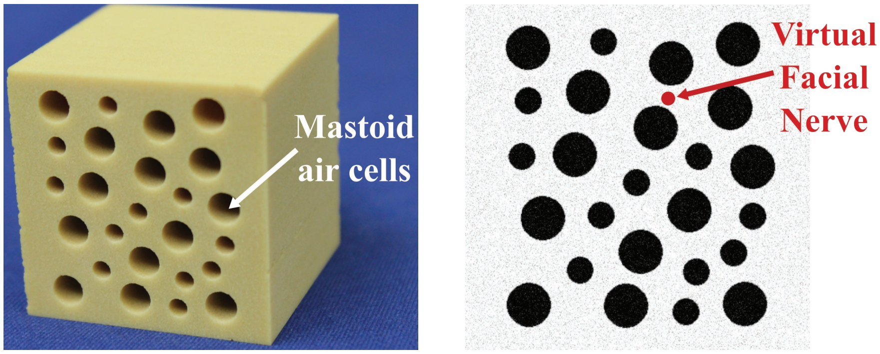

(a) (b)

Figure 2.6: (a) Photo of the biomechanical test block used in experiments and (b) image slice of the test block showing virtual facial nerve that was added to the image for the testing of the planning algorithm.

same Cartesian path at the same location in the phantom block, which enabled comparison between the different optimization approaches. The trajectory optimization step described in Chapter 2 is independent of the Cartesian path so any path could have been used in the experimental trials. For simplicity, the path used was a simple “lawnmower” type path in which the volume of bone was removed layer-by-layer. The outer path dimensions were 15 mm x 15 mm x 15 mm and the depth of each layer was 1.5 mm.

The first two trials were performed to evaluate the orientation selection component of the motion planning algorithm. The first trial, which serves as the control trial, used a constant angle ($\theta = 0°$) and constant milling velocity ($v = 1.5\frac{\text{mm}}{\text{sec}}$). The second trial was constrained to the same velocity but the orientation was varied along the path, with the value selected by minimizing (2.6). The optimization was performed using the `fminbnd` function in MATLAB 2015a (The MathWorks Inc., Natick, MA, USA). The drill inclination angle θ was bounded by both the limits of the robot and the constraints imposed by the unmilled bone at each point along the trajectory. Forces were recorded throughout both trials using a six-axis force/torque sensor (Mini40, ATI Industrial Automation, Apex, NC, USA) positioned between the second and third joints of the robot. The force data was smoothed using a moving average filter and analyzed according to the position of the cutting burr at the time of the force reading. When the burr was within 2 mm of any point on the facial nerve, the measured force was projected along the unit vector between the burr and the closest point on the nerve ($\hat{\mathbf{u}}_v$). The magnitude of forces towards the facial nerve was compared for the two trials. Additionally, the force values for all points along the trajectory were compared for the two trials.

A third milling trial was performed to include the velocity scaling component of the motion planning algorithm as well as the orientation selection. The same Cartesian path used in the two trials described above was planned in the phantom material. For this trial, the linear velocity, v_{cut}, was regulated according to (2.13). The linear velocities were scaled such that the total procedure time was equal to the control trial (9 minutes, 26 seconds) and a fair comparison of forces could be made to prior trials. Again, (2.6) was used to select the drill orientation. The force data was recorded and compared to the first two trials.

2.4.2 Cadaver Head Bone Drilling Experiments

The second set of experiments were performed on cadaveric temporal bone for a more clinically-relevant scenario (see Figure 2.7). Since temporal bone is denser than the synthetic Sawbones material from the first set of experiments (up to $1.87\frac{g}{cm^3}$ vs. $0.80\frac{g}{cm^3}$ [42]), it is expected that forces will generally be higher in the actual bone. Unlike the phantom test block experiments, where material properties such as density and air cell configuration could be held constant, actual temporal bone varies between experiments due to variance in pneumatization (location and size of air pockets within the bone). This variation makes force comparisons between the different trials more challenging. For this reason, only the full optimization trial, in which both velocity and drill shaft angle are determined by minimizing the cost function, was performed and compared to a control trial, in which both velocity and drill shaft angle are held constant. In an attempt to normalize pneumatization, so that the comparison between the full optimization trial and the control trial was as fair as possible, a single cadaver head was used for each experiment. Pneumatization of the mastoid is relatively symmetric between the right and left temporal bones of a single cadaver head, but it can vary significantly between individuals [43, 44]. Therefore, the full optimization trial was performed on the right temporal bone of the cadaver head, and the control trial was performed on the left for each experiment. Figure 2.8 shows the pneumatization symmetry between the right and left sides of Cadaver Head 2 (CH 2). A total of three cadaver heads were used.

Since the target bone to be removed had to be segmented for each side separately, an effort was made to keep the volumes approximately the same for a fair comparison between the control and the full optimization. This involved removing some of the target volume from the larger of the two mastoids so that it closely matched the target volume of the smaller mastoid. Figure 2.9 shows the right and left target volumes to be removed for Cadaver Head 3 (CH 3).

Each trial followed the same protocol for performing a full mastoidectomy, which is outlined in detail in [30] and reiterated here. First, a preoperative CT scan of the cadaver head was taken, and the vital anatomy (e.g. facial nerve, chorda typani) was automatically segmented using previously developed methods [45, 46]. With the locations of the vital anatomy as boundaries, a target region of bone to be removed was manually delineated on the preoperative CT scan using custom software. Next, the cadaver was prepared for robot attachment by making a standard incision and lifting the tissue behind the ear to expose the mastoid region of the temporal bone. A pre-positioning platform (PPF), which serves as the intermediate attachment piece between the cadaver head and the robot, was attached to the skull using three cranial plating screws. Six spheres attached to the surface of the PPF serve as both attachment points for the robot and fiducial markers for registration. With the PPF attached, an intraoperative scan was taken and registered to the preoperative scan using intensity-based registration [47]. Then, the fiducial markers were localized within the intraoperative scan and used to register the intraoperative scan to the robot coordinate frame using point-based registration [48]. Using these two registrations (from preoperative CT to

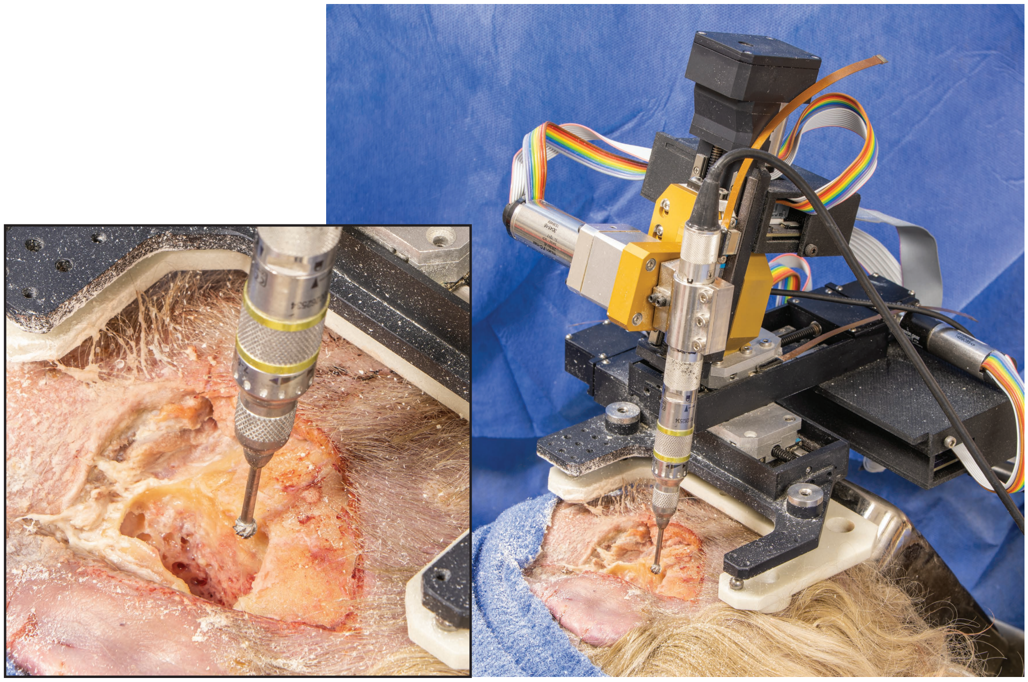

Figure 2.7: Custom four DOF bone-attached robot for mastoidectomy mounted to a cadaver head. A full mastoidectomy was performed on both sides of the head. The left side drilling was used as the control trial in which both the drill orientation and drill velocity along the trajectory were held constant. The full optimization algorithm was used on the right side to determine drill orientation and drill velocity along the trajectory. The inset in the left corner shows a close-up of the pocket of bone milled away.

intraoperative CT and from intraoperative CT to robot coordinate system), the pre-planned target and anatomy were transformed into the robot coordinate system. Next, a milling path that will remove the maximum amount of target bone without damaging the vital anatomy was planned, and the corresponding robot trajectory was generated. The robot was then attached to the PPF for the start of bone milling.

A total of three cadaver heads were used for these experiments, and a full mastoidectomy was planned and milled on both sides of each head (two trials per head for a total of six trials). Just as with the block experiments in Section 2.4.1, a simple “lawnmower”-type path was used in which the volume of bone was removed layer-by-layer. Since the shape of the mastoid target volume was more irregular than the simple cube volume used with the blocks, an extra pass of the drill around the outside boundary of each layer was necessary to

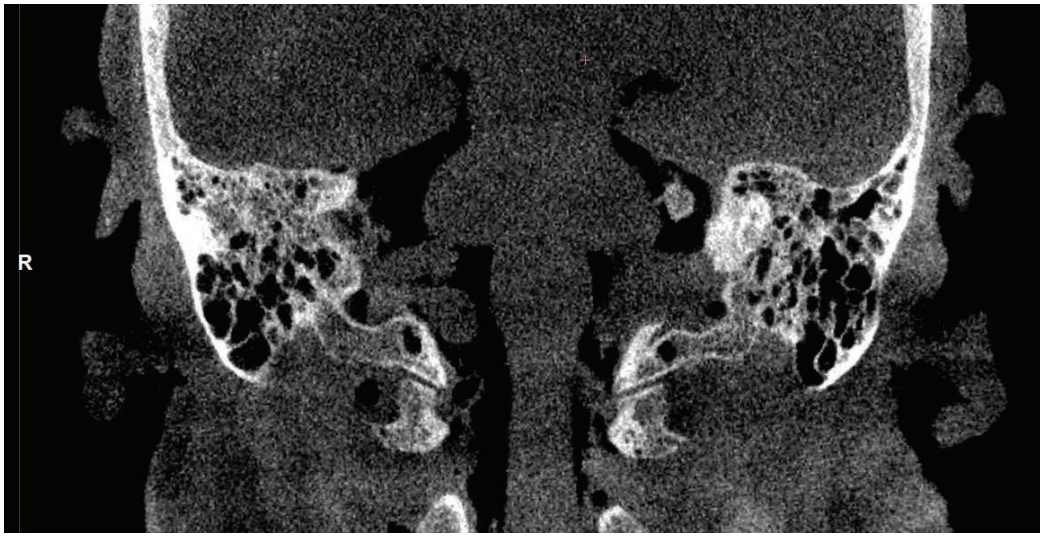

Figure 2.8: This shows the pneumatization of the mastoid region of the temporal bone in Cadaver Head 2 (CH 2). It can be seen that the degree of pneumatization is symmetric between the left and right side.

ensure the full target volume was milled. On the right side of each head, the full optimization motion planning algorithm was used with drill motion velocity limits between 1 mm/s and 8 mm/s enforced. The 8 mm/s upper limit was chosen for safe robot execution and has been used safely in a bone milling robot for craniotomy [49]. For these full optimization trials, the linear velocity, v_{cut}, was regulated according to (2.13) and scaled with k_{vel} such that the average velocity over the entire drilling was 3 mm/s. Previous bone milling robots for craniotomy safely used a 3 mm/s feed rate [49]. On the left side of each head, a control trial was performed using a constant drill orientation ($\theta = 0°$) and a constant velocity ($v = 3\frac{mm}{ss}$). The constant velocity for the control trial was chosen to be equal to the average velocity for the full optimization trial so that a fair comparison of forces could be made between the two trials.

2.4.3 Breakthrough Force of Skeletonized Bone Surrounding Facial Nerve

A worst-case injury from mastoidectomy involves damage to the facial nerve. It is common to skeletonize bone surrounding the facial nerve as part of the mastoidectomy

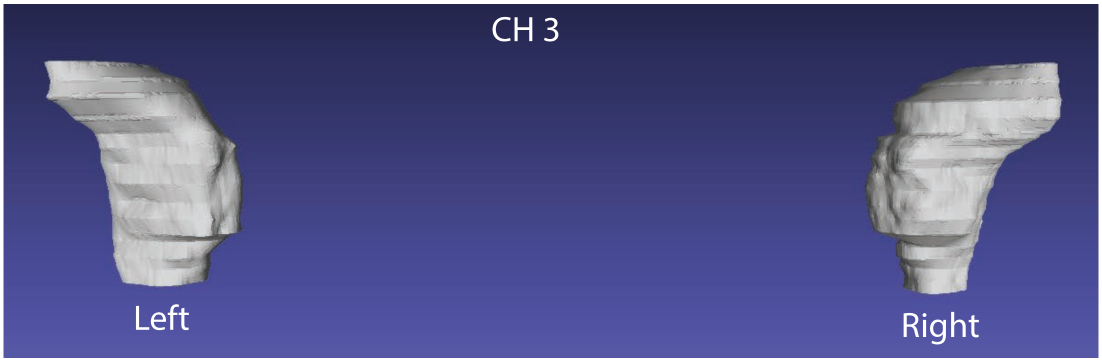

Figure 2.9: The right and left target volumes of bone to be removed are shown for Cadaver Head 3 (CH3). The target volumes were segmented such that approximately equal volumes were to be milled for each side.

procedure, but this increases the risk of drill damage to the facial nerve. Surgeons reduce drill movement and perform drilling carefully and efficiently when removing bone in close proximity to the facial nerve. Through our new patient-specific algorithm outlined in 2.3, we aim to give human-surgeon drilling technique to the robot for safer drilling. In a worst-case scenario, cutting forces in the direction of a facial nerve could exceed the breakthrough force of the skeletonized bone surrounding it. This would cause the drill to rupture the surrounding bone and damage the facial nerve. To quantify this worst-case breakthrough force, we set up an experiment to drive a surgical drill into a skeletonized facial nerve specimen atop a force sensor, and we measure the force required to break through the bone and damage the facial nerve. This breakthrough threshold is then used to motivate any force reductions using our new algorithm.

Figure 2.10 shows the experimental setup used to quantify the drilling breakthrough force on the skeletonized bone surrounding the facial nerve of a cadaver specimen. The specimen sat on top of a force sensor (Nano25, ATI Industrial Automation, Apex, NC), which was used to measure the drilling forces. A surgical drill was attached to a linear slider, and while the drill bit was spinning at 20,000 rpm, it was slowly driven downwards until it made contact with the cadaver specimen. With the drill tip aligned so that it would contact a thin portion of the bone ($\sim$ 0.5 mm) on top of the facial nerve, the drill was slowly

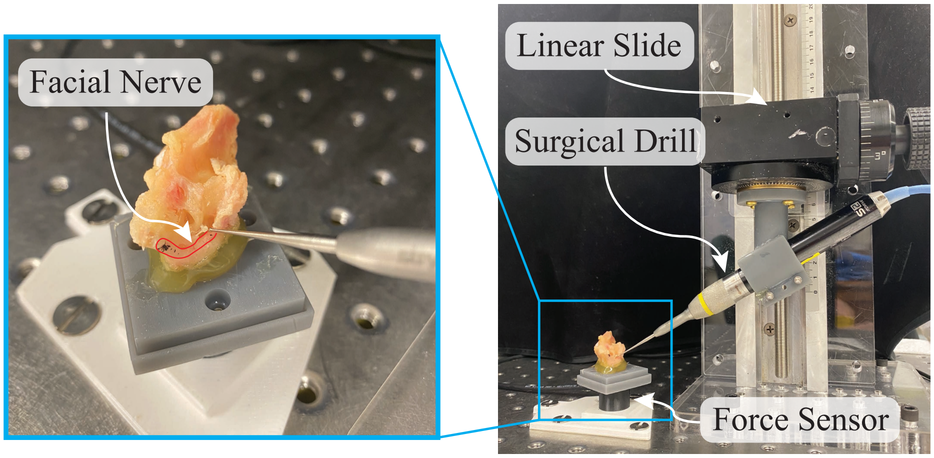

Figure 2.10: The experimental setup to quantify the drilling breakthrough force on the bone surrounding the facial nerve of a cadaver specimen after it has been skeletonized. A surgical drill was attached to a linear slide, and while spinning at 20,000 rpm, it was lowered into the specimen. Under the specimen is a force sensor (Nano25, ATI Industrial Automation, Apex, NC), which was used to record the forces applied by the drill. The left image shows a closeup of the cadaver specimen, with the facial nerve outlined in red.

lowered by hand until the drill tip ruptured the bone and contacted the nerve.

2.5 Results

2.5.1 Phantom Test Block Experiments

Figure 2.11 illustrates the reduction of forces towards the facial nerve that was achieved through the implementation of the proposed approach in the phantom block experiments. When the cutting burr was within 2 mm of the facial nerve, the control trial resulted in a mean force of 0.51 N, a 75th percentile force of 0.67 N, and a peak force of 1.60 N. The trial using the orientation optimization had mean, 75th percentile, and peak force values of 0.32 N, 0.50 N, and 1.16 N, respectively. Finally, the trial using the full (orientation and velocity) optimization had mean, 75th percentile, and peak force values of 0.19 N, 0.33 N, and 0.80 N, respectively. Compared with the control trial, the full optimization trial resulted in a 63% reduction in mean forces and a 50% reduction in peak forces toward the facial nerve.

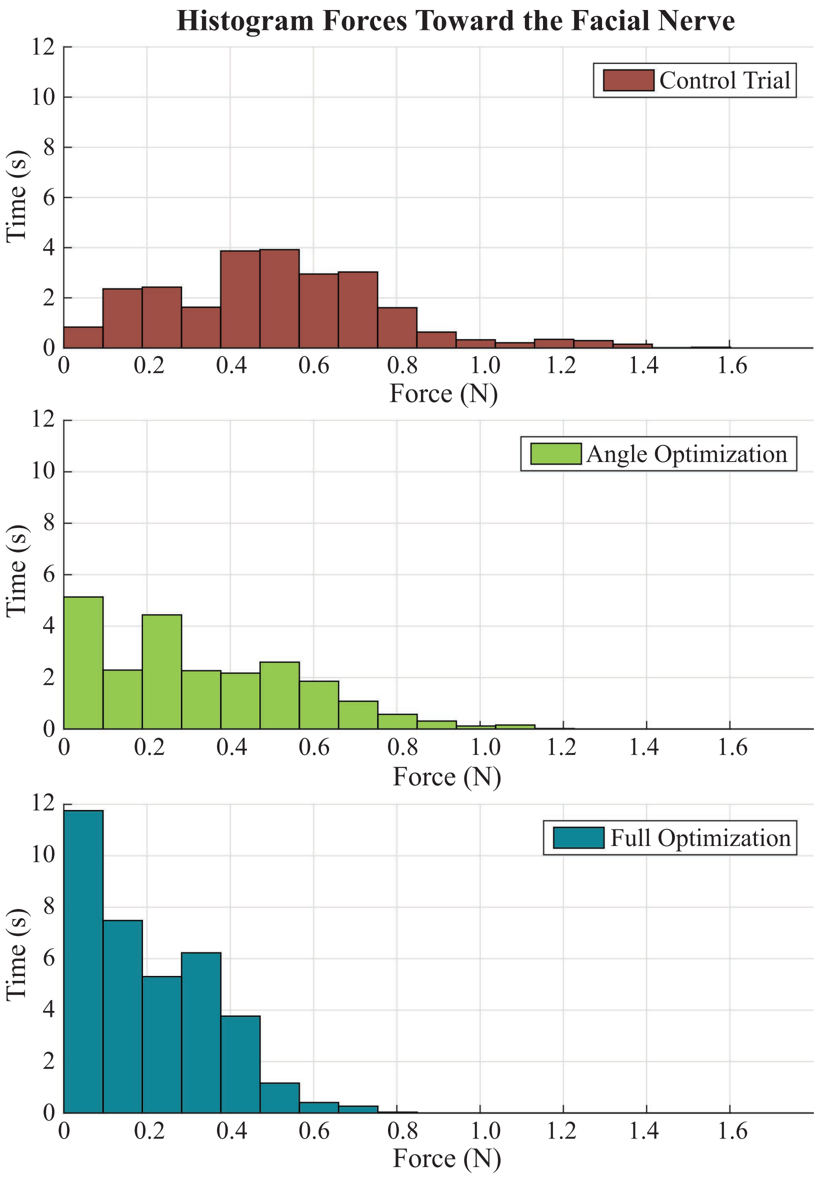

Figure 2.11: Cutting forces towards the facial nerve when the burr was within 2 mm of the nerve. “Angle Optimization” refers to the trial in which only the regulation of the incidence angle was enabled and “Full Optimization” refers to the trial that used both angle and velocity regulation based on (2.6) and (2.13).

In addition to minimizing forces directed at the facial nerve, the proposed approach was found to produce an overall reduction of cutting forces throughout the milling process. This can be observed in the force magnitude plot (Figure 2.12): the control trial resulted in a mean and peak force of 0.73 N and 3.24 N, whereas the trial that used variable incidence

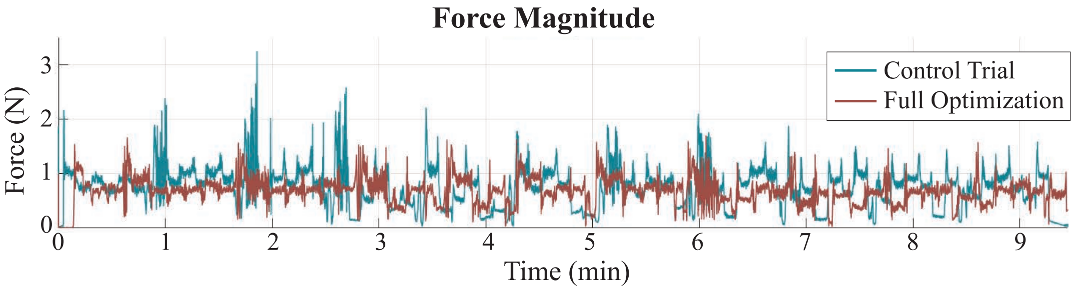

Figure 2.12: Force magnitude observed throughout the milling process. Here, “Full Optimization” refers to the trial that used both angle and velocity regulation. These plots show an overall reduction in mean and peak forces using the angle and velocity regulation. Note that the velocity was not constant throughout the full optimization trial so specific points along the path for the two trials do not occur at the same time. Thus, this plot provides a general comparison of the overall forces rather than a comparison at specific points along the path.

angle and milling velocity had a mean force of 0.66 N and a peak force of 1.69 N.

2.5.2 Cadaver Head Bone Drilling Experiments

As motivation for reducing forces toward the facial nerve, we quantified the breakthrough force when drilling skeletonized bone surrounding the facial nerve. Figure 2.13 shows a force threshold of $\sim$ 0.3 N to break through the bone and damage the facial nerve. As this is a small force for a worst-case scenario, reducing forces toward the facial nerve during drilling will improve safety and limit the potential for damage to the facial nerve. This 0.3 N breakthrough threshold was used in 2.1 to compare the control trial to the full optimization trial and determine if force reductions due to the new algorithm were clinically significant.

Table 2.1 shows the reduction of forces towards the facial nerve that was achieved by the patient-specific motion planning algorithm in the cadaveric temporal bone. Additionally, Figure 2.14 shows a graphical representation of the forces towards the facial nerve as a function of their distance from the facial nerve (within 3 mm). When the cutting burr was within 3 mm of the facial nerve, mean forces were reduced by 0.006 N and 0.019 N

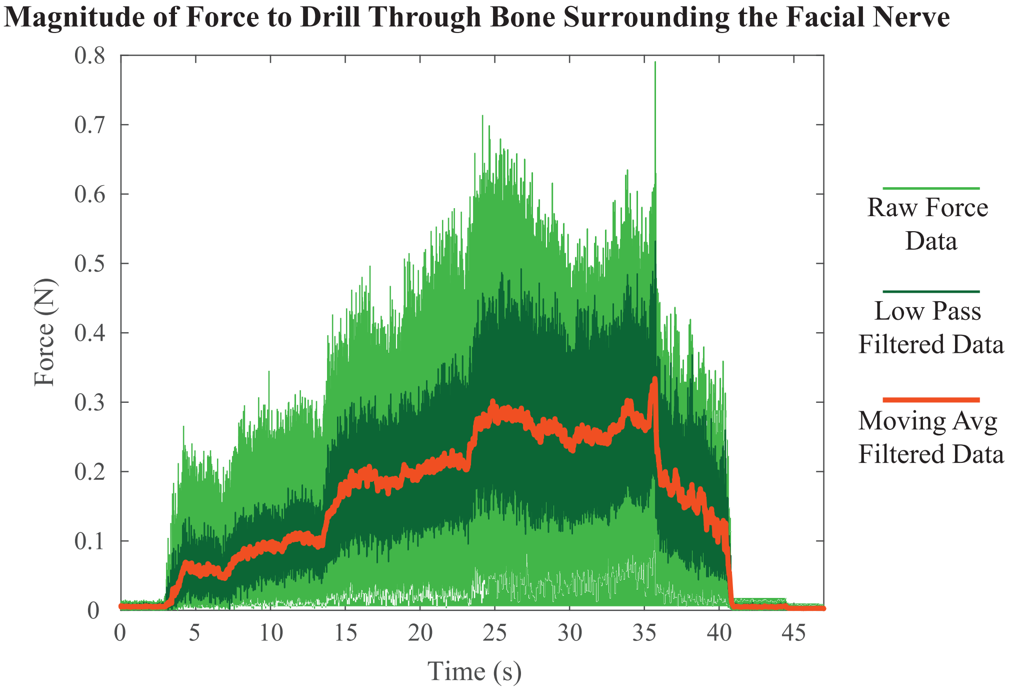

Figure 2.13: This plot shows the force to drill through the skeletonized bone surrounding the facial nerve. Due to the vibrations caused by the surgical drill, the raw force data needed to be filtered to obtain a clean measurement. Both a low-pass filter (dark green) and a moving average filter (orange) based on the surgical drill speed to average every 25th rotation were applied to the raw data. The breakthrough force can be seen at approximately 35 seconds, where there is a sharp decrease in force. The force here is $\sim$ 0.3 N.

and maximum forces were reduced by 0.128 N and 0.356 N for Cadaver Head 1 and 3, respectively. In both Cadaver head 1 and 3, the max force in the direction of the facial nerve exceeded the breakthrough force (0.3 N) of a worst-case scenario of drilling skeletonized bone on the facial nerve. In this case, damage to the facial nerve is possible and the percentage of forces above this experimentally derived threshold were 0.07 and 2.24 for Cadaver Head 1 and 3, respectively. After implementing the new algorithm for full optimization, the maximum forces toward the facial nerve fall below this threshold. This brings the percentage of forces above the facial nerve damage threshold to 0 for both Cadaver Head 1 and 3.

Additionally, forces over the entire mastoidectomy were compared for the three Ca-

		Forces Toward Facial Nerve (within 3 mm of FN)		
Cadaver Head #		Left Side (Control)	Right Side (Full Optimization)	Difference
CH 1:	Mean (N)	0.008	0.002	-0.006
	Max (N)	0.346	0.218	-0.128
	Above FN Damage Threshold (%)	0.07	0.00	-0.07
CH 3:	Mean (N)	0.020	0.000	-0.019
	Max (N)	0.552	0.196	-0.356
	Above FN Damage Threshold (%)	2.24	0.00	-2.24

Table 2.1: Cutting forces toward the facial nerve (FN) when the burr was within 3 mm of the nerve. The mean and maximum cutting forces towards the facial nerve for both CH 1 and CH 3 are included in this table. Additionally, the percentage of cutting forces that were above the 0.3 N threshold for breaking through the skeletonized bone surrounding the facial nerve (see Figure 2.13) are included. The left and right side refer to the left mastoid and right mastoid millings and correlate to the control and full optimization trials, respectively. The difference between the two is included in the rightmost column. Note that CH 2 was excluded from this data because the cutting burr in the control trial did not get within 3 mm of the FN due to anatomic constraints.

daver Head experiments. Table 2.2 compares the mean, 75th percentile force, and maximum milling forces between the left and right side mastoids, which correlate to the control and full optimization trials, respectively. Based on these trials, implementation of the full optimization reduces the maximum forces by 2.87 N, 0.34 N and 4.15 N for Cadaver Heads 1 through 3.

2.6 Discussion

The experimental results demonstrate that the proposed methodology is able to decrease cutting forces near vital anatomical structures and throughout the bone milling procedure. This is attributed to the incidence angle and velocity regulation scheme described by (2.6) and (2.13), which makes the robot mill more like a surgeon, i.e. varying the angle to control the cutting efficiency, moving slower when close to critical anatomy, and faster when in non-critical areas. This reduction of cutting forces is expected to bear two important

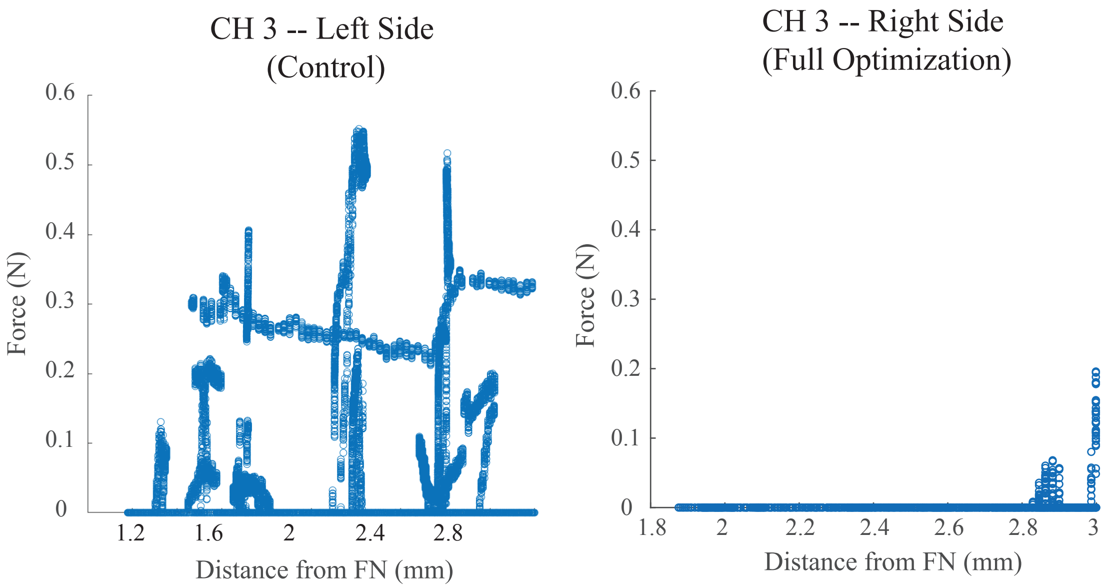

Figure 2.14: Cutting forces toward the facial nerve (FN) when the burr was within 3 mm of the nerve. This shows the data for Cadaver Head 3 (CH 3) with the control and full optimization on the left and right, respectively. Note the reduction in force spikes towards the facial nerve for "Full Optimization," which refers to the trial that used both angle and velocity regulation based on (2.6) and (2.13).

clinical advantages. The first and most evident is that deflections of the robot towards vital anatomy (e.g. facial nerve, major blood vessels) will be smaller, thereby reducing the risk of accidental collisions when the burr is moving in close proximity to the structures. Second, lower cutting forces are expected to reduce the rate of thermal energy transferred to the surrounding bone, which could lead to heat-related trauma to the underlying vital structures. This latter implication is especially important in light of recent work that suggests high temperatures induced by bone drilling may cause thermal injury to the facial nerve [50, 51].

2.7 Conclusion

Chapter 2 presented a novel method for robotic bone milling that uses image-based bone density estimates along with the location of vital anatomy to generate a safe and efficient cutting plan. The method regulates the burr incidence angle to control the cutting

		Force Data for Full Mastoidectomy		
Cadaver Head #		Left Side (Control)	Right Side (Optimized)	Difference
CH 1:	Mean (N)	1.09	1.25	0.16
	75th Percentile (N)	1.47	1.58	0.11
	Max (N)	11.86	8.99	-2.87
CH 2:	Mean (N)	0.86	1.14	0.28
	75th Percentile (N)	1.40	1.70	0.30
	Max (N)	9.61	9.27	-0.34
CH 3:	Mean (N)	2.67	1.05	-1.62
	75th Percentile (N)	2.75	1.25	-1.50
	Max (N)	14.18	10.03	-4.15

Table 2.2: Comparison of force data observed for the full mastoidectomy on three cadaver heads. Here, the full optimization trial was performed on the right side temporal bone and the control trial was performed on the left side temporal bone for each cadaver head. The mean, 75$^{\text{th}}$ percentile, and max force values are reported for each side and each head. The difference column contains the full optimization trial forces (right side temporal bone) minus the control trial forces (left side temporal bone) for each head to compare the two trials. Here we see that in each case, the maximum milling force is reduced when the full optimization algorithm is used.

forces that occur at the burr-bone interface. The objectives are to improve the safety and efficiency of the milling procedure by avoiding large forces that could deflect the robot towards vital anatomy (e.g. facial nerve), thus reducing the risk of accidental collisions, as well as enabling faster milling in areas of low-density bone. The tool orientation and cutting velocity are selected based on the local density of bone and the proximity to vital anatomic structures.

The proposed method was implemented using a 4-DOF bone-attached robot for mastoidectomy. Milling experiments were performed on both custom temporal bone phantoms and actual temporal bone. The results revealed a reduction of mean and peak forces compared to CNC-like bone milling. This indicates that by giving a robot human-surgeon qualities, such as the ability to adapt to specific patient anatomy, robotic mastoidectomy is improved. In the long run, a robotic approach to this surgery would lead to more repeatable and accurate outcomes, which would benefit patient safety. In addition, with this robotic approach that takes into account both distance to vital anatomy and image-based bone density estimates, surgery time could be decreased by running the robot much faster in areas of less dense bone that are far enough away from vital structures. Future research will focus on further experimental validation of the approach, with an emphasis on quantifying the surgical time savings by using this approach. The benefits of human-robot collaborative path adaptation to this automated approach bring this device closer to clinical translation. However, this robot will still take years before proving to be a viable commercial product due to the harsher regulations for automated devices towards clinical adoption. Additionally, the barrier to adoption by medical professionals is high for an automated approach to something currently performed manually.

Chapter 3

Miniature Magnetorheolical Brake with High Torque and Fast Response

3.1 Chapter Overview

The second approach to a human-robot collaborative device to improve mastoidectomy starts with the surgeon, and using an inherently safe, cooperative device, it gives the surgeon enhanced robotic accuracy and augmented spatial awareness. Like ANSR, in Chapter 2, this device is designed to be bone-attached, so that the tracking error can be eliminated for increased accuracy. Also, to ensure the inherent safety of the system, the device is designed to be completely passive utilizing brakes at each joint, which eliminates any risk of errant motion from actuators such as motors. The brake enforces boundaries to the surgical drill so that it stays within the target volume of bone to be removed and stops it from damaging vital anatomy. As an essential component to the design of this device, the brake needs to be small and lightweight enough to be bone attached and powerful enough to stop the drill motion of the surgeon.

Chapter 3 presents the design and performance characterization of a miniature magnetorheological (MR) brake, with a fast time constant and a high torque-to-mass ratio designed for use in small haptic or robotic devices. More specifically, the development and characterization of this brake is a fundamental part of a cooperatively controlled passive robotic system for performing mastoidectomy described in Chapter 4. By combining a disk and drum-type design and incorporating the electromagnetic coils into the rotor, this brake utilizes all three shear surfaces of the rotor for increased braking torque. In addition, a serpentine magnetic flux path that crosses all MR fluid shear surfaces multiple times is used to achieve high braking torque in a small form factor. An FEM model was used to optimize the dimensions of the brake components to maximize magnetic flux density within the MR fluid gap. This maximizes the shear force of the MR fluid and ultimately increases the braking torque. To characterize brake performance, the relationship between current and braking torque, as well as the system dynamic response, were analyzed. The performance of our new brake is also compared to several other brakes of similar size that are available both commercially and found in the literature, and we illustrate that of these, our brake design has the highest torque to volume ratio.

3.2 Introduction

Brakes are used in many applications, including industrial equipment, automobiles, and robotics, to dissipate kinetic energy. In some applications, it is desirable for the brake to be small and light, yet provide high braking torque and fast response time. This would be advantageous, for example, in robotic applications where the brake is mounted on a moving link, and it is desirable to have low inertia to improve the dynamic performance of the arm [52, 53]. Small, light brakes with a fast response time are similarly important in haptic applications because the human sense of touch is so sensitive [54, 55, 56]. The contribution of Chapter 3 is to provide a new design that has the potential to offer improved braking torque and response time with respect to small brakes on both the commercial market and in the literature. For purposes of this Chapter, we define small brakes as those with a diameter of less than 40 mm and a thickness of less than 30 mm.

In considering which braking technologies might enable brakes to be small yet have high torque and fast response, we quickly ruled out friction brakes due to their slow response times [57], as well as the fact that they often exhibit undesirable properties including stiction, vibration, non-linearity between input current and output torque, and drift in output torque due to abrasion [58]. Electromagnetic (EM) disk brakes offer faster response time but are still not as fast as hysteresis powered (HP) brakes [59, 60], magnetic particle (MP) brakes [61], or magnetorheological (MR) brakes [62, 63, 64, 65, 66, 67]. If fast response time was the only design parameter, then a piezoelectric brake would be ideal, since these are capable of being 5-6 times faster than MP and EM brakes, respectively [61].

However, the tradeoffs for the speed of piezoelectric brakes are that they offer relatively low braking torque and are also physically relatively large when compared to other small brakes in the literature and available commercially.

The remaining electromagnetic brake types (HP, MP, and MR) are all highly controllable (i.e., the braking torque can be controlled by the amount of current supplied to the brake) and all have relatively fast response times. However, both HP and MP brakes lack powerful braking torque at small sizes, resulting in low torque-to-volume and torque-to-weight ratios for commercially available models [59, 68, 60]. Additionally, HP brakes experience cogging, a phenomenon that occurs when the control current is not removed before the rotor comes to rest and results in a pulsating output torque that prevents smooth operation, and MP brakes have a constant drag associated with them, as there is friction between the particles and the rotor even when the current-carrying coils are not energized. While MR brakes are not without disadvantages (they produce hysteretic behavior due to residual magnetic field produced within the housing of the brake [69]), of the three remaining choices, they have the greatest potential to be small, yet still produce high braking torque. To reduce the nonlinear effects of magnetic hysteresis within MR brakes, modeling of the hysteresis of ferromagnetic materials has been extensively studied [70, 71, 72, 73] and used to model the hysteresis within MR brakes [69, 74, 75, 63]. In addition, various control schemes including a reverse current burst [76] or embedded hall-effect sensors with PID control [58] to remove the residual magnetic field within the ferromagnetic housing of the brake have been shown to be successful.

Generally, magnetorheological (MR) brakes are categorized as either disk-type or drum-type by design, which is determined by the shape of the rotor and where the magnetic flux interacts with the MR fluid to create a shear surface [65, 77]. In a disk-type MR brake, the rotor is slender and the MR fluid is energized to create a shear surface on the top and bottom of the rotor surface (see [64, 62, 63, 57]). Alternatively, a drum-type MR brake has a thicker rotor such that the energized MR fluid creates a shear surface at the outer radial surface of the rotor (see [77, 67]). In this Chapter, we describe a unique design that is able to efficiently utilize all three shear surfaces surrounding the rotor (top, bottom, and side), which enables higher braking torque in a smaller package. This design, which was enabled by inverting the placement of the current-carrying coil into the rotor, can be referred to as an inverted disk-drum combination brake.

Due to the many advantages of MR brakes (e.g. fast response time, high controllability, inherent stability, and exhibiting a simple interface between the mechanical and electrical systems [58]), there has been an emphasis in the literature on using them in haptic devices. As one of the early groups to use MR brakes in haptics, Li et al. developed a slim disk-type MR brake and coupled two of the brakes to a joystick to create a 2D virtual environment [78]. Through brake design innovations and optimizations, other groups sought to increase the braking torque for a larger range of available torques within the haptic device, while keeping the brake compact [76]. Blake et al. created a particularly small MR brake, while retaining a high braking torque, for a wearable haptic glove application [79]. By incorporating low magnetic permeability material (e.g. aluminum) into the rotor and housing of a drum-type brake, Blake et al. produced a serpentine flux path such that it crosses the fluid gap multiple times. This design feature increases the braking torque of the MR brake without increasing the overall dimensions of the brake.

To generate large braking torque in a compact brake, many groups have proposed a variety of designs and strategies. Assadsangabi et al. used FEA to improve braking torque while keeping the weight low for a disk-type brake [65]. To further increase braking torque, Gudmundssen et al. proposed the use of multiple stacked disks with each disk increasing the area sheared by the MR fluid [80]. They developed a multi-disk MR brake for use in a prosthetic knee and optimized the geometric dimensions of the brake using multiple design objectives (i.e. maximize braking torque, minimize the off-state stiffness, and minimize the weight of the brake). Guo and Liao compared how three different inner coil placements affected the braking torque of a multi-disk MR brake design [81]. After optimizing the geometric design parameters, they used FEA to validate the optimized design. Having developed a novel two-disk MR brake with no viscous zero-field torque, Shamieh and Sedaghati optimized their brake to maximize braking torque while minimizing response time and brake weight [82]. They used a genetic algorithm combined with a sequential quadratic programming algorithm to find an optimal solution.

Another way of increasing braking torque compared to the standard disk- or drum-type brake is to use a T-shaped rotor. Similar to the multi-disk design, the T-shaped rotor increases the area that is sheared by the MR fluid, which increases the braking torque. Avraam et al., after comparing the most common MR brake types (i.e. drum, disk, inverted drum, T-shaped, multiple-disks), developed an MR brake with a T-shaped rotor design for a wrist rehabilitation device [83]. Similarly, Nguyen and Choi compared the most common MR brake types with the objective of maximizing braking torque within a given volume [84]. Based on the optimal solutions, they provided advice on the optimal selection of MR brake type.

Most recently, with the goal of miniaturizing the MR brake while retaining high braking torque for use in haptics, Qin et al. adopted a novel multi-drum MR brake design [85]. Similar to a design from Rossa et al. [86], this multi-drum MR brake has one of the highest torque-to-volume ratios in the literature. In a successive paper, Qin et al. further evaluated the multi-drum brake based on the number of drums and fluid gap selection in optimization [87]. In addition to various MR brake designs described above, research groups have explored how changing specific components within the brake can increase braking torque. These include changes to the fluid gap size [88] and the magnetic core shape [89].

In this Chapter, we created a miniature MR brake that is powerful (high braking torque for its size) and fast acting. Both of these characteristics can be effectively applied to haptics or wearable robotics. Our new MR brake has two design features that, when used in combination, enable the brake to be compact, yet efficiently utilize all three shear surfaces surrounding the rotor, amplifying the braking torque. Utilization of the three shear surfaces in this manner is a design innovation that enables the brake to exhibit the highest torque-to-mass ratio among comparable-sized MR brakes in the literature. First, the placement of current-carrying coils is inverted such that they reside in the rotor, rather than the traditional location of the housing. This increases the moment arm in the brake, since braking forces are applied at the outer edge of the housing. The second design feature is the serpentine magnetic flux path we employ so that it crosses the MR fluid gap a total of six times, which increases the magnetic flux density (and hence braking torque) within the MR fluid in comparison to prior designs of similar size which have had at most only 4 crossings [79]. The combination of these two design features is what allows the brake to efficiently use all three shear surfaces surrounding the rotor and to increase the braking torque in a small package. In comparing our new brake design to other small MR brakes, which we define as brakes with an outer diameter of less than 40 mm and a thickness of less than 30 mm, we see that our brake has the highest torque-to-mass ratio and lowest time constant, rendering it useful for haptic or wearable robotic applications.

3.3 MR Brake Design

As seen in Fig. 3.1, the MR brake has two major components: the rotor and the housing. The rotor encapsulates the current-carrying coils (purple) and consists of a low-carbon steel body (orange) broken up by an aluminum ring (blue) on each face (top, side, and bottom). The aluminum rings were bonded to the steel components of the rotor using cyanoacrylate adhesive. A chamfer on both the top edges of the aluminum rings and the top edges of the steel components allowed a channel for the glue to bond the two components firmly together. Great care was taken once the adhesive cured to remove any excess material from the surface of the rotor so that dimensional tolerance could be maintained. The housing consists of two low-carbon steel endcaps (tan) inset into an outer structure, and a low-carbon steel cylindrical shell (green). The rotor is held within the housing by the two endcaps, which contain bronze bushings to allow rotation between the rotor and the housing, and the brake is all held together by eight bolts equally spaced around the perimeter of the housing. A thin gap of 0.1 mm surrounds the rotor on each of its faces and is filled with MR fluid (∼0.16 ml). To ensure no fluid leakage, a small amount of silicone glue was applied between the mating surfaces of the shell and the outer end pieces.

As stated above, we incorporated the coils into the rotor. This unique design can be referred to as an inverted disk-drum combination brake since both disk and drum-type designs incorporate the coils into the housing. By doing this, we move the shear surface to the furthest edge of the brake in the radial direction to lengthen the moment arm and enhance the braking torque (see Fig. 3.1B). Due to this design decision to incorporate the coils into the rotor, the rotor must remain stationary while the housing rotates around it, in

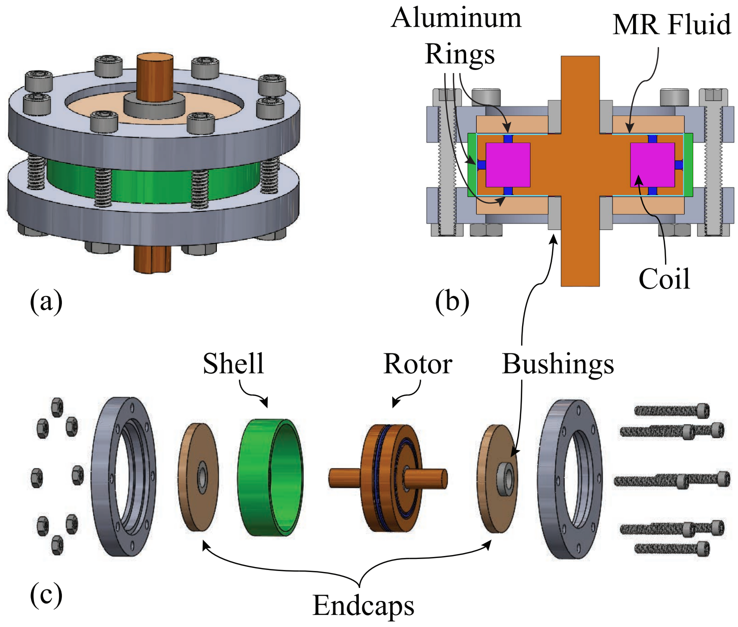

Figure 3.1: CAD drawings of three different views of the MR brake assembly: (a) Assembled view, (b) cross-section view, and (c) exploded view. In (b), the current-carrying coils are colored purple within the low-carbon steel rotor, colored orange. Aluminum rings, colored blue, are embedded into the rotor. The outer housing consists of a low-carbon steel ring shell, colored green, and two low-carbon steel endcaps, colored pale orange. MR fluid, colored cyan, resides in the thin gap between the rotor and the housing, and the entire housing is held together by two aluminum end pieces, which are secured with eight bolts that surround the assembly.

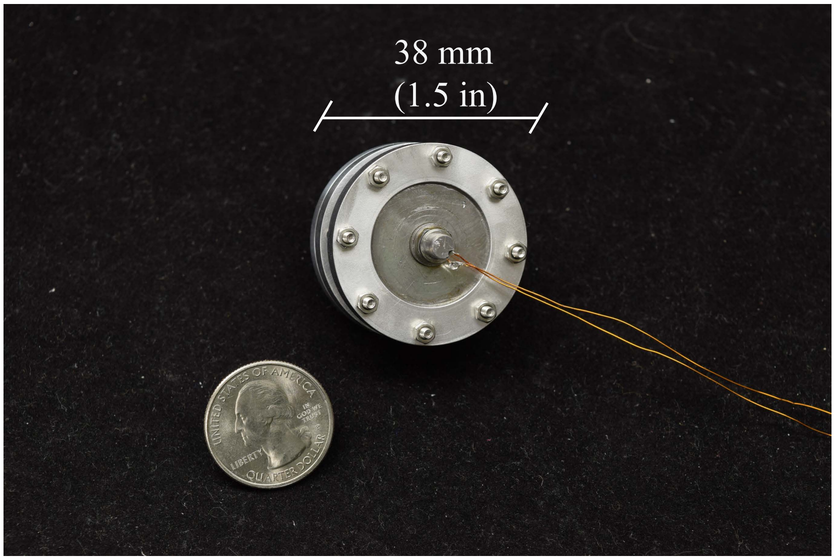

Figure 3.2: The small size of the actual MR brake is highlighted here and compared to the size of a US quarter.

order to keep the wire leads from twisting. This may introduce undesirable rotary dynamics in a large brake, but given its small size and light weight, which is slightly larger than the diameter of a U.S. quarter (Fig. 3.2) and weighs only 67.8 grams, the rotation of the housing around the rotor does not cause significant undesirable dynamics in the brake. The current-carrying coils are made up of approximately 300 turns of 30 AWG magnet wire spooled around the rotor.

In addition to increasing the moment arm and number of shear surfaces within the brake, we incorporated a serpentine flux path to increase the number of crossings the magnetic field has within the MR fluid, which ultimately increases the braking torque (see Fig. 3.3). This is done by incorporating aluminum rings into the rotor to alter the flux path generated by the coils. Since the surrounding low-carbon steel within both the rotor and endcaps of the outside housing have a relative permeability orders of magnitude larger than aluminum, magnetic field lines tend to concentrate within the higher permeability steel, rather than the low permeability aluminum. By adding an aluminum ring to each face of the rotor, the magnetic flux path is guided to cross the MR fluid gap a total of six times. In comparison to a traditional disk-type or drum-type MR brake, which has only two magnetic flux crossings [66], this design feature significantly increases the magnetic flux density in the MR fluid and further increases the braking torque. The number of crossings is limited by the small brake size constraint as well as tight manufacturing tolerances of such small parts, but by incorporating the coils into the rotor and using a disk-drum combination MR brake design, we increased the number of crossings to two on each face of the rotor (top, side, bottom), for a total of six crossings.

The design was modeled and improved through iteration using the magnetostatic module of ANSYS finite-element method (FEM) software (ANSYS, Inc., Canonsburg, PA, USA) (see Fig. 3.4). All material and magnetic properties, including the magnetic flux density vs. magnetic field strength (B-H) curve for the MR fluid (MRF-140CG; Lord Corporation, Cary, NC, USA), were entered into the software to perform the simulation. Graphs of the MR fluid magnetic properties are included in Fig. 3.5 (B). An axisymmetric model was used to reduce computation, and the mesh resolution was increased until the solution converged (99,721 nodes and 54,092 elements). To perform the simulation, the model consisted of an electromagnetic coil of 296 turns, and a 0.5 Amp current was set. Our design goal was to increase the braking torque while keeping the brake as small as possible. The design target was constrained to 38 mm diameter by 14.5 mm width maximum, as this approximate size was consistent with other small brakes both in literature and available commercially.

To increase braking torque, one must 1) increase magnetic flux density within the MR fluid. This is done both by increasing the number of turns of the coil and increasing the steel within the rotor width to the point of diminishing returns. Note that there is an inherent trade-off between space allowed for coils versus steel to carry the subsequent magnetic flux created. 2) Increase the rotor diameter as much as allowable by the size constraints. 3) Decrease the fluid gap size to force magnetic flux through the fluid since the relative permeability of the MR fluid is much smaller than the surrounding steel. Song et al. performed

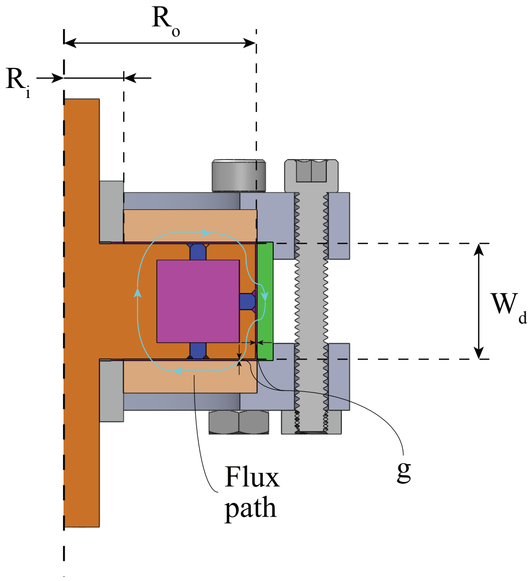

Figure 3.3: Schematic of MR brake design which includes dimensional callouts and the approximate magnetic flux path. R_i and R_o are the inner and outer radii of the disk, respectively. $R_o - R_i$ is the length of the active MR fluid region on the top and bottom of the disk. W_d is the width of the active MR fluid region of the disk. g is the fluid gap width surrounding the disk on the top, bottom, and side. The aluminum rings embedded in the rotor, shown in blue, cause the flux path to cross the fluid gap a total of six times in the given cross-section.

an extensive study on the influence of gap size (among other variables) on the braking torque, and found that generally, braking torque increases with smaller gap size [88]. Due to this finding, a fluid gap of 0.1 mm was chosen for this design, although the actual gap size tolerance could be slightly manipulated based on the tightness of the eight surrounding screws. 4) Decrease the width of the aluminum rings until the magnetic flux density within the rings noticeably increases (the result of a larger concentration of magnetic field lines crossing through the rings as opposed to the fluid, which is not the desired effect here).

To further improve the magnetic flux density within the fluid, we sought the largest current density subject to overall rotor dimension constraints. This led us to select 30 AWG magnet wire for the coil because it would allow for the most turns without significant thermal buildup. The rotor spool was wound with approximately 300 turns of wire. As stated, to increase braking torque by increasing the rotor radius and width, the coils were

Table 3.1: MR Brake Constant Variables

Variable	Description	Value (mm)
Ri	inner radius	4
Ro	outer radius	12.8
Wd	width of drum	7.7
g	thickness of gap	0.1

integrated into the rotor. This extended the moment arm and allowed the brake dimensions to be controlled by rotor size. Consequently, a larger rotor means more turns of wire and a stronger magnetic field, all of which work to increase the braking torque.

Thus, with the above goals and bounds, ANSYS was used to measure the magnetic flux density within the MR fluid gap for each design iteration. Subject to the main constraint of a maximum diameter of 38 mm and height of 14.5 mm, for each design iteration, the following variables were incrementally changed until improvements to the magnetic flux

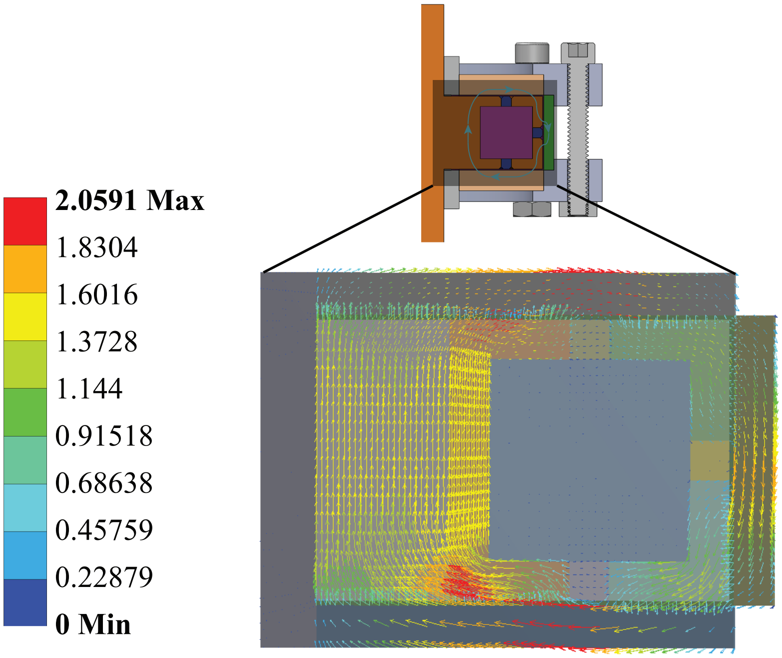

Figure 3.4: FEM of the magnetic flux density through a wedge of the brake. Note that the lines of magnetic flux are forced to cross the MR fluid gap six times within this cross-section, which increases both the magnetic flux density within the MR fluid and the braking torque.

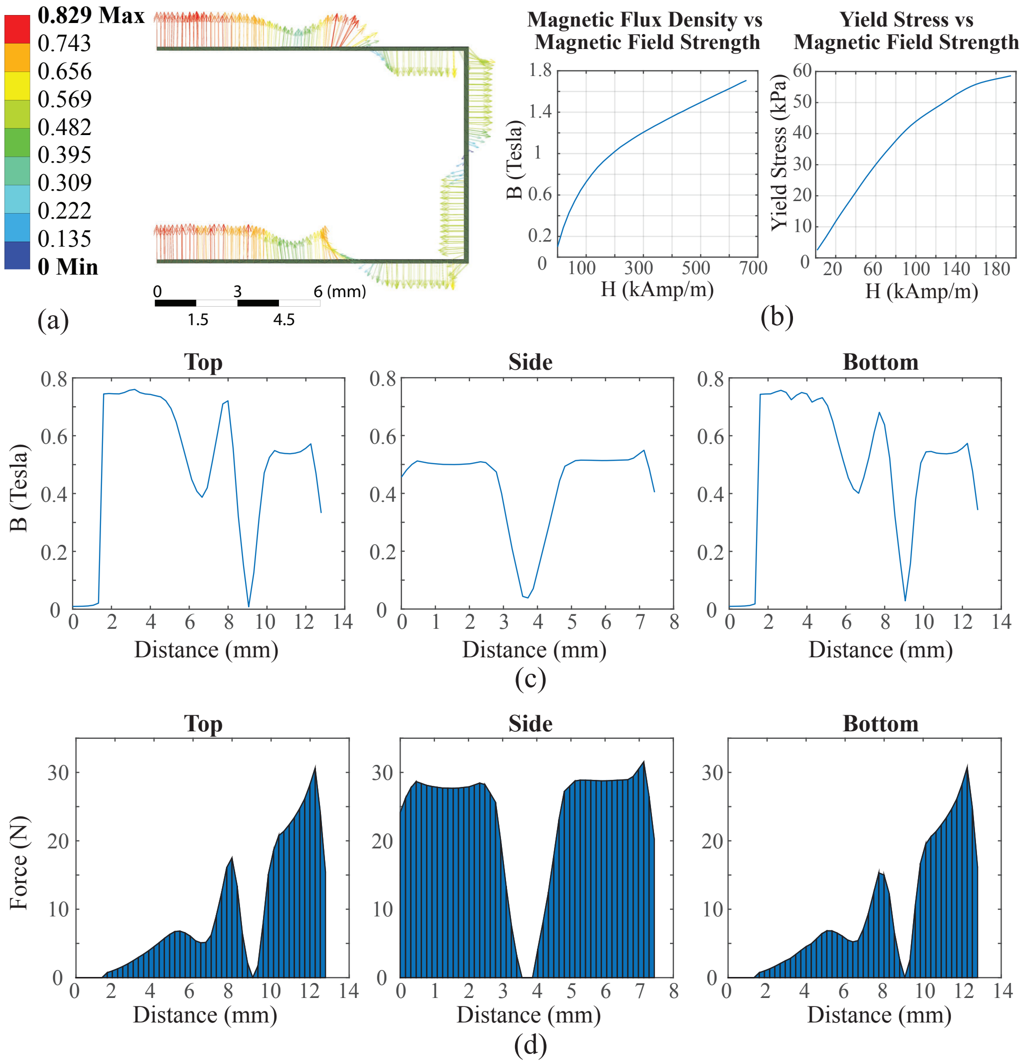

Figure 3.5: (a) Magnetic flux density within the MR fluid from FEA in the ANSYS model of the MR brake. The magnetic flux density values here correspond to 0.5 A within the current-carrying coils. Using these values along with the (b) B-H curve (magnetic flux density vs magnetic field strength) and yield stress vs magnetic strength graph for the MR fluid used (MRF-140CG, LORD Corporation, Cary, NC, USA), an estimate for the braking torque was calculated using (3.3). (c) Shows a plot of the magnitude of the magnetic flux density as a function of its position along the MR fluid gap for each shear surface (Top, Side, and Bottom). (d) Shows a plot of the numerical integration used to solve (3.3) for the braking torque. The trapezoidal estimation function (MATLAB) was used to find the area under the curve, and a braking torque of 409 N·mm at 0.5 A was estimated when all three braking torque contributions (Top, Side, and Bottom) were combined. For the top and bottom shear surfaces, the distance on the x-axis refers to the distance from the centerline of the rotor shaft. For the side shear surface, distance refers to the position along the width of the brake from top to bottom.

density within the MR fluid gap were negligible: the number of turns of the coil, the thickness of the steel endcaps, the thickness of the outer steel shell, the cross-sectional area and spacing of the aluminum rings, and the MR fluid gap size. Following FEM, the largest magnetic flux density values were found using an outer steel shell thickness of 0.042" ($\sim$1 mm), a steel endcap thickness of 0.085" ($\sim$2 mm), an aluminum ring cross-sectional area of 0.042" x 0.042"($\sim$1 mm x $\sim$1 mm), and a fluid gap of 0.1 mm.

The braking torque can be theoretically derived by integrating the shear stress along the rotor surface area:

$$T = 2\int_{R_i}^{R_o} \tau(2\pi r) r dr + \int_0^{W_d} \tau(2\pi R_o) R_o dw + T_{fric} \tag{3.1}$$

where T is the total braking torque, τ is the shear stress of the MR fluid, R_i and R_o are the inner and outer radii of the disk, respectively, W_d is the width of the active MR fluid region of the side of the disk, and T_{fric} is the additional torque due to friction within the brake either between the rotor and the bushings or between the rotor and housing due to tight manufacturing tolerances. The first integration term is the braking torque of the top and bottom surface of the rotor, and the second integration term is the braking torque on the side surface. The behavior of MR fluids is often modeled as a Bingham plastic with variable yield strength [90], therefore the shear stress, τ, can be modeled by Bingham's equations:

$$\tau = \tau_{yd}(H) + \eta \frac{\omega r}{g} \tag{3.2}$$

where τ_{yd} is the dynamic yield stress, which is a function of the magnetic field strength, H, η is the fluid viscosity, ω is the angular velocity, r is the radius of the disk, and g is the fluid gap. After substituting (3.2) into (3.1) and simplifying, the total braking torque becomes:

$$
\begin{aligned}
T =& 4\pi \int_{R_i}^{R_o} \tau_{yd}(H(r))r^2 dr \\
&+ 2\pi {R_o}^2 \int_{0}^{W_d} \tau_{yd}(H(w))dw \\
&+ \pi\eta \frac{\omega}{g}[({R_o}^4 - {R_i}^4) + 2{R_o}^3 W_d] + T_{fric}
\end{aligned}
\tag{3.3}
$$

The first integration term accounts for the braking torque from the top and bottom surfaces of the rotor, while the second integration term is the braking torque from the side surface of the rotor. The third term is the contribution of the viscous flow on all three surfaces of the rotor. Since the viscous flow is proportional to the rotational speed of the brake, this term need only be used if operating the brake at fast speeds. Most likely, for the applications proposed for this specific brake such as haptics or human-robot collaborative devices, the brake will be operating at slow speeds and this term may be neglected.

By using (3.3) in conjunction with the FEM, we can calculate an estimate for braking torque after each incremental change to the design. Thus, by changing the variables outlined earlier (i.e. number of turns of the coil, thickness of the steel endcaps, etc.), we were able to improve the braking torque until further changes resulted in negligible braking torque improvement. The output of the FEM, which is shown in Fig. 3.5 (A, C), is the magnetic flux density within the MR fluid gap as a function of distance along the fluid length. These magnetic flux density values could be converted to yield stresses using the magnetic relationships shown in Fig. 3.5 (B), and then used directly in (3.3). Numerical integration must then be used to solve for the braking torque according to the model since the yield stress changes along the MR fluid gap radius. A current of 0.5 A through the current-carrying coils was used during the design process to compare different design iterations. For the final design shown here, the modeled braking torque to an input of 0.5 A was calculated to be 409 N·mm, with 117.5 N·mm, from the top/bottom and 174 N·mm from the side. Experiments to test the validity of this value and further characterize the MR brake are shown below.

3.4 MR Brake Experiments

To test the braking torque and system dynamic response characteristics (i.e. step response and frequency response) of the MR brake, we created a custom dynamometer setup (Fig. 3.6). To do this, we attached a brushed DC motor (Maxon Precision Motors, Inc., Fall River, MA, USA) to the housing of our MR brake and then coupled the rotor of the MR brake to a Mini40 torque sensor (ATI Industrial Automation, Apex, NC, USA). The DC motor was sized such that it would not stall during experimental testing with the brake outputting its maximum torque. To control the current supplied to the MR brake, we used

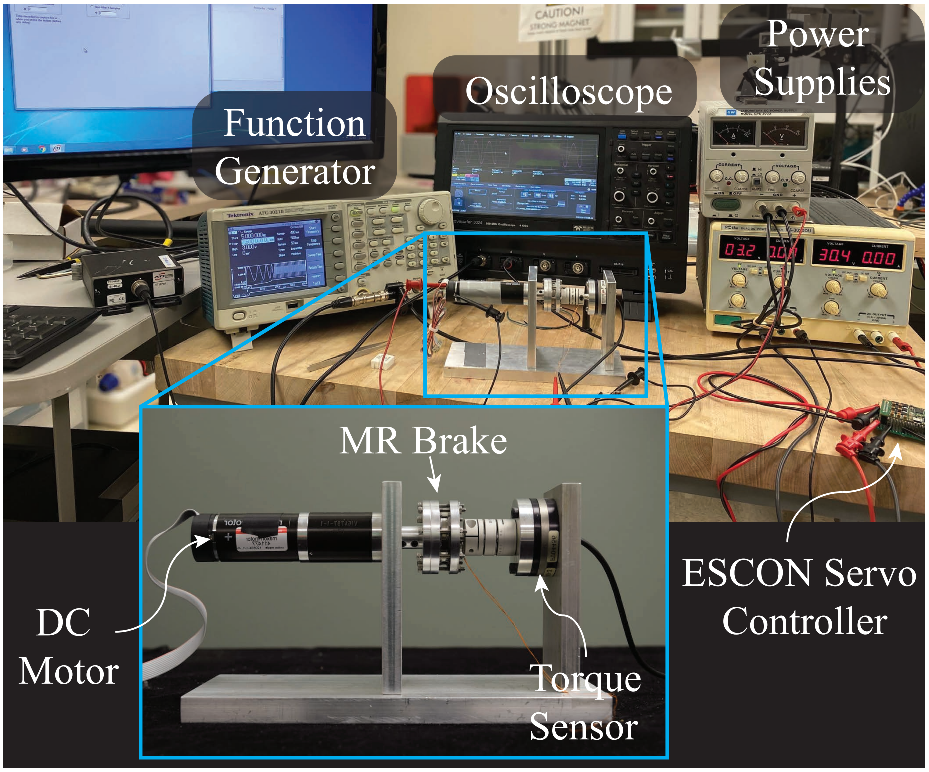

Figure 3.6: Experimental setup for testing the braking torque of our MR brake. The test bed includes a DC motor attached to the MR brake and a torque sensor to capture the braking torque. A DC power supply drove the motor and supplied 30V to an ESCON 50/5 servo controller, which controlled the current supplied to the MR brake. An oscilloscope was used to capture both the actual current supplied to the MR brake and the voltage supplied by a function generator for system dynamic response testing.

an ESCON 50/5 Module servo controller supplied with 30V from a 30V/3A DC power supply (PS-3030DU; Uniteq Corporation). Given a voltage input from a function generator (AFG 3021B; Tektronix, Beaverton, OR, USA), the ESCON servo controller supplied a current to the brake defined by a voltage-to-current ratio configured using the ESCON Studio software. An oscilloscope (WaveSurfer 3024; Teledyne Lecroy, Chestnut Ridge, NY, USA) was used to capture data on the current supplied to the MR brake as well as signals from the function generator used during the system dynamic response testing.

3.4.1 Braking Torque

The first set of experiments was aimed at establishing the braking torque output of our MR brake. There were three goals to these experiments: 1) establish a relationship between input current and output torque, 2) from this relationship, find the magnetic flux saturation limit, and 3) determine the best current input for our MR brake. To accomplish the first goal, we measured the braking torque of the MR brake at currents ranging from 0 to 1.4 A in 0.1 A intervals (see Fig. 3.7). Each braking torque experiment began with the DC motor freely spinning the MR brake housing. Then, the brake was engaged by supplying the current-carrying coils within the brake with a specified current, and the torque was measured using the force/torque sensor. Without the brake engaged, we measured approximately 15 N·mm of frictional torque within the brake. This can be attributed to friction between the shaft and bushings and the MR fluid. Since the gap between the rotor and the housing where the MR fluid resides is small (0.1 mm), there is a possibility that some friction is caused by the interaction between the rotor with the housing. From Fig. 3.7, we see that there is an approximately linear relationship between current and braking torque for input currents less than 0.5 A (R^2 = 0.995). Above 0.5 A, magnetic saturation begins to take place within the steel flux path, which limits the braking torque output. By 1.4 A, the MR brake is at its braking torque limit; the steel flux path has reached full magnetic saturation. Thus, 0.5 A is the best input current for large torque without significant thermal buildup. Based on this, we limited the input current to 0.5 A in subsequent experiments to avoid excessive thermal buildup. The results in Fig. 3.7 show the controllability of our MR brake, determined experimentally. At the 0.5 A level determined above, our MR brake produces approximately 462 N·mm. Comparing this value to the modeled braking torque estimation found at the end of Section 3.3, we see that the results vary by 53 N·mm. This is most likely caused by unmodeled friction within the brake.

3.4.2 Hysteresis Characteristics

Hysteresis is a potential problem in the control of MR brakes since it leads to a nonlinear relationship between input current and output braking torque. The presence of ferromagnetic materials within the brake, which are necessary to carry the magnetic flux, are responsible for this hysteretic behavior since the materials inherently have a nonlinear re-

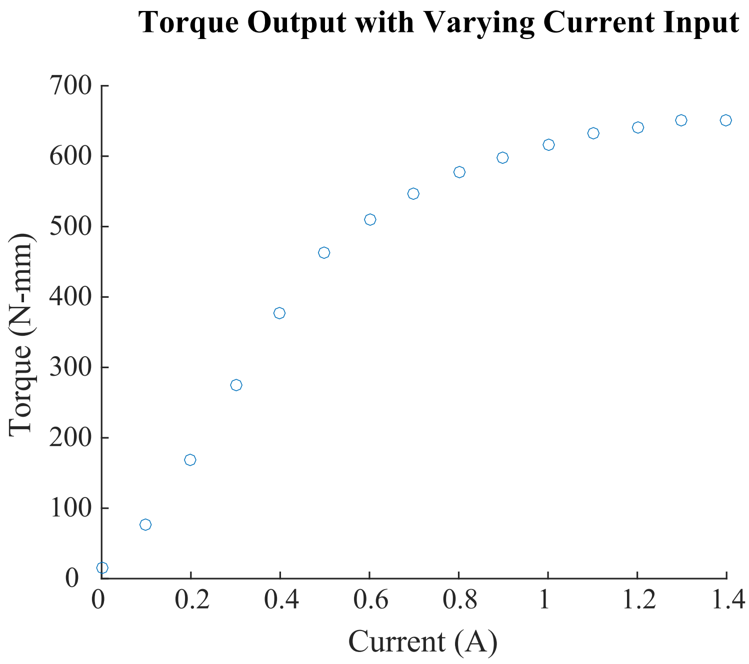

Figure 3.7: Results of MR brake testing to establish the braking torque output. The input current was varied from 0 to 1.4 A in steps of 0.1 A and the braking torque recorded. The relationship was approximately linear below 0.5 A, and then becomes nonlinear due to magnetic flux saturation.

lationship between magnetic flux density (B) and magnetic field strength (H) [69]. In the following experiment, we aimed to characterize any hysteresis that may be present within the MR brake that leads to a nonlinear relationship between input current and the output braking torque. With the brake rotating at 55 rpm, a step current input was commanded to the brake in increments of 0.1 A and the braking torque was recorded at each current step. This test was performed twice; the first time increasing the current to 0.8 A to create a major hysteresis loop and the second time increasing the current to 0.5 A to create a minor hysteresis loop. In Fig. 3.8, the major and minor hysteresis loops are indicated by the diamond and circle markers, respectively, and the rising currents are the blue lines, while the falling currents are the red lines. As seen in Fig. 3.8, with a higher supplied current, the magnetic hysteresis loop is larger due to the larger residual flux within the ferromagnetic

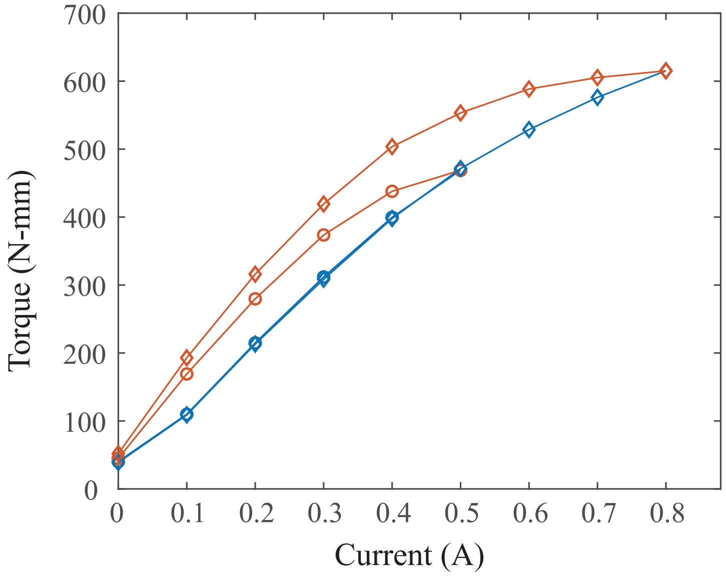

Figure 3.8: This shows the hysteresis present within the MR brake. Step inputs of current were commanded to the brake in 0.1 Amp increments and the braking torque at each step was recorded. A major and minor hysteresis loop are shown here, as indicated by diamond markers and circle markers, respectively. The major loop goes to a maximum current of 0.8 A, then returns to 0 A, and the minor loop goes to a maximum of 0.5 A, then returns to 0 A. In each loop, the blue line indicates the rising current and the red line indicates the falling current.

housing materials of the brake creating higher braking torques as the current is commanded back to zero. By operating the brake at a current of 0.5 A and below, which is below the current level where magnetic saturation starts to take effect, as found in 3.4.1, the hysteresis loop becomes significantly smaller, reducing the nonlinearity between current and braking torque.

3.4.3 Step Response

An experiment to characterize the transient response of the MR brake to a step current input started with the motor rotating the MR brake freely at 55 rpm. At 2 seconds, a step current input of 0.5 A was sent to brake by the ESCON 50/5 servo controller, and the resulting rise in braking torque was recorded. In Fig. 3.9, the transient response of the braking torque to the 0.5 A is shown by the blue line. After a very quick initial rise in braking torque (time constant – 63.2% response – of 3.9 ms), which is due to the fast rise in current supplied by the ESCON servo controller, slower particle dynamics within the brake are present as it reaches its final value. The rise time of the brake, defined as the time required for the response to rise from 10% - 90% of the final braking torque, is approximately 35 ms. In addition to the braking torque, both the commanded current step and transient response of the current within the MR brake are plotted in Fig. 3.9 with a dotted and solid red line, respectively. These were captured together using an oscilloscope so that the commanded step input and actual current could be aligned. The inset graph zooms in on the transient response of the current and shows a comparison between the rate of change of the current within the brake and the actual braking torque. A faster rise time of the current (0.61 ms for 0% - 100%) compared to the braking torque indicates a mechanical limit to the rate at which the braking torque increases.

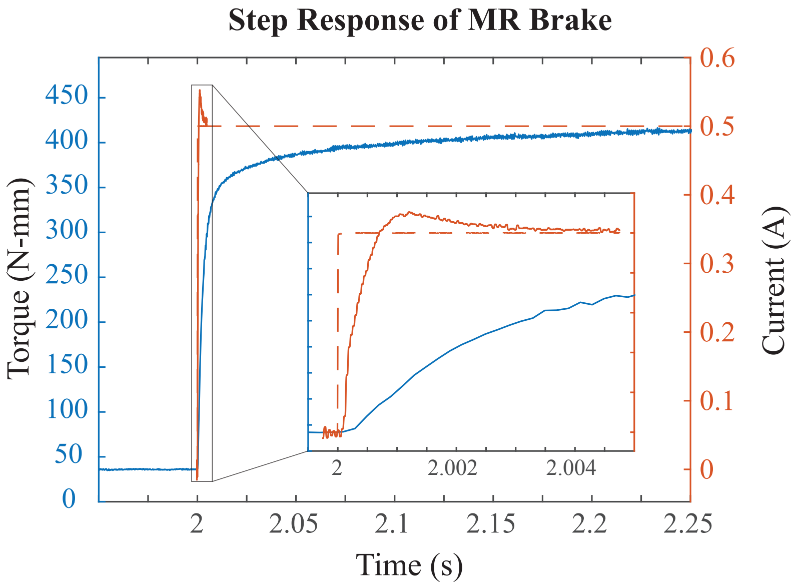

Figure 3.9: The braking torque response (blue line) to a step input of 0.5 A (dotted red line) at 2 seconds. The solid red line shows the rise of the actual current within the brake, which rises at a faster rate than the braking torque. After a quick initial rise in braking torque (time constant of 3.9 ms), slower particle dynamics can be seen. The rise time (10% - 90%) of the braking torque is approximately 35 ms. The rise time (0% - 100%) of the current within the MR brake is 0.61 ms. The inset graph zooms in on the rising portion of the current and shows the comparison in the rate of change between the current and the braking torque.

3.4.4 Frequency Response

To characterize the frequency response of the MR brake, a sinusoidal waveform of 1.5 + 1.5sin(ωt) V from the function generator was commanded to the ESCON 50/5 servo controller, which corresponded to a 0.25 + 0.25sin(ωt) A wave being sent to the MR brake (the servo controller was configured such that a 3.0 V input signal to the controller was equal to a 0.5 A output signal to the MR brake). Fig. 3.10 shows the torque tracking of the MR Brake in the time domain. Fig. 3.11 shows the frequency response for the ESCON servo controller output current to the input voltage from the function generator, the braking torque output to the ESCON servo controller input current, and the braking torque output to the input voltage of the function generator. The bandwidth (-3 dB) of each is 728 Hz, 62 Hz, and 65 Hz, respectively. By identifying the asymptotic behavior of each plot, transfer

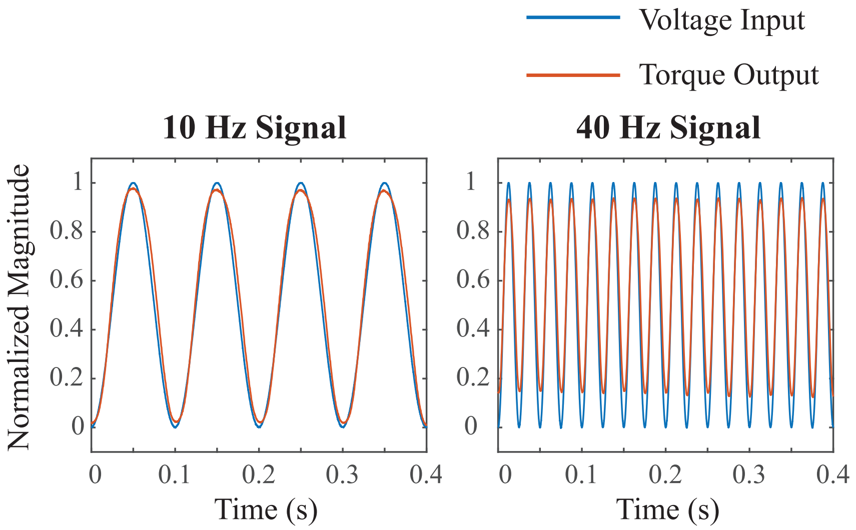

Figure 3.10: The torque tracking of the MR brake to a 10 Hz and 40 Hz sinusoidal voltage input. Here the voltage input corresponds to a 0.5 A magnitude sinusoidal output from the current controller. The magnitude of each wave was normalized. Since the bandwidth of the frequency response was 65 Hz, the magnitude of the braking torque output begins to decrease as the frequency of the input signal increases.

functions for the ESCON controller (G_1(s)), MR brake (G_2(s)), and full system (G(s)) were obtained:

$$G(s) = G_1(s)G_2(s) \text{ , where} \tag{3.4}$$

$$G_1(s) = \frac{901.9(s+900)}{(s+1050)(s+4500)} \tag{3.5}$$

$$G_2(s) = \frac{3.27\times 10^5}{s+500} \tag{3.6}$$

In Fig. 3.11, the frequency response magnitude plot of each transfer function is shown as the black line overlaid on the experimental data.

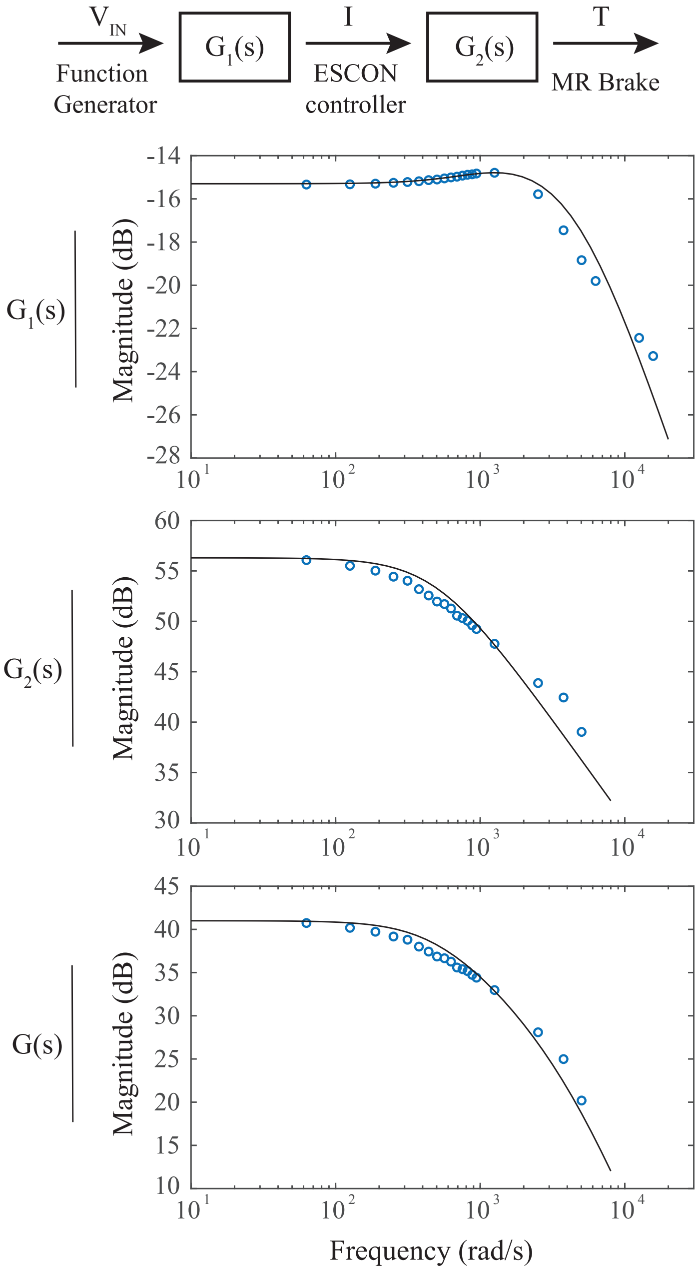

Figure 3.11: This shows the frequency response of the current output of the ESCON 50/5 servo controller to a voltage input by the function generator, the braking torque output to a current input, and the braking torque output to a voltage input, respectively. The frequency ranged from 10 Hz up to a maximum of 2500 Hz (31.4 rad/s to $1.57 \cdot 10^4$ rad/s). The bandwidth (-3 dB) of each was approximately 728 Hz, 62 Hz, and 65 Hz, respectively. The black line on each plot represents the frequency response of the transfer functions obtained from this analysis, shown in (3.4)-(3.6).

3.5 Comparison with Existing Miniature Brakes

Based on the above experiments, our brake can be compared with similarly-sized brakes, both in the literature and in commercial use. Table 3.2 shows a comparison between several different types of small brakes, including electromagnetic (EM), magnetic particle (MP), hysteresis (HB), piezoelectric (PZT), and magnetorheological (MR). Note that TVR and TMR stand for Torque-to-Volume ratio and Torque-to-Mass ratio, respectively.

Of all the brakes, the PZT-actuated proportional drum brake had the fastest response, with a 2.6 ms rise time [61]. Our MR brake had a rise time of approximately 35 ms, which is slightly slower than the EM brake, but faster than the MP brake (note: rise time for the MP brake was taken from experimental data on the slightly larger Model: B2 from [61] since the rise time is not listed on the data sheet.) All rise times included in Table 3.2 were defined as the time required to rise from 10% to 90% of the final braking torque value.

Looking at the braking torque of each brake, we see that the EM brake from Magneta has the highest torque output at 600 N·mm. Next on this list as well is our MR brake with a braking torque output of 462 N·mm. Adjusting for the size of the brake, our MR brake has the greatest torque-to-volume ratio among the small-scale brake types identified. The closest comparable brake in both size and torque output is the electromagnetic brake from Magneta, but one inherent advantage of the MR brake versus the EM brake is that the MR brakes output torque is fully controllable. In contrast, an EM brake whose current-torque relationship is highly non-linear, the braking torque of the MR brake can be controlled by varying the input current. This feature, along with the fast response time, makes our MR brake extremely favorable for haptic applications.

Table 3.3 provides a comparison between small MR brakes found in the literature. As stated above, small brakes within this Chapter are defined as those with a diameter of less than 40 mm and a width of less than 30 mm. The hollowed multi-disk brake has the greatest maximum torque and greatest TVR of all those compared. Our brake has the greatest TMR and fastest time constant. It is interesting to note the fast time constant of

Table 3.2: Brake Comparison Among Different Types of Small-Scale Brakes

	Ours	Magneta	Placid Industries	Magtrol	Gogola et al. [61]
Type/Architecture	MR	EM Model: 14.110.02.103	MP Model: B1	HP Model: 3M	PZT
Torque (Nmm)	462	600	113	20	180
Diameter (mm)	38	39	40	31.8	71
Width (mm)	14.5	19	27	18.6	38
Volume (mm^3)	16445	22697	33929	14772	150449
TVR $* 10^{-3}$ (N/mm^2)	28.1	26.4	3.3	1.4	1.2
Mass (g)	68	63	255	110	560
TMR (Nmm/g)	6.79	9.52	0.44	0.18	1.64
Rise Time (ms)	35	15	100[a]	-	2.6

[a] Model: B2 rise time from [61]

Table 3.3: Brake Comparison among Small-Scale Magnetorheological Brakes

	Ours	MR Brake [79]	MR Brake [85]	MR Brake [91]	MR Brake [92]
Type/Architecture	Inverted Hybrid	Drum	Multi-Drum	Hollowed Multi-Disk	Multi-Disk
Torque (Nmm)	462	189	403[a]	1080[a]	480[a]
Diameter (mm)	38	25	28	39.5	36
Width (mm)	14.5	18	23.5	25	18
Volume (mm^3)	16445	8836	14470	26700[c]	18322
TVR $* 10^{-3}$ (N/mm^2)	28.1	21.4	27.9	40.4	26.2
Mass (g)	68	84[b]	105	232	130
TMR (Nmm/g)	6.79	2.25	3.84	4.66	3.69
Time Constant (ms)	3.9	67	54	-	60

[a] Saturation torque

[b] Includes gear train

[c] Volume reduced by hollow core

our brake compared to the others. We suspect that since the rise time of the MR fluid is a couple of milliseconds, electrical dynamics associated with the power supply used may be responsible. On another note, there is a tradeoff between the inductance of the coil and the brake response time. The main goal of the design described in this Chapter was to increase the braking torque as much as possible given its size. As such, the maximum number of coils that would fit within the rotor was used rather than choosing a specific inductance. Since the rise time of the current into an inductive load is subject to both the inductance and the maximum output voltage of the source, we chose to control the current with a large voltage source so that we could still have a fast response for a set coil inductance. As stated in the Step Response subsection of the Experiments, our MR brake experienced a quick initial rise in braking torque before the slower particle dynamics within the brake took over until it reached its final value. We believe the fast response is in part due to the brake dynamics and in part due to the addition of the current controller (ESCON 50/5), which can supply a very sharp current step to the brake before settling to the commanded current. Overall, having the greatest TMR and fastest time constant among the small MR brakes compared here makes our MR brake well-suited for haptic or wearable robotic applications.

3.6 Conclusion

Designed as a blend of both a disk and drum-type brake, our magnetorheological brake (MR) utilizes a serpentine magnetic flux path to obtain high braking torque by creating a shear surface on all three surfaces of the rotor. To increase braking torque, we inverted the traditional placement of the current-carrying coils and put them within the rotor rather than the housing. This MR brake offers a combination of high braking torque and fast response, in a small form factor.

For the implementation of the brake into a surgical robotic system, for example, additional testing on the specific magnetorheological fluid used would be useful. Minimizing sediment formation and long-term braking torque degradation would be advantageous, and it is something that will need to be explored in the future with high-cycle and shelf-life testing. Additionally, further analysis of the effect of the fluid gap size on the braking torque of our brake should be explored in future work. While studies show that decreasing fluid gap size will generally increase braking torque [88], too small of a gap can cause manufacturing tolerance problems and may even decrease the braking torque if below a critical point. While the fluid gap size in this Chapter seeks to balance these competing objectives, the size has not been rigorously studied or optimized for our brake.

Based on the high braking torque, fast time constant, and small size, our new brake is well-suited for future applications in haptic devices, especially in wearable or handheld mechatronic systems. By implementing brakes into the joints of a robotic system that is cooperatively controlled by a human user, hard stops can be applied to display haptic objects or prevent the user from accessing areas of the workspace that should be avoided. As an inherently passive device, the brake cannot impart any energy into a robotic system. Thus, this MR brake design enables the cooperatively-controlled, passive device discussed below in Chapter 4.

Chapter 4

An Intrinsically Safe Collaborative Surgical Robot for Mastoidectomy

4.1 Chapter Overview

While the automated approach in Chapter 2 shows many benefits including accuracy, repeatability, and patient-specific path adaptation, clinical translation of the device relies on adoption by medical professionals. Since mastoidectomy is currently performed manually, the barrier to adoption is higher for an automated approach than for a cooperative approach that does not take the drill control out of the surgeon's hands. Also, an automated approach is subject to higher scrutiny and harsher regulations which would delay clinical adoption. Perhaps the cooperative approach yields a faster route to clinical adoption since the surgeon remains an active participant in the surgery as normal. For this reason, a cooperatively controlled approach for mastoidectomy is discussed in Chapter 4.

Using the MR brake described in Chapter 3, a design for a cooperatively controlled, passive robot for mastoidectomy was developed. Designed to be a bone-attached cooperative robot for otologic surgery, it has the ability to be more accurate with a smaller footprint than existing systems in literature for assisting with mastoidectomy. Compared to an automated system, this device gives the power back to the surgeon. As an inherently safe device that can only inhibit motion, it does not impart any motion of its own onto the drill. Coupled with image-guidance, the surgeon is provided with subsurface anatomical information as well as an extra safety mechanism that will not allow vital anatomical structures to be damaged. Work described in Chapter 4 depicts the core kinematic unit (CKU) of the cooperatively-controlled robot design, a planar five-bar linkage, which uses two MR brakes at the base joints to control the end-effector (i.e. surgical drill) motion.

4.2 Introduction

The motivation for Chapter 4 is to give surgeons robotic accuracy and enhanced spatial awareness that would allow them to conduct a mastoidectomy safer and more efficiently. While the earliest robotic systems aimed at performing mastoidectomy were automated systems [1, 2, 30], perhaps a more viable approach towards a clinical system is a cooperative robotic system. Cooperative systems allow the surgeon to perform a mastoidectomy just as normal and only intervene if a preoperatively set boundary is crossed. Prior work on cooperative robotic systems has shown them capable of performing mastoidectomy safely using motorized serial arms and active optical tracking [22, 3]. Another cooperative approach simply augments the surgical drill to turn off if it gets too close to a vital structure to avoid damage to it [34]. While it still gives the surgeon full control, the system relies on active optical tracking and could have potential accuracy issues due to registration error or blocked line of sight. A master-slave system, which aims to combine the best of robotic precision and surgical technique, is another consideration for improving mastoidectomy. A group using the da Vinci Surgical System proved the feasibility of this system to perform a mastoidectomy, but they remarked the lack of haptic feedback to the surgeon as a major drawback. Additionally, the procedure time increased significantly [35].

If the goal of the cooperative robotic device for mastoidectomy is to make the procedure as safe as possible for the patient, then a passive device using only brakes to stop drill motion from damaging vital anatomical structures is an inherently safe solution. Passive devices, like brakes or dampers, cannot accidentally move the tool; they can only stop it from moving. Thus, the surgeon is the only one causing tool motion and the robot becomes a safety system that is strictly passive, i.e. it cannot inject energy into the drill-bone-surgeon system. Additional benefits of a passive system are its higher speed and lighter weight than an active motor-controlled robot (brakes can be designed much smaller and lighter for the same torque output compared to motors).

A potential drawback of a passive surgical robot is less control for applying virtual boundaries since you cannot actively push the surgical drill as you could with a motor-controlled system. Several groups have looked into passively creating virtual fixtures, a review of which has a section dedicated to passive constraint enforcing mechanisms [93]. As a method for improving the accuracy of bone segment placement during craniofacial osteotomies, Taylor et al. used mechanical brakes to apply "passive manipulation aids" [94]. Brakes were attached to each decoupled, orthogonal axis of the device. By actuating each brake when the associated manipulator axis was aligned with the target, the manipulator was accurately aligned one axis at a time. In another case, a narrow band was established near the surface of a forbidden zone such that within this band, one brake was pulsed at a time to keep the tip moving along the surface (i.e. creating a virtual wall) [95, 96]. Cho et al. used a concept for active robots, namely the force manipulability ellipsoid, and extended this to passive robots to control the force at the tip and set it to zero, effectively creating a virtual wall [97]. Another mechanism, the Passive Trajectory Enhancing Robot (P-TER), used both brakes and clutches to apply guidance constraints. Gomes et al. implemented a control law that is based on a grid of torques that would be transmitted to the end-effector if each brake/clutch is activated. The combination that best matched the desired output torque was then chosen [98]. Lastly, continuously variable transmissions (CVT) were used within "Cobots" to constrain the relative joint velocities of in a passive mechanism [99, 100]. This approaches the problem from a different perspective than the previously mentioned approaches. A Cobot is a constrained device that, when not interacting with a constraint, has some degrees of freedom simulated. The passive device used in this design uses only brakes and controls them based on proximity to a boundary.

The contributions of this work involve the design of the first bone-attached cooperative robot for mastoidectomy, referred to as the cooperatively-held surgical drill (CoSD), and the development of the CKU of this design, which is a five-bar linkage mechanism utilizing two MR brakes at the base joints. As mentioned in Chapter 1, bone-attached robots eliminate additional errors associated with optical tracking, making the design more precise than serial arms that require tracking of the tool. In addition, the robot is designed to be completely passive with magnetorheological (MR) brakes discussed in Chapter 3, rendering this system inherently safe. While a five-bar linkage is a well-known structure that has been studied in haptic device applications [101], this is the first use in a completely passive structure for surgical milling.

4.3 Design

Design for this robot was driven both by the decision to make it bone-attached and as rigid as possible for the high accuracy required for mastoidectomy, as well as by the limited surgical workspace and need for visibility of this procedure (i.e. a microscope is used for mastoidectomy, therefore a direct line of sight is required to perform the surgery successfully). For rigidity, parallel robotic structures are superior to serial arms, therefore a parallel design that could cooperatively hold the drill along with the surgeon was chosen. While the rigidity of parallel robots adds to the accuracy of the end-effector, often parallel

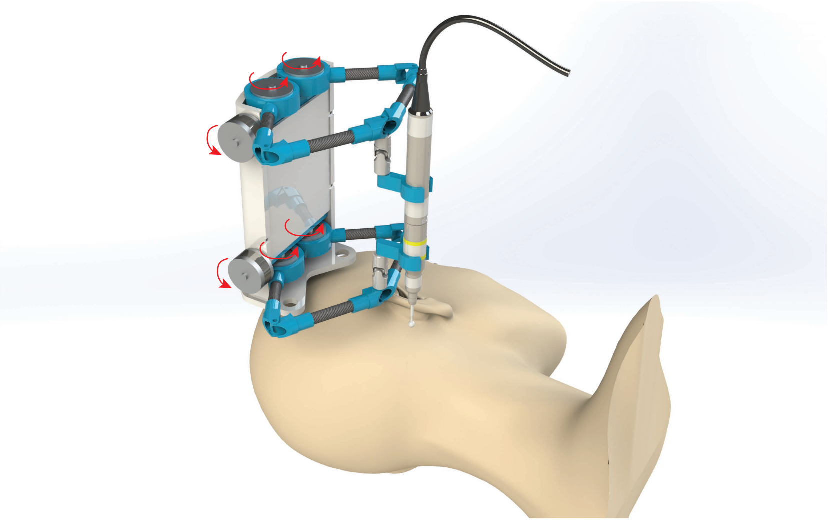

Figure 4.1: A CAD rendering of the cooperatively-held surgical drill (CoSD). The robotic device is bone attached superior to the mastoid region of the temporal bone. The six rotational joints, where the MR brakes from Chapter 3 are located, are depicted by the red rotational arrows. CoSD has five degrees of freedom: three translational and two rotational (the rotation along the drill shaft is omitted because it is not necessary to control the drill).

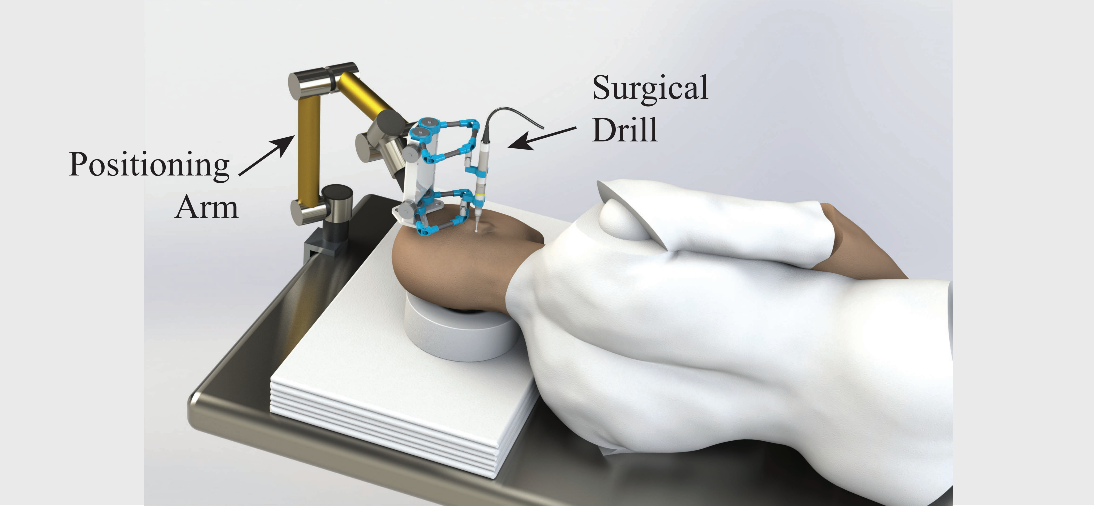

Figure 4.2: This shows the system concept of CoSD. A bed attached robot would help offload some of the weight from the patient as well as add additional rigidity. CoSD is bone attached just above the surgical site, with the surgical drill held right above the mastoid bone to be milled.

robots are quite large compared to their workspace. For a bone-attached robot with a need for visibility of a small surgical workspace, this is a problem that limits potential designs. Therefore after multiple different design considerations, a twin five-bar linkage parallel robot structure that holds the surgical drill at either end was chosen (Figure 4.1).

The device, which is a cooperatively-held surgical drill, or CoSD, is designed to be bone-attached in a similar manner to the Acoustic Neuroma Surgical Robot (ANSR), the design of which was mentioned both in Section 1.2.2 (Figure 1.7) and Section 2.4. A pre-positioning frame (PPF) is attached directly to the patient, superior to the surgical site using three bone screws. On the PPF, there are multiple fiducials that are used both to register the robot to the segmented anatomical structures and as the mounting locations for the robot itself. Forces at the bone screw locations are a major consideration, and to offload most of the weight of the robot as well as add rigidity to the structure, a positioning arm (i.e. a gas spring arm) attaches to the base plate of the robot (Figure 4.2).

A workspace analysis informed the link lengths of CoSD. Prior work by Dillon et al. found that the workspace necessary for a mastoidectomy is approximately an inverted el-

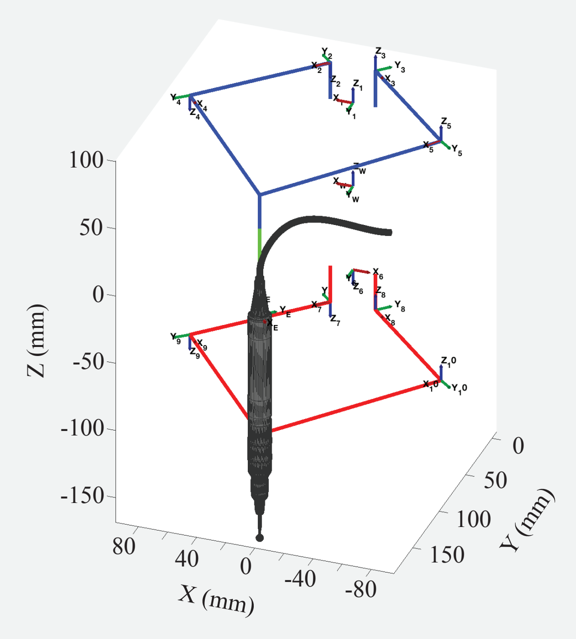

Figure 4.3: Representation of joints and coordinate frames for CoSD. This wire frame was used to analyze the mastoidectomy workspace and find link lengths that could reach all areas of the surgery.

liptical cone with major and minor ellipse diameters 52 mm and 45 mm, respectively, and a depth of 41 mm. Link lengths of CoSD were chosen such that all points within this workspace could easily be reached (Figure 4.3). More on the workspace analysis specific to the five-bar linkage mechanism can be found below in 4.4.

To assist the surgeon further, other than just stopping the motion of the drill if damage to vital anatomy is imminent, an image-guidance display will be overlaid onto the preoperative CT scans, in which vital anatomical structures were automatically segmented and a preplanned drilling volume was manually selected. It is believed that with extra visual feedback of the underlying vital anatomy, the surgeon has the potential to perform the surgery faster and more efficiently since the vital anatomy need not be uncovered before proceeding with the rest of the drilling.

As a first step in developing and testing the CoSD design described above, the rest of Chapter 4 focuses on the development and testing of the CKU of the design (Figure 4.4).

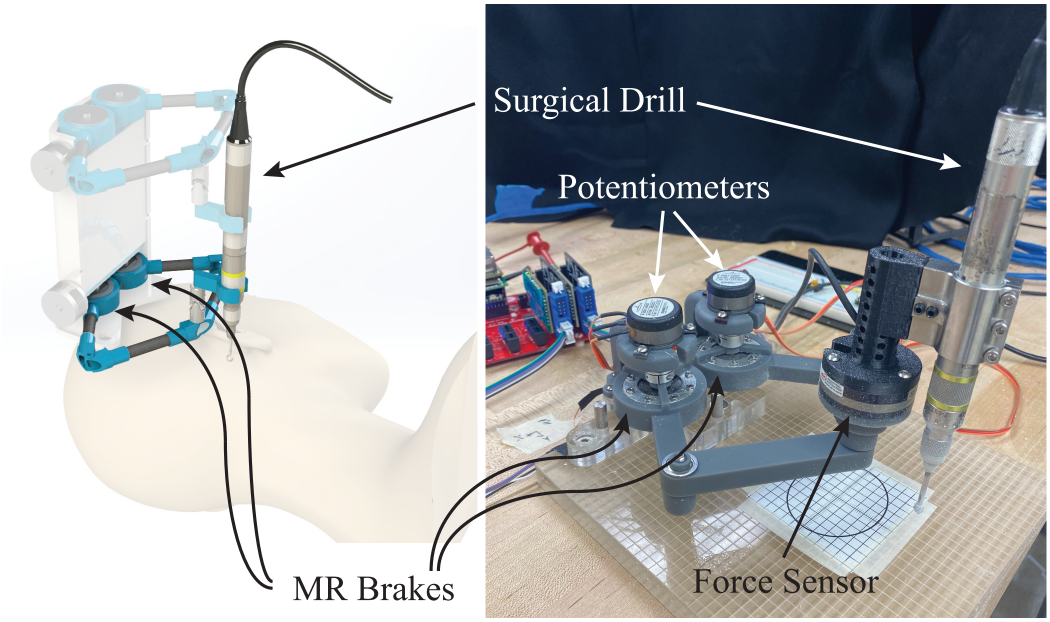

Figure 4.4: This shows the development of the core kinematic unit (CKU) used to test the feasibility of the CoSD design. On the left is the CoSD design, with the CKU highlighted. On the right is the physical development of the CKU.

4.3.1 Forward Kinematics

To control the surgical drill at the end-effector of the five-bar linkage mechanism to within a specified boundary, the end-effector position must be calculated within the control loop. Given base angle readings from potentiometers (Series P2500, novotechnik, Southborough, MA, USA) attached to each MR Brake, the forward kinematics of the robot architecture are used to calculate the end-effector position. Figure 4.5 shows a simplified representation of the five-bar mechanism with the base frame coordinate system, joint positions, and joint lengths labeled. The forward kinematics can be solved from the kinematic constraint equations of each leg of the five-bar mechanism from the base frame coordinate system to the end-effector:

The position of the end-effector is designated by:

$$\mathbf{P} = (x_P \, , \, y_P) \tag{4.1}$$

The position of the points b_1 and b_2 located at the end of link one for each leg can be written as:

$$\mathbf{b_1} = (L_1 \cos q_1 - L_0 \, , \, L_1 \sin q_1) \tag{4.2}$$

$$\mathbf{b_2} = (L_1 \cos q_2 + L_0 \, , \, L_1 \sin q_2) \tag{4.3}$$

where q_1 and q_2 are the active base angle joints for the two legs. Each leg is then subject to the following kinematic constraint:

$$|\mathbf{Pb_i}| = L_2, \qquad \text{where} \quad i = 1,2 \tag{4.4}$$

which can be rewritten to form the following kinematic constraint equations for each leg:

$$\text{Leg 1:} \qquad (x_P - L_1 \cos q_1 + L_0)^2 + (y_P - L_1 \sin q_1)^2 = L_2^2 \tag{4.5}$$

$$\text{Leg 2:} \qquad (x_P - L_1 \cos q_2 - L_0)^2 + (y_P - L_1 \sin q_2)^2 = L_2^2 \tag{4.6}$$

By subtracting (4.6) from (4.5) and simplifying, the new equation can be written in the form:

$$x_P = c \, y_P + d \tag{4.7}$$

where

$$c = \tfrac{L_1(\sin q_1 - \sin q_2)}{2L_0 + L_1 \cos q_2 - L_1 \cos q_1} \qquad\qquad d = \tfrac{L_1 L_0(\cos q_1 + \cos q_2)}{2L_0 + L_1 \cos q_2 - L_1 \cos q_1}$$

Substituting (4.7) into (4.5) and simplifying, the new equation can be written in the form:

$$f \, y_P^2 + g \, y_P + h = 0 \tag{4.8}$$

where

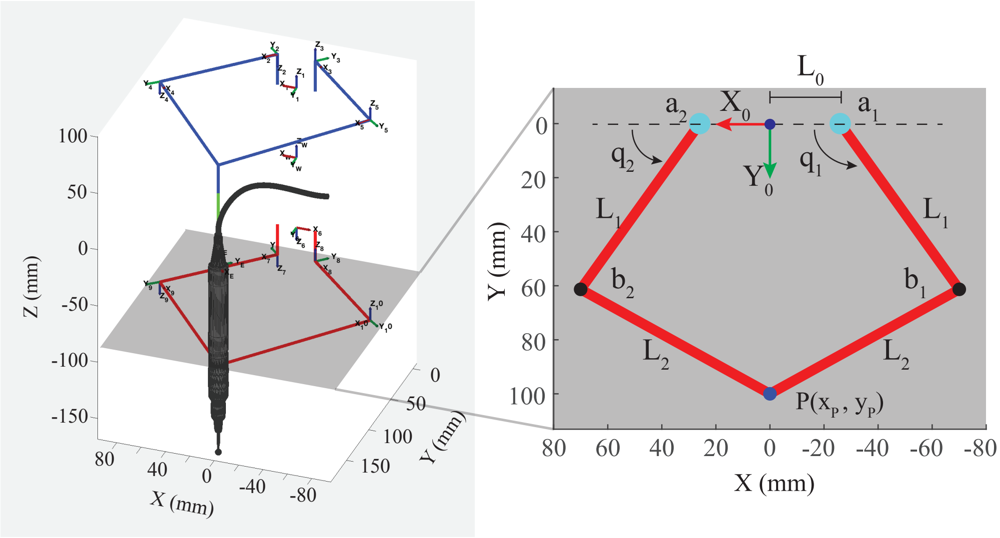

Figure 4.5: Looking at the CKU of CoSD (e.i. five-bar linkage mechanism), the relevant labels for the base frame coordinate system, joint positions, and joint lengths are shown. These are referenced within the forward kinematics calculations.

$$f = 1 + d^2$$

$$g = 2(cd - cL_1\cos q_1 + cL_0 - L_1\sin q_1)$$

$$h = d^2 - 2d(L_1\cos q_1 - L_0) - 2L_1L_0\cos q_1 + L_0^2 + L_1^2 - L_2^2$$

then, y_P can be obtained from (4.8) as:

$$y_P = \frac{-g \pm \sqrt{g^2 - 4fh}}{2f} \tag{4.9}$$

4.3.2 Initialization of Base Joints

In order to have an accurate end-effector position, the base joints must be initialized. This procedure involved both calibrating the potentiometers used to gather the base joint angles as well as zeroing the potentiometer readings at a known location. Only having to be performed once, the potentiometer calibration routine involved measuring each base joint

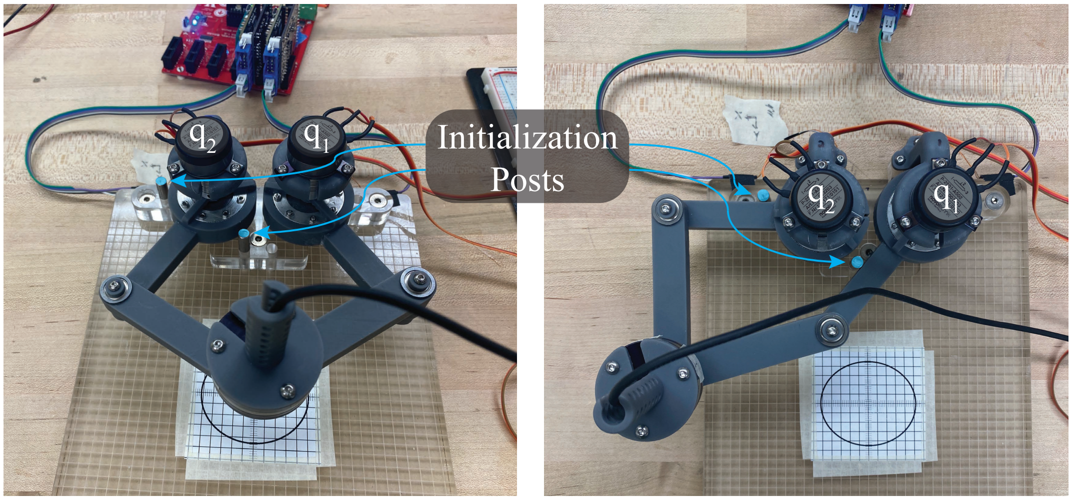

(a) (b)

Figure 4.6: This shows the CKU (a) at its centered position and (b) at the initialization position. In the initialization position, the first two links of the mechanism are placed so that they rest against initialization posts. These initialization posts are aligned to the CKU base coordinate frame, such that when the links touch the posts, q_1 and q_2 are at 50° and 0°, respectively.

angle, q_1 and q_2 (Figure 4.5), through approximately 130° of rotation using a coordinate measurement machine (CMM) (FARO GagePlus, FARO Technologies, Inc., Lake Mary, FL, USA), which has an accuracy of 0.025 mm within its working volume. Then these angles measured by the CMM were compared to the angle readings from the potentiometers at the same locations. Using the CMM measurements as the ground truth, a calibration ratio that mapped the potentiometer readings to the actual joint angles was found (0.963 and 0.959 for q_1 and q_2, respectively).

The calibrated potentiometer readings then needed to be zeroed at a known angle that was aligned with the five-bar linkage mechanism base coordinate frame. To do this, initialization posts, which are steel posts embedded into the base upon which the CKU is held, were used as stops for the first two linkages to be butted-up against (Figure 4.6 B.). At these locations, q_1 and q_2 are at 50° and 0° within the five-bar mechanism coordinate frame, respectively. When the links were placed at this initialization location, a momentary push button was pressed, which set the potentiometer readings to correspond to the initialization angles. With the initialization procedure completed, the initialization posts were removed so that they do not limit the workspace at all and the potentiometer readings were used with the forward kinematics to calculate the end-effector position.

4.4 Experiments

Experimentation was performed to test both the accuracy of the robotic system and the feasibility of this system in performing a mastoidectomy. While only performed for a planar case, it was important to ensure that a target boundary the size of a mastoidectomy opening could be enforced such that the drill could not drill outside the targeted bone region.

4.4.1 Workspace Analysis

To ensure that the CKU workspace is large enough to reach all points required for a mastoidectomy, a workspace analysis was performed. Prior work by Dillon et al. found that the workspace necessary for a mastoidectomy is approximately an inverted elliptical cone with major and minor ellipse diameters 52 mm and 45 mm, respectively, and a depth of 41 mm. For the planar case of a five-bar mechanism, the depth was ignored and the ellipse was defined as the required mastoidectomy workspace. Leveraging a workspace analysis performed by Liu et al. [102] on the optimum design parameters for a planar 5R symmetrical parallel mechanism, we decided on link lengths that would give a large singular-free area, deemed the usable workspace. Liu et al. present an atlas of usable workspace shapes based on the normalized relationship between link lengths. From this atlas, normalized link lengths for this design were chosen from the region with one of the largest usable workspaces. Actual link lengths were then calculated to ensure twice the minor ellipse diameter for total travel in the y-direction (see Section 4.5 for more details on this). The link lengths used in this design were 75.5 mm, 80 mm, and 26 mm for L_1, L_2, and L_0, respectively.

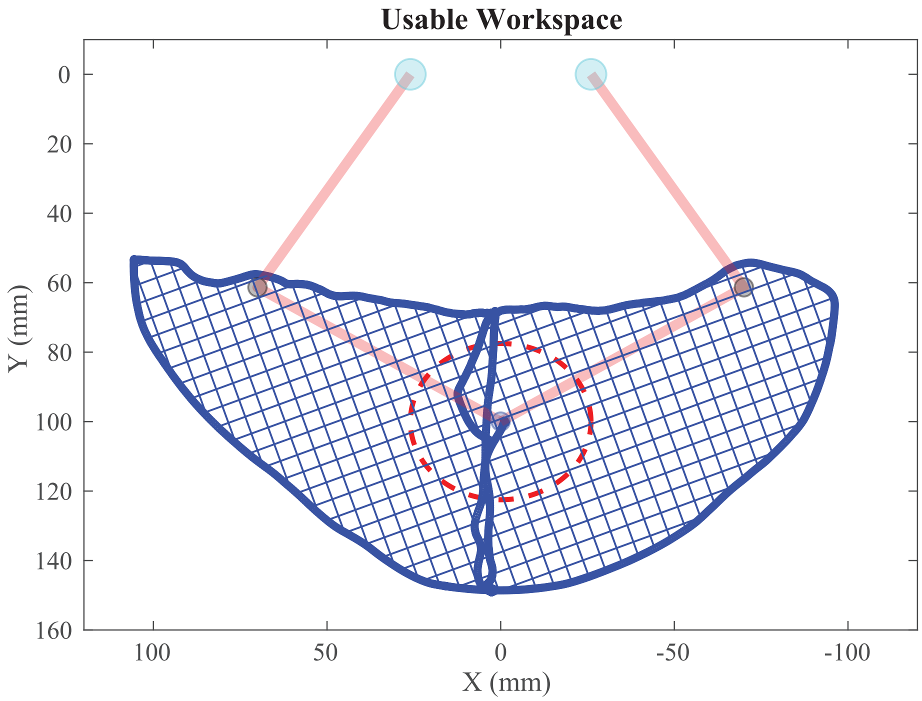

Figure 4.7: This shows the usable workspace of the CKU. The hatched area within the blue boundary is the actual usable workspace, gathered from moving the end-effector around and logging its position. The end-effector was moved such that it came conservatively close to the mechanism's singularities but never crossed them. Thus the mechanism workspace is a singular-free zone, and the mastoidectomy workspace within is shown by the dotted red ellipse.

Figure 4.7 shows the usable workspace of the CKU, gathered from actual end-effector position data as it moved around the workspace. We call it the usable workspace since this is the largest singular-free zone within the total mechanism workspace. To trace it, the end-effector was moved conservatively close to its singularities but steered clear of them. As a result, this usable workspace more than encapsulates the necessary area for performing a mastoidectomy, the boundaries of which are indicated by the dashed red ellipse.

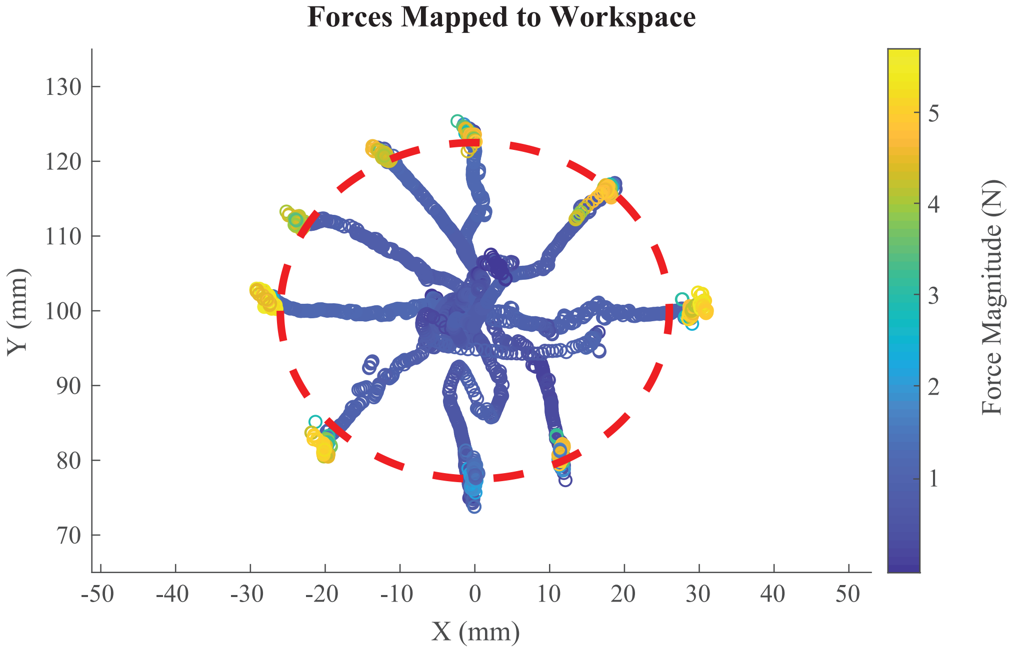

Figure 4.8: Force data is captured and mapped to the workspace as the end-effector is moved to and from the center of the ellipse to the elliptic boundary. Forces felt at the end-effector increase at the boundary when the MR brakes engage to prevent the end-effector from crossing the boundary. Note that smaller forces are seen at the lowest boundary (6 o'clock position) since this boundary is close to a kinematic singularity of the mechanism's workspace.

4.4.2 Enforcing a Boundary and Mapping Forces to the Workspace

A force sensor (Mini40, ATI Industrial Automation, Apex, NC, USA) was attached to the end effector to record forces throughout the workspace and show the effect that MR brake activation has on the end-effector. While force sensor data at the end-effector can be used for control to inform the system of user intent, here it is simply used for diagnostic data collection within the workspace. The system was set up such that the end-effector could move freely within the ellipse workspace, the boundary of which is shown by the dashed red line in Figure 4.8. When the end-effector hits the boundary line, both MR brakes at the base joints are engaged by sending 0.5 A of current to each coil, which generates ∼460 N·mm of torque in each brake (refer to Section 3.4 for a braking torque analysis of the MR brakes used).

To test the ability of the MR brakes to stop the motion of the end-effector, the end-effector was moved from the center of the ellipse to multiple radial points outside the ellipse. As the end-effector hit the boundary and the brakes engaged, the user continued to push in the radial direction attempting to move the end-effector outside the boundary. As a result of the MR brakes engaging, forces exerted on the end-effector increased since the end-effector was held stationary by the brakes. Figure 4.8 shows these increased forces at the boundary as they increase up to just under a Newton. Once engaged, the MR brakes were set to stay on for 4 seconds before disengaging. Therefore, if the user did not stop pushing after the 4 seconds, the end-effector would release and be allowed to push through the boundary freely and then moved back to the center of the ellipse workspace. Position data points from when the brakes disengage until it returns to within the workspace have been removed from Figure 4.8 so that the spurious movement of the end-effector releasing and crossing outside the boundary does not detract from the force mapping shown. Immediately after disengaging, a reverse current of 0.5 A was sent through the coil in both MR brakes for a brief amount of time (30 ms) to eliminate residual magnetic flux within the ferromagnetic housing of the brake, which leads to off-state torque. This reverse current burst allowed the brake to move more freely than simply returning the current to 0 A.

4.4.3 Haptic Feel of the CKU

For the CKU to be used effectively for drilling a mastoidectomy, the mechanism must not hinder the normal movement of the surgical drill. When encountering a boundary or feature that should not be drilled, the CKU must stop the motion of the drill to avoid going past the boundary or drilling the feature. When using a strictly passive system, the system can easily stop motion, but often, there is a ”sticky” feeling when trying to move back away from the boundary. This stickiness on the boundary is an undesired haptic feel that results in a jerking motion when detaching from the boundary. While this is a common problem

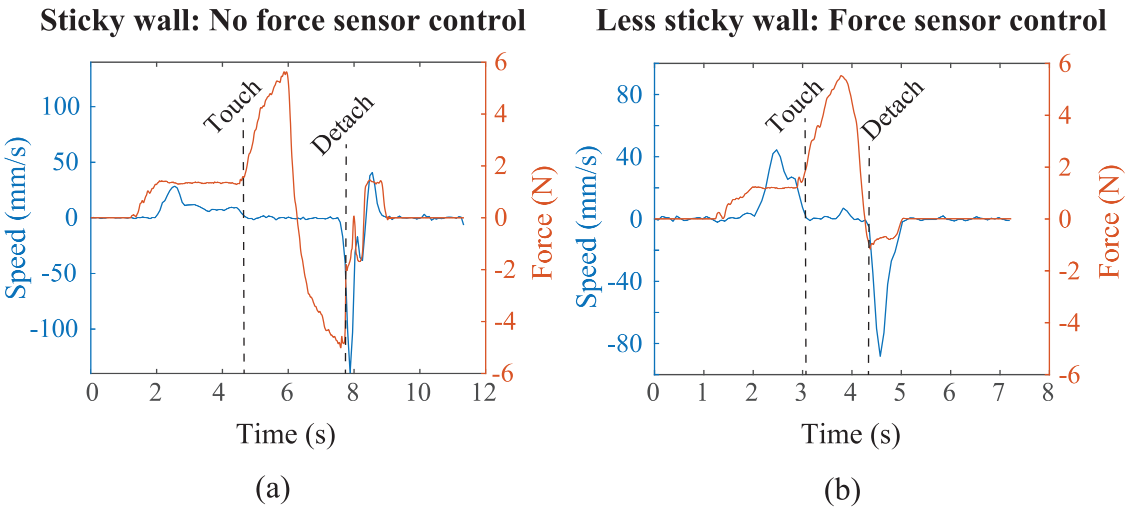

(a)

(b)

Figure 4.9: This shows how the use of a force sensor within the control loop can reduce the sticky feeling of detaching from a boundary wall. Both plots show the speed and force applied to the drill on the left and right y-axes, respectively. In each case, the drill was moved in the positive x-direction, was touched to the boundary with increasing force (MR brakes engaged), and then was moved in the negative x-direction until the MR brakes disengaged and allowed movement back into the workspace. Comparing (a), where the force sensor was not used in the control loop, and (b), where the force sensor was used in the control loop, the force required to move the drill off of the boundary and back into the workspace is reduced, resulting in a less sticky wall and a smooth transition back into the workspace.

in passive haptic systems [95], a solution is to add force sensing into the control loop to determine user motion intent. Without a force sensor in the control loop, to detach from the boundary, the CKU must rely on encoder readings and the forward kinematics to determine when the end effector is moving back into the workspace. Thus, with the brakes engaged after touching a boundary, this can only be done by using a large force in the opposite direction and detecting a small movement back into the workspace. The result is a sticky wall feeling and a jerky, fast motion of the drill back into the workspace. Alternatively, by adding a force sensor into the control loop, the CKU can disengage the brakes when a specified force in the direction back into the workspace is sensed. The result is a much less sticky wall, improved haptic feel, and a smooth transition back into the workspace off of the boundary.

An experiment to quantify and compare the haptic feel of the CKU with and without a force sensor in the loop was performed, and the results are shown in Figure 4.9. In both cases, the drill was moved in the positive x-direction until it touched the ellipse workspace boundary. When detected that it reached the boundary, the MR brakes engaged while the drill was continuously pushed and held into the boundary wall. After a second, the drill was moved in the negative x-direction back into the workspace until it reached the starting location. Both the position and forces on the drill were recorded, and the speed could be determined from the position and time data. The boundary touch and boundary detach events within the data were labeled.

Comparing the boundary wall touch event for with and without force sensor control, in both cases, the force of the drill pushed into the wall was just over 5 N, and the nearly vertical drop in speed to zero indicated a successful braking event at the boundary. Without the force sensor control, a large force pulling away from the wall of approximately 5 N resulted in a sticky wall. This behavior is not good for a smooth haptic feel of the device and could be potentially dangerous since a jerky detachment means a quick movement of the drill back into the workspace. Such a jerky movement leaves the user with little control over the movement of the drill and has the potential to drill a part of the workspace that was unintended. With the force sensor control, a detachment force of 0.5 N was set so that if the user moved the drill with 0.5 N back in the direction of the workspace, the brakes would disengage. This resulted in a smaller detachment force and a smoother transition off of the boundary. The detachment force was no more than the force felt on the drill when moving the drill freely around the workspace. Thus, with the force sensor added into the control loop to determine user intent, the haptic feel of the device was improved and the CKU motion was much smoother at the boundary.

4.4.4 Phantom Bone-Milling Experiment

To test the mechanism feasibility in performing a mastoidectomy, a surgical drill (Midas Rex, Medtronic, Minneapolis, MN, USA) was attached to the end-effector and used to

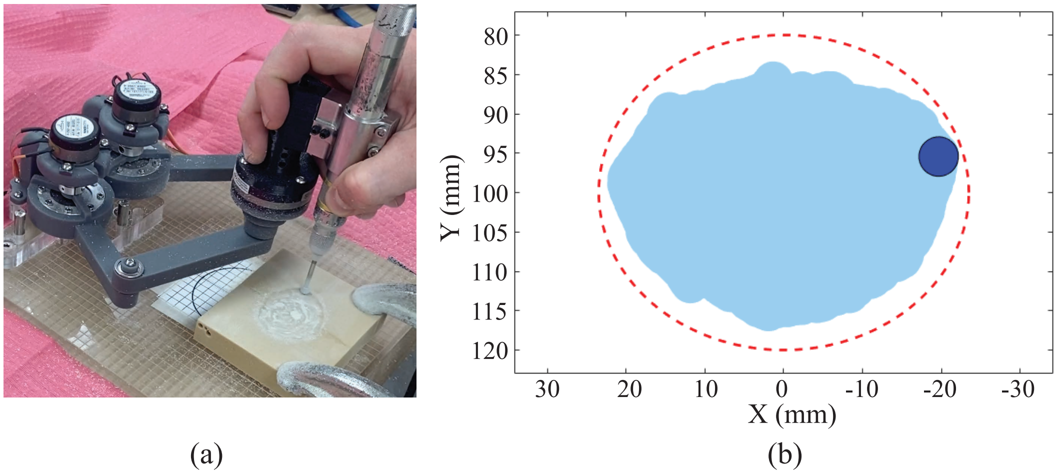

(a) (b)

Figure 4.10: The experimental setup for milling the elliptic opening of a mastoidectomy is shown. (a) shows the physical system with both the force sensor and the surgical drill attached to the end-effector as it is drilling the elliptic shape out of the Sawbones material. (b) shows the corresponding drill bit location when it is stopped at the boundary, with the MR brakes not allowing it to cross over. The light blue is areas throughout the drilling that have already been drilled away.

drill the opening of a mastoidectomy (approximated as an ellipse) on synthetic bone-like material called Sawbones (Pacific Research Laboratories, Vashon Island, WA USA). Figure 4.10 shows the experimental setup and the corresponding bone that has been removed from within the elliptical boundary.

To test the efficacy of the CKU in improving drilling accuracy, an otolaryngology-head and neck surgery (O-HNS) resident physician performed a drilling task using the CKU first with the MR brakes turned off (disabled) and again with the MR brakes turned on (enabled). With the brakes turned off, the drilling was performed freehand as normal. Although the drill was held by the CKU mechanism and constrained to its workspace, the brakes were disengaged and would not stop the motion of the drill in any way. With the brakes turned on, the motion of the drill could be stopped and the CKU would prevent the user from drilling undesired areas. For this experiment, the resident was given a template (see 4.11 (a)), which showed the desired area to be drilled (an ellipse whose dimensions approximate the opening for a mastoidectomy) and 5 different visual markers. These markers were to be used as a spatial reference for drilling the desired elliptical area, similar to how an O-HNS surgeon uses anatomical landmarks to perform the drilling safely during a mastoidectomy. The visual markers were transcribed onto a blank sawbones block. Using the template as a guide, the resident first drilled the desired elliptical area with the brakes turned off. On an identical sawbones blank, the resident drilled the desired elliptical shape again, but

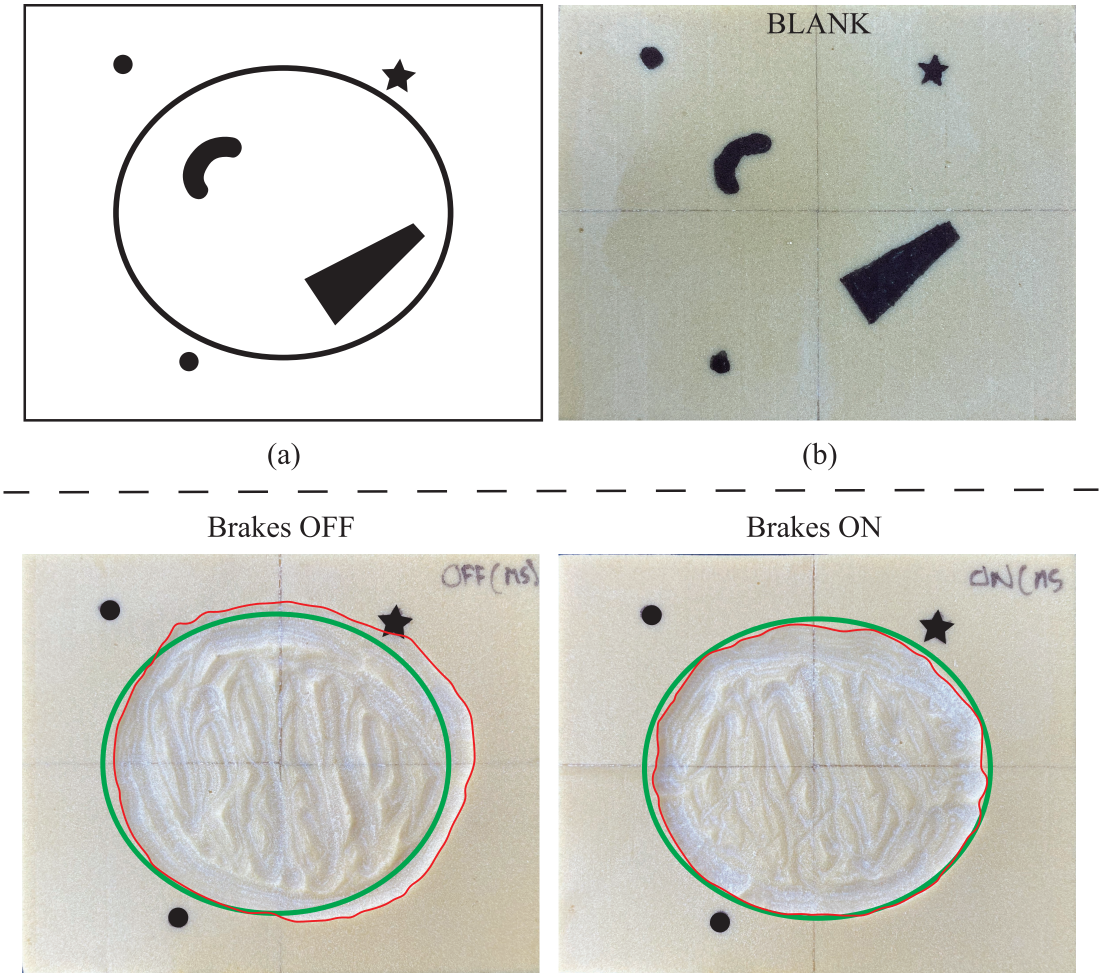

(a) (b)

(c)

Figure 4.11: For the drilling experiment, (a) a template with visual markers was used as a guide to drill out an ellipse (52 mm major diameter by 45 mm minor diameter). (b) The visual markers were transcribed on a sawbones blank, and an O-HNS resident physician was tasked with drilling out the elliptical shape as shown in (a). This was performed on two blanks, and the resident drilled one with the brakes turned off, and the second with the brakes turned on. The results of drilling with the CKU with the brakes turned off versus the brakes turned on are shown in (c).

	% Total Area Drilled	% Area Drilled Outside Boundary
Brakes OFF	97.2	13.4
Brakes ON	94.1	0.27

Table 4.1: Results for the drilling experiment using the CKU with the MR brakes disengaged (Brakes OFF) and engaged (Brakes ON).

this time with the brakes turned on so that they would prevent any drilling outside of the desired area. The two drilled areas were then compared to the desired elliptical shape to see if having the brakes stop the motion of the drill at the ellipse boundary would improve drilling accuracy. The results are shown in Table 4.1.

In Figure 4.11 (c), we see that while slightly more of the ellipse area was drilled when the brakes were turned off, a significant area was drilled outside the desired ellipse boundary. Conversely, when the brakes were turned on so that they stopped the motion of the drill when it got to the ellipse boundary, the percent of the area drilled outside the boundary was reduced. The only material drilled outside the desired area was in the bottom right quadrant, and at its largest distance from the ellipse boundary, it was $\sim$ 0.5 mm. Thus, the CKU improved the accuracy of the drilling by preventing areas outside of the ellipse to be drilled.

4.5 Results and Discussion

Results from the workspace analysis are shown in Figure 4.7. For the CKU, movement is more limited in the y-direction than the x-direction (refer to the base frame coordinate system shown in Figure 4.5). The total travel in the y-direction from the top of the workspace arc to the bottom of the workspace arc was designed to be twice the minor ellipse diameter of the mastoidectomy workspace (90 mm). After tracing the usable workspace and recording the actual end-effector position, the total travel in the y-direction was 81 mm. This was just under twice the minor ellipse diameter of the mastoidectomy workspace, and the slight undershoot can be attributed to the conservative tracing of the usable workspace. To avoid going through a singularity when tracing the workspace, the end-effector was kept a conservative distance from the singularity boundary. Had the end-effector been moved right up to the singular boundary, the total travel in the y-direction would be closer to 90 mm. Thus, based on the link lengths chosen for the five-bar mechanism ($L_1 = 75.5mm$, $L_2 = 80mm$, and $L_0 = 26mm$), the usable workspace successfully encompasses the mastoidectomy workspace for milling. When used within the CoSD design, the larger usable workspace of the CKU allows for the entire mastoid region to be reached, even in the case of slight misalignment when attaching CoSD to the patient.

Results of enforcing a boundary at the mastoidectomy workspace boundary are shown in Figure 4.8. It can be seen that when the brakes were not engaged and the end-effector moved freely within the elliptic boundary, forces were low (< 1 N). Upon hitting the boundary, forces on the end-effector increase to ~ 5 N. While the brakes were engaged, forces recorded at the end-effector were determined by how hard the user continued to push. Excessive force was not used, so forces stayed relatively low. The forces applied were kept reasonable to simulate how much force would be applied to the drill during actual milling. Although, without a surgeon using this device, proper forces applied to the surgical drill were just estimates. Some end-effector position data can be seen outside the boundary. This positioning error is likely the combination of a few factors. The first is that the kinematic link lengths were not calibrated. Second, even though the potentiometers were initialized using an accurate coordinate measurement machine (CMM), analog signal noise from the potentiometers causes some position errors. The position was determined directly from the forward kinematics, so noise in the potentiometer readings results in errors in the end-effector position. Finally, the control loop rate was approximately 60 Hz. If the end-effector was moved too quickly towards the boundary, the controller was not fast enough to stop it right on the boundary. The control rate could be potentially increased with further analysis of the code running on the robotics operating system (ROS).

Results from the phantom bone-milling experiment are shown in Figure 4.11 and in

Table 4.1. In Figure 4.11 (c), when the brakes were turned off for the full drilling and the ellipse shape was drilled freehand, a portion of the block outside the desired elliptical drilling space was drilled away (13.4% of the ellipse area). When the brakes were turned on and allowed to engage to prevent motion outside the boundary, only 0.27% of the ellipse area was drilled outside of the desired elliptical drilling space. The largest distance the drill went outside of the ellipse area was $\sim$ 0.5 mm, and this small error can be attributed to compliance within the links of the CKU. With the brakes on, the CKU improved the accuracy of the drilling. This accuracy increase in this 2-dimensional experiment shows the advantage of using this device to drill versus drilling freehand. Having shown the feasibility of the CKU for milling within a boundary, the next steps towards building the full CoSD can be taken. Future work in implementing the CoSD system for mastoidectomy must consider the extra surgical workflow steps that such a system would add. These are discussed below.

4.5.1 Surgical Workflow

To set up this system, a few additional steps must be added into the surgical workflow and are outlined in Figure 4.12. Vital anatomical structures, including the facial nerve, chorda tympani, external auditory canal, semicircular canals, and ossicles are automatically segmented from the preoperative CT scans using previously described methods [45, 46]. The volume of bone to be drilled out is then manually segmented by the surgeon (note: this part is not necessary to perform the surgery since this is a cooperative approach and surgeons would just make their own boundaries during the procedure. In the case that the surgeon wished to remove minimal bone, preplanned boundaries can be created and the robot will stop the drill from milling more than intended). Up to this point, all the steps have been preoperative and have not added additional time to the case.

During the actual surgery, a prepositioning frame (PPF) is attached to the patient's skull using three bone screws superior to the surgical site. An intraoperative CT scan is then

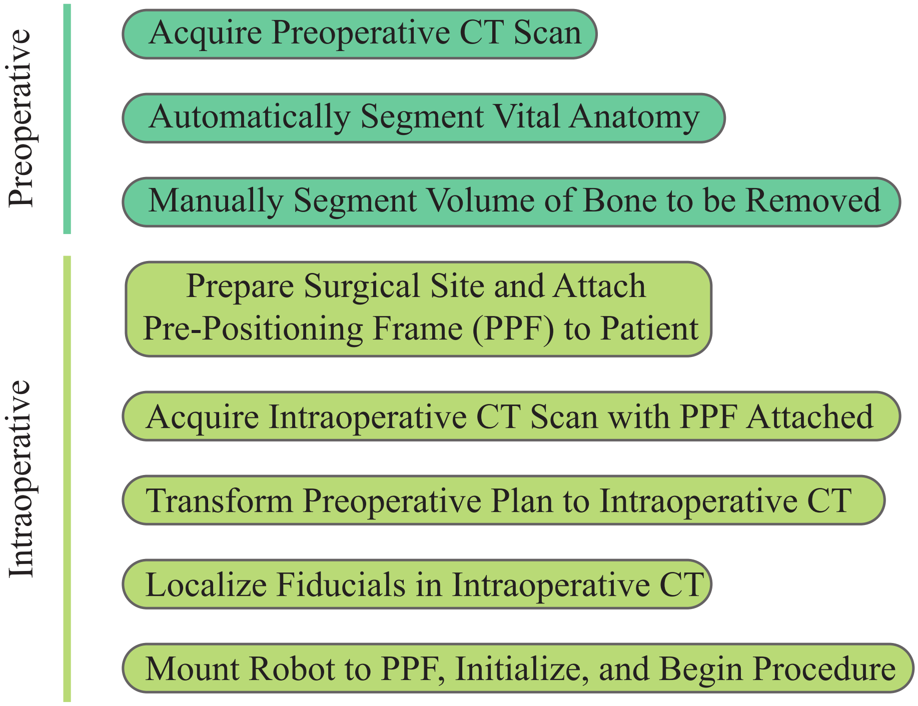

Figure 4.12: Surgical workflow of the preoperative and intraoperative steps for using CoSD. All segmentation and drill boundary planning is done preoperatively, and then the preoperative plan is registered to interoperative CT scan once the positioning frame is attached. Since the fiducials of the intraoperative CT scan are also the mounting locations for CoSD, the robot will know the locations of the anatomy once the fiducials are localized.

acquired and is registered to the preoperative CT scan using intensity-based registration based on mutual anatomical information [47]. Fiducials, which serve to both register the robot to the preoperative CT scan and attach the robot onto the patient, are localized within the intraoperative CT scan. Then, upon mounting the robot to the fiducials and initializing the encoders, the surgeon can cooperatively perform the mastoidectomy.

4.6 Conclusion

A design for a cooperatively-controlled, passive robot for mastoidectomy is presented. Testing on the CKU of the design shows the ability of the device to successfully keep a surgical drill within a predefined boundary. The device could be made to stop the drill from hitting vital anatomy during mastoidectomy, adding safety to the procedure. The inherent safety of the device, which is derived from being completely passive, lends a quicker path through regulatory compared to an automated approach. Additionally, its cooperative control, which keeps the surgeon in control of the drill motion, has a higher potential for adoption by surgeons than an automated approach. For these reasons, the cooperative approach has a quicker route to clinical translation.

Chapter 5

Conclusions and Future Work

This dissertation combines the expert drilling technique and adaptability of an otologic surgeon with the high accuracy and enhanced sensing capabilities of a robot to improve the safety and efficiency of mastoidectomy. By approaching the idea from both directions, namely starting with a CNC-like robot and giving it surgeon techniques and conversely starting with a surgeon and giving him/her greater precision and subsurface anatomical information, this dissertation converges towards a system of combined strengths. The automated approach is shown to be the best solution in the long run, but the cooperative, passive approach is the more immediate solution.

Chapter 2 focuses on making an automated milling robot, ANSR, mill more like a human surgeon and less like an industrial CNC machine. An algorithm is presented which takes in patient-specific CT scan data to both reduce forces towards vital anatomical structures and improve drilling efficiency. Image-based bone density estimates are used to speed up milling in less dense bone (i.e. air cells), and force-based modeling informed milling velocity and drill incidence angle to minimize forces towards vital structures. Experimentation in both surrogate bone and human temporal bone confirmed both reduction of peak milling forces and reduction of forces towards the facial nerve. In addition, a threshold force for breaking through the surgically skeletonized bone surrounding the facial nerve was experimentally quantified, and the new algorithm successfully lowers forces below this threshold for improved safety.

As with any new surgical device, adoption by the medical professionals using it is critical to the success of the device. For an automated robotic approach to mastoidectomy, such as with ANSR, this barrier to adoption is high since most of the control is taken out of the surgeon's hands. The surgeon must fully rely on and trust the system to complete the milling. Perhaps a cooperative robotic approach is better for quicker clinical adoption in otologic bone milling since the surgeon remains an active participant in the surgery as normal and the system only intervenes if the drill is in danger of hitting a vital anatomical structure. Thus, the cooperative approach is explored as a more immediate solution.

Chapters 3 and 4 described the design of an inherently safe, cooperative robotic system, CoSD, to give a surgeon greater precision and image-guidance, while also increasing safety for the patient. Designed as a bone-attached robot in order to increase system accuracy by eliminating additional tracking errors, the robot requires small, lightweight, and powerful brakes. No such commercial brake existed for this application, so a new design of a miniature magnetorheological (MR) brake with high braking torque was developed and characterized in Chapter 3.

In Chapter 4, the design for CoSD was presented. This is the first design of a bone-attached cooperative robot for mastoidectomy. Designed to be inherently safe with the use of MR brakes, this robot implements a control scheme that stops all drill motion if contact with bone outside the target region or with a vital anatomical structure is imminent. The core kinematic unit, a five-bar linkage mechanism, was built and experimentally used to test the boundary control. Additionally, smooth operation of the device is important to the success of this device, and a control scheme using a force sensor attached to the surgical drill reduces the sticky haptic feel when touching a boundary.

By approaching the problem from both directions, namely taking an automated approach and giving it human surgeon technique for more efficient milling and taking a surgeon and giving him/her robotic precision through an inherently safe cooperative device, a clinically viable solution to surgeon-robot milling in otologic surgery may be realized. Through this work, it was found that the automated approach described in Chapter 2 provides the most benefits in the long run, but it faces a high barrier to clinical adoption. The cooperative approach described in Chapter 4 does not provide the same repeatability as an automated approach, but given its completely passive design, it has the potential for quicker clinical adoption.

5.1 Future Work in Robotic Mastoidectomy

Future work on both mastoidectomy robots presented in this work should focus on further testing on each device, particularly with regards to integration into the current clinical workflow. For either system to be clinically viable, it must show true value to both the hospital and patient outcomes. Reducing operative time, especially in long cases such as the translabyrinthine acoustic neuroma surgery, is a great benefit to both patient health and hospital cost. Therefore, better quantifying such time savings would illustrate the value of implementing either system. Quantification of time savings would involve not only the time it takes for the milling itself but also the additional time to set up, sterilize, attach, initialize, etc., that is inherent to a robotic approach compared to traditional manual milling. Optimization of these additional workflow steps for a robotic approach would be necessary to reduce operative time. For ANSR, institutional review board approval was received to test all the steps of the system except for the milling on patients. This will provide great insight into the time required to perform those setup steps mentioned and into any practical challenges associated with that setup.

Given the higher barrier to clinical adoption of an automated approach like ANSR, future work could focus on giving the surgeon more feedback during an automated mastoidectomy procedure. While it is true that an automated system would eliminate much of the feedback the surgeon has during bone milling, adding additional visual feedback, such as a camera video feed of the drilling along with real-time image-guidance video feed of the drill tip in relation to vital anatomical structures, would keep the surgeon “in the loop” and allow for the surgeon to better interact with the system.

The next consideration for the clinical realization of both systems is sterilization. Ideally, the whole robot would be sterilizable. As it stands for ANSR, the motors and sensors used are not able to be autoclaved and therefore would need to be substituted with sterilizable versions. For CoSD, the MR brakes were not designed to be sterilizable, but since the current-carrying coils are sealed within the rotor, substituting the magnet wire used for wire with insulation that can handle the high autoclave temperatures should be the only change needed for sterilization. If the substitution of non-sterilizable components is not possible, then alternative means of separating the robot from the patient can be used. The structure of the robot could be bagged with the drill mounted through the bag in the operating room after it is sterilized.

Lastly, and most importantly, all future work for these systems should look to improve patient outcomes. While work has been done to show the *potential* improvement these systems can have on otologic surgery (i.e. removal of less bone, reduction in damage to vital anatomical structures, decrease in operative time, etc.), its real clinical value is unknown. More work must be done to quantify and assess these potential benefits through more experimentation and comparison to clinical data for mastoidectomy. Only then could it be determined if the clinical translation of these systems would ultimately lead to improved patient outcomes.

5.2 Future Work in Miniature Magnetorheological Brakes

The magnetorheological (MR) brake design that was developed for the cooperative mastoidectomy device has the potential to be used in various other applications, where a small, lightweight, yet powerful and controllable brake would be advantageous. These may include other bone-attached surgical devices where precise positioning is necessary. One such application may be an image-guided alignment device for deep brain stimulation. In deep brain stimulation, a precise, direct path for implanting a neurostimulator within the brain is needed. To assist with alignment, three miniature MR brakes, controlling the roll, pitch, and yaw, could be used one at a time to properly orient a preplanned trajectory when coupled with image-guidance. An additional advantage of this brake design could be for robotic applications where the brake is mounted on a moving link, and it is desirable to have low inertia to improve the dynamic performance of the arm. Wearable haptics is another field where the advantages of this brake design have potential.

A known drawback of MR brakes is their inherent magnetic hysteretic behavior. This affects the controllability of the brake since it leads to significant residual off-state torque, but there are solutions to counteract the hysteresis, including hysteretic modeling, using a force/torque sensor, or embedding a hall effect sensor for use in closed-loop control [58]. While it may not be necessary to precisely control the MR brake for certain applications (i.e. for CoSD, as long as the braking torque is increased enough to overcome surgeon force on the drill then it can be used to stop the motion effectively), there are certainly benefits to finely controlling braking torque. Therefore, the next iteration of this brake should take into account a way to effectively eliminate the hysteretic behavior.

5.3 Future Work in Patient-Specific Planning

The algorithm developed for patient-specific trajectory planning of the acoustic neuroma surgical robot (ANSR) is one that is generalized so that it can be applied to other automated milling robots. To quantify the improvement of this algorithm at reducing forces both towards the facial nerve and in magnitude overall, a simplified "lawnmower" path was used. This type of path, while it allowed for a fair comparison for the study, would not be the fastest nor the most efficient path to choose for an actual procedure. Due to the irregular shape of the pocket of bone to drill out as well as the potential for small nooks, a more intelligent path planner is needed for this procedure. Future work towards implementing this algorithm along with a more intelligent path planner, such as the one presented by Dillon et al. [30], would allow for the forces towards vital anatomy to be reduced and for cutting to be as efficient as possible. After implementing these, it would be beneficial to see the improvements in the speed of the procedure, since both minimizing operative time and increasing safety and efficiency through a reduction in forces move this system closer to clinical translation.

5.4 Conclusion

In conclusion, the main focus of this work is to combine the best aspects of surgeons and robots in a system for improving mastoidectomy. By approaching the problem from both directions, that is, making a robot mill like a surgeon and conversely giving a surgeon robotic precision, this work aimed to find a near-optimal solution for human-robot collaboration in otologic milling procedures. It was found that the automated approach provides more benefits for the patient in the long run (e.g. lower forces towards vital anatomy, higher repeatability, potential surgical time savings) and given the work from Chapter 2, can adapt like a surgeon to a specific patient based on their anatomy, but ultimately it has a high barrier to clinical adoption and requires more testing to ensure safe operation. Alternatively, the cooperative approach does not have the same repeatability as the automated approach, but accuracy improvement over freehand drilling shown in Chapter 4 as well as its passive design lends quicker clinical adoption. While the systems described in this work are still in the laboratory setting, the hope is that they are closer to clinical translation with the contributions laid out in this dissertation. Ultimately, the goal of medical technology research, and more specifically surgical robotics, is to improve clinical outcomes for patients, and the two systems presented have the potential to achieve this goal through reduced invasiveness, decreased procedure time, and decreased risk of complications.

BIBLIOGRAPHY

[1] Philipp A Federspil, Urban W Geisthoff, Dominik Henrich, and Peter K Plinkert. Development of the first force-controlled robot for otoneurosurgery. *The Laryngoscope*, 113(3):465–71, March 2003.

[2] Andrei Danilchenko, Ramya Balachandran, Jenna L. Toennis, Stephan Baron, Benjamin Munkse, J. Michael Fitzpatrick, Thomas J. Withrow, Robert J. Webster III, and Robert F. Labadie. Robotic Mastoidectomy. *Otology & Neurotology*, (32):11–16, 2010.

[3] Hoon Lim, Nozomu Matsumoto, Byunghyun Cho, Jaesung Hong, Makoto Yamashita, Makoto Hashizume, and Byung-Ju Yi. Semi-manual mastoidectomy assisted by human–robot collaborative control–a temporal bone replica study. *Auris Nasus Larynx*, 43(2):161–165, 2016.

[4] Neal P Dillon, Ramya Balachandran, Michael A Siebold, Robert J Webster III, George B Wanna, and Robert F Labadie. Cadaveric testing of robot-assisted access to the internal auditory canal for vestibular schwannoma removal. *Otology & Neurotology*, 38(3):441, 2017.

[5] Lesley C French, Mary S Dietrich, and Robert F Labadie. An estimate of the number of mastoidectomy procedures performed annually in the united states. *Ear, Nose & Throat Journal*, 87(5):267, 2008.

[6] D Gareth R Evans, Anthony Moran, Andrew King, S Saeed, Nihal Gurusinghe, and Richard Ramsden. Incidence of vestibular schwannoma and neurofibromatosis 2 in the north west of england over a 10-year period: higher incidence than previously thought. *Otology & Neurotology*, 26(1):93–97, 2005.

[7] Sven-Eric Stangerup, Mirko Tos, Jens Thomsen, and Per Caye-Thomasen. True incidence of vestibular schwannoma? *Neurosurgery*, 67(5):1335–1340, 2010.

[8] Derald Brackmann, Clough Shelton, and Moses A Arriaga. *Otologic Surgery*. Elsevier Health Sciences, 2015.

[9] Jérémy Lecoeur, Jack H Noble, Ramya Balachandran, Robert F Labadie, and Benoit M Dawant. Variability of the temporal bone surface's topography: implications for otologic surgery. In *Medical Imaging 2012: Image-Guided Procedures, Robotic Interventions, and Modeling*, volume 8316, page 83161B. International Society for Optics and Photonics, 2012.

[10] Steven Arild Wuyts Andersen, Peter Trier Mikkelsen, Lars Konge, Per Cayé-Thomasen, and Mads Sølvsten Sørensen. Cognitive load in distributed and massed practice in virtual reality mastoidectomy simulation. *The Laryngoscope*, 126(2):E74–E79, 2016.

[11] Russell H Taylor, Arianna Menciassi, Gabor Fichtinger, Paolo Fiorini, and Paolo Dario. Medical robotics and computer-integrated surgery. In *Springer handbook of robotics*, pages 1657–1684. Springer, 2016.

[12] SC Ho, RD Hibberd, and BL Davies. Robot assisted knee surgery. *Engineering in Medicine and Biology Magazine, IEEE*, 14(3):292–300, 1995.

[13] M Jakopec, SJ Harris, F Rodriguez y Baena, P Gomes, J Cobb, and BL Davies. The first clinical application of a hands-on robotic knee surgery system. *Computer Aided Surgery*, 6(6):329–339, 2001.

[14] Peter Kazanzides, Brent D Mittelstadt, Bela L Musits, William L Bargar, Joel F Zuhars, Bill Williamson, Phillip W Cain, and Emily J Carbone. An integrated system for cementless hip replacement. *Engineering in Medicine and Biology Magazine, IEEE*, 14(3):307–313, 1995.

[15] T Cill Kienzle, S David Stulberg, Michael Peshkin, Arthur Quaid, Jon Lea, A Goswani, and Chi-haur Wu. Total knee replacement. *Engineering in Medicine and Biology Magazine, IEEE*, 14(3):301–306, 1995.

[16] Howard A Paul, William L Bargar, Brent Mittlestadt, Bela Musits, Russell H Taylor, Peter Kazanzides, Joel Zuhars, Bill Williamson, and William Hanson. Development of a surgical robot for cementless total hip arthroplasty. *Clinical Orthopaedics and Related Research*, 285:57–66, 1992.

[17] Russell H Taylor, Brent D Mittelstadt, Howard A Paul, William Hanson, Peter Kazanzides, Joel F Zuhars, Bill Williamson, Bela L Musits, Edward Glassman, and William L Bargar. An image-directed robotic system for precise orthopaedic surgery. *Robotics and Automation, IEEE Transactions on*, 10(3):261–275, 1994.

[18] Moshe Shoham, Michael Burman, Eli Zehavi, Leo Joskowicz, Eduard Batkilin, and Yigal Kunicher. Bone-mounted miniature robot for surgical procedures: concept and clinical applications. *Robotics and Automation, IEEE Transactions on*, 19(5):893–901, 2003.

[19] Yik San Kwoh, Joahin Hou, Edmond A Jonckheere, and Samad Hayati. A robot with improved absolute positioning accuracy for ct guided stereotactic brain surgery. *Biomedical Engineering, IEEE Transactions on*, 35(2):153–160, 1988.

[20] J Cobb, J Henckel, P Gomes, S Harris, M Jakopec, F Rodriguez, A Barrett, and B Davies. Hands-on robotic unicompartmental knee replacement: a prospective, randomised controlled study of the acrobot system. *The Journal of bone and joint surgery. British volume*, 88(2):188–197, 2006.

[21] Hoon Lim, Jung-Min Han, Jaesung Hong, Byung-Ju Yi, Seung Hwan Lee, Jin Hyeok Jeong, Nozomu Matsumoto, Masamichi Oka, Shizuo Komune, and

Makoto Hashizume. Image-guided robotic mastoidectomy using human-robot collaboration control. In *2011 International Conference on Mechatronics and Automation*, pages 549–554. IEEE, 2011.

[22] Kevin C Olds, Preetham Chalasani, Paulette Pacheco-Lopez, Iulian Iordachita, Lee M Akst, and Russell H Taylor. Preliminary evaluation of a new microsurgical robotic system for head and neck surgery. In *2014 IEEE/RSJ International Conference on Intelligent Robots and Systems*, pages 1276–1281. IEEE, 2014.

[23] Myung Hoon Yoo, Hwan Seo Lee, Chan Joo Yang, Seung Hwan Lee, Hoon Lim, Seongpung Lee, Byung-Ju Yi, and Jong Woo Chung. A cadaver study of mastoidectomy using an image-guided human–robot collaborative control system. *Laryngoscope investigative otolaryngology*, 2(5):208–214, 2017.

[24] Jong-Ha Chung, Seong-Young Ko, Dong-Soo Kwon, Jung-Ju Lee, Yong-San Yoon, and Choong-Hee Won. Robot-assisted femoral stem implantation using an intramedulla gauge. *Robotics and Automation, IEEE Transactions on*, 19(5):885–892, 2003.

[25] C Plaskos, P Cinquin, S Lavallée, and AJ Hodgson. Praxiteles: a miniature bone-mounted robot for minimal access total knee arthroplasty. *The International Journal of Medical Robotics and Computer Assisted Surgery*, 1(4):67–79, 2005.

[26] A Wolf, B Jaramaz, B Lisien, and AM DiGioia. Mbars: mini bone-attached robotic system for joint arthroplasty. *The International Journal of Medical Robotics and Computer Assisted Surgery*, 1(2):101–121, 2005.

[27] Dennis P Devito, Leon Kaplan, Rupert Dietl, Michael Pfeiffer, Dale Horne, Boris Silberstein, Mitchell Hardenbrook, George Kiriyanthan, Yair Barzilay, Alexander Bruskin, et al. Clinical acceptance and accuracy assessment of spinal implants

guided with spineassist surgical robot: retrospective study. *Spine*, 35(24):2109–2115, 2010.

[28] Jan-Philipp Kobler, Kathrin Nuelle, G Jakob Lexow, Thomas S Rau, Omid Majdani, Lueder A Kahrs, Jens Kotlarski, and Tobias Ortmaier. Configuration optimization and experimental accuracy evaluation of a bone-attached, parallel robot for skull surgery. *International journal of computer assisted radiology and surgery*, 11(3):421–436, 2016.

[29] Louis B Kratchman, Grégoire S Blachon, Thomas J Withrow, Ramya Balachandran, Robert F Labadie, and Robert J Webster. Design of a bone-attached parallel robot for percutaneous cochlear implantation. *Biomedical Engineering, IEEE Transactions on*, 58(10):2904–10, 2011.

[30] Neal P Dillon, Ramya Balachandran, J Michael Fitzpatrick, Michael A Siebold, Robert F Labadie, George B Wanna, Thomas J Withrow, and Robert J Webster. A compact, bone-attached robot for mastoidectomy. *Journal of Medical Devices*, 9(3):031003–1–7, 2015.

[31] Naohiko Sugita, Taiga Nakano, Yoshikazu Nakajima, Kazuo Fujiwara, Nobuhiro Abe, Toshifumi Ozaki, Masahiko Suzuki, and Mamoru Mitsuishi. Dynamic controlled milling process for bone machining. *Journal of Materials Processing Technology*, 209(17):5777–5784, 2009.

[32] Tianmiao Wang, Sheng Luan, Lei Hu, Zhongjun Liu, Weishi Li, and Liang Jiang. Force-based control of a compact spinal milling robot. *The International Journal of Medical Robotics and Computer Assisted Surgery*, 6(2):178–185, 2010.

[33] Tom M Williamson, Brett J Bell, Nicolas Gerber, Lilibeth Salas, Philippe Zysset, Marco Caversaccio, and Stefan Weber. Estimation of tool pose based on force–

density correlation during robotic drilling. *Biomedical Engineering, IEEE Transactions on*, 60(4):969–976, 2013.

[34] Christopher C Heath, Ramya Balachandran, Omid Majdani, Andrew Jurik, Thomas Edwards, Robert F Labadie, and J Michael Fitzpatrick. Disablement of a surgical drill via ct guidance to protect vital anatomy. In *Medical Imaging 2009: Visualization, Image-Guided Procedures, and Modeling*, volume 7261, page 72610N. International Society for Optics and Photonics, 2009.

[35] Wen P Liu, Mahdi Azizian, Jonathan Sorger, Russell H Taylor, Brian K Reilly, Kevin Cleary, and Diego Preciado. Cadaveric feasibility study of da vinci si–assisted cochlear implant with augmented visual navigation for otologic surgery. *JAMA Otolaryngology–Head & Neck Surgery*, 140(3):208–214, 2014.

[36] Neal P Dillon, Loris Fichera, Patrick S Wellborn, Robert F Labadie, and Robert J Webster. Making robots mill bone more like human surgeons: using bone density and anatomic information to mill safely and efficiently. In *2016 IEEE/RSJ International Conference on Intelligent Robots and Systems (IROS)*, pages 1837–1843. IEEE, 2016.

[37] Neal P Dillon, Louis B Kratchman, Mary S Dietrich, Robert F Labadie, Robert J Webster III, and Thomas J Withrow. An experimental evaluation of the force requirements for robotic mastoidectomy. *Otology & Neurotology*, 2013.

[38] Mohammadreza Arbabtafti, Majid Moghaddam, Ali Nahvi, Mohammad Mahvash, Barry Richardson, and Bijan Shirinzadeh. Physics-based haptic simulation of bone machining. *Haptics, IEEE Transactions on*, 4(1):39–50, 2011.

[39] Nam-Gyu Ryu and Jin Kim. How to avoid facial nerve injury in mastoidectomy? *Journal of audiology & otology*, 20(2):68, 2016.

[40] Sandeep Dhanik and Paul Xirouchakis. Contour parallel milling tool path generation for arbitrary pocket shape using a fast marching method. *The International Journal of Advanced Manufacturing Technology*, 50(9-12):1101–1111, 2010.

[41] Eberhard Abele, Stefan Rothenbücher, and Matthias Weigold. Cartesian compliance model for industrial robots using virtual joints. *Production Engineering*, 2(3):339–343, 2008.

[42] Jan-Philipp Kobler, Lenka Prielozny, G.Jakob Lexow, Thomas S. Rau, Omid Majdani, and Tobias Ortmaier. Mechanical characterization of bone anchors used with a bone-attached, parallel robot for skull surgery. *Medical Engineering & Physics*, 37(5):460 – 468, 2015.

[43] Paul Butler, Adam WM Mitchell, and Harold Ellis. *Applied radiological anatomy*. Cambridge University Press, 1999.

[44] Luciana Munhoz, Christyan Hiroshi Iida, Reinaldo Abdala Junior, Ronaldo Abdala, and Emiko Saito Arita. Mastoid air cell system: Hounsfield density by multislice computed tomography. *Journal of Clinical & Diagnostic Research*, 12(4), 2018.

[45] Jack H Noble, Frank M Warren, Robert F Labadie, and Benoit M Dawant. Automatic segmentation of the facial nerve and chorda tympani in ct images using spatially dependent feature values. *Medical physics*, 35(12):5375–5384, 2008.

[46] Jack H Noble, Benoit M Dawant, Frank M Warren, and Robert F Labadie. Automatic identification and 3-d rendering of temporal bone anatomy. *Otology & neurotology: official publication of the American Otological Society, American Neurotology Society [and] European Academy of Otology and Neurotology*, 30(4):436, 2009.

[47] Frederik Maes, Andre Collignon, Dirk Vandermeulen, Guy Marchal, and Paul Suetens. Multimodality image registration by maximization of mutual information. *Medical Imaging, IEEE Transactions on*, 16(2):187–198, 1997.

[48] Michael Fitzpatrick and Milan Sonka. Handbook of medical imaging, volume 2: Medical image processing & analysis. *Bellingham, WA: SPIE Press*, 2000.

[49] V Cunha-Cruz, A Follmann, A Popovic, P Bast, T Wu, S Heger, M Engelhardt, K Schmieder, and K Radermacher. Robot-and computer-assisted craniotomy (cranio): from active systems to synergistic manmachine interaction. *Proceedings of the Institution of Mechanical Engineers, Part H: Journal of Engineering in Medicine*, 224(3):441–452, 2010.

[50] Robert F Labadie, Ramya Balachandran, Jack H Noble, Grégoire S Blachon, Jason E Mitchell, Fitsum A Reda, Benoit M Dawant, and J Michael Fitzpatrick. Minimally invasive image-guided cochlear implantation surgery: First report of clinical implementation. *The Laryngoscope*, 124(8):1915–1922, 2014.

[51] Arne Feldmann, Juan Anso, Brett Bell, Tom Williamson, Kate Gavaghan, Nicolas Gerber, Helene Rohrbach, Stefan Weber, and Philippe Zysset. Temperature prediction model for bone drilling based on density distribution and in vivo experiments for minimally invasive robotic cochlear implantation. *Annals of Biomedical Engineering*, 44(5):1576–1586, 2016.

[52] Gerd Hirzinger, Max Fischer, Bernhard Brunner, Ralf Koeppe, Martin Otter, Markus Grebenstein, and Ingo Schäfer. Advances in robotics: the dlr experience. *The International Journal of Robotics Research*, 18(11):1064–1087, 1999.

[53] Ulrich Hagn, Rainer Konietschke, Andreas Tobergte, Mathias Nickl, Stefan Jörg, Bernhard Kübler, Georg Passig, Martin Gröger, Florian Fröhlich, Ulrich Seibold, et al. Dlr mirosurge: a versatile system for research in endoscopic telesurgery. *International Journal of Computer Assisted Radiology and Surgery*, 5(2):183–193, 2010.

[54] Inrak Choi, Elliot W Hawkes, David L Christensen, Christopher J Ploch, and Sean Follmer. Wolverine: A wearable haptic interface for grasping in virtual reality. In

Intelligent Robots and Systems (IROS), 2016 IEEE/RSJ International Conference on, pages 986–993. IEEE, 2016.

[55] Siyao Hu and Katherine J Kuchenbecker. High magnitude unidirectional haptic force display using a motor/brake pair and a cable. In *World Haptics Conference (WHC), 2017 IEEE*, pages 394–399. IEEE, 2017.

[56] Patrick Dills, Chembian Parthiban, It Fufuengsin, and Michael Zinn. Design and analysis of a high performance impedance based hybrid haptic interface. In *IEEE Haptics Symposium*, 2018.

[57] Edward J Park, Dilian Stoikov, Luis Falcao da Luz, and Afzal Suleman. A performance evaluation of an automotive magnetorheological brake design with a sliding mode controller. *Mechatronics*, 16(7):405–416, 2006.

[58] Ozan Erol, Berk Gonenc, Doruk Senkal, Sait Alkan, and Hakan Gurocak. Magnetic induction control with embedded sensor for elimination of hysteresis in magnetorheological brakes. *Journal of Intelligent Material Systems and Structures*, 23(4):427–440, 2012.

[59] Ogura industrial corp. https://ogura-clutch.com/. [Online; accessed: 2018].

[60] Magtrol, inc. https://www.magtrol.com/. [Online; accessed: 2018].

[61] Michael Gogola and Michael Goldfarb. Design of a pzt-actuated proportional drum brake. *IEEE/ASME Transactions on Mechatronics*, 4(4):409–416, 1999.

[62] WH Li and H Du. Design and experimental evaluation of a magnetorheological brake. *The International Journal of Advanced Manufacturing Technology*, 21(7):508–515, 2003.

[63] B Liu, WH Li, Prabuono B Kosasih, and XZ Zhang. Development of an mr-brake-based haptic device. *Smart Materials and Structures*, 15(6):1960, 2006.

[64] Kerem Karakoc, Edward J Park, and Afzal Suleman. Design considerations for an automotive magnetorheological brake. *Mechatronics*, 18(8):434–447, 2008.

[65] B Assadsangabi, F Daneshmand, N Vahdati, M Eghtesad, and Y Bazargan-Lari. Optimization and design of disk-type mr brakes. *International Journal of Automotive Technology*, 12(6):921–932, 2011.

[66] A Poznić, A Zelić, and L Szabó. Magnetorheological fluid brake–basic performances testing with magnetic field efficiency improvement proposal. *Hungarian Journal of Industry and Chemistry*, 40(2):107–111, 2012.

[67] Carlos Rossa, Adrien Jaegy, José Lozada, and Alain Micaelli. Design considerations for magnetorheological brakes. *IEEE/ASME Transactions on Mechatronics*, 19(5):1669–1680, 2014.

[68] Placid industries. https://placidindustries.com/. [Online; accessed: 2018].

[69] Jinung An and Dong-Soo Kwon. Modeling of a magnetorheological actuator including magnetic hysteresis. *Journal of Intelligent Material Systems and Structures*, 14(9):541–550, 2003.

[70] Marion L Hodgdon. Applications of a theory of ferromagnetic hysteresis. *Magnetics, IEEE Transactions on*, 24(1):218–221, 1988.

[71] ID Mayergoyz. Dynamic preisach models of hysteresis. *Magnetics, IEEE Transactions on*, 24(6):2925–2927, 1988.

[72] Kun Wang, Ying Zhang, and Richard W Jones. Modelling of hysteresis in smart actuators using the generalised prandtl-ishlinskii operator. In *ICCAS 2010*, pages 261–266. IEEE, 2010.

[73] F Ossart, TA Phung, and G Meunier. Comparison between various hysteresis models and experimental data. *Journal of Applied Physics*, 67(9):5379–5381, 1990.

[74] Andrezej Demenko, Cezary Jedryczka, Piotr Sujka, and Wojciech Szelag. The influence of magnetic hysteresis on magnetorheological fluid clutch operation. *COMPEL-The international journal for computation and mathematics in electrical and electronic engineering*, 2009.

[75] A Wiehe, K Voth, and J Maas. Rotary mr actuators with current less holding torque for a vehicle door assistant. In *Journal of Physics: Conference Series*, volume 149, page 012085. IOP Publishing, 2009.

[76] Doruk Senkal and Hakan Gurocak. Serpentine flux path for high torque mrf brakes in haptics applications. *Mechatronics*, 20(3):377–383, 2010.

[77] Alireza Farjoud, Nader Vahdati, and Yap Fook Fah. Mathematical model of drum-type mr brakes using herschel-bulkley shear model. *Journal of Intelligent Material Systems and Structures*, 19(5):565–572, 2008.

[78] WH Li, B Liu, Prabuono B Kosasih, and XZ Zhang. A 2-dof mr actuator joystick for virtual reality applications. *Sensors and Actuators A: Physical*, 137(2):308–320, 2007.

[79] Jonathan Blake and Hakan B Gurocak. Haptic glove with mr brakes for virtual reality. *IEEE/ASME Transactions On Mechatronics*, 14(5):606–615, 2009.

[80] KH Gudmundsson, F Jonsdottir, and F Thorsteinsson. A geometrical optimization of a magneto-rheological rotary brake in a prosthetic knee. *Smart Materials and Structures*, 19(3):035023, 2010.

[81] Hongtao Guo and Wei-Hsin Liao. Optimization of a multifunctional actuator utilizing magnetorheological fluids. In *Advanced Intelligent Mechatronics (AIM), 2011 IEEE/ASME International Conference on*, pages 67–72.

[82] Hadi Shamieh and Ramin Sedaghati. Development, optimization, and control of a novel magnetorheological brake with no zero-field viscous torque for automotive applications. *Journal of Intelligent Material Systems and Structures*, 29(16):3199–3213, 2018.

[83] More Avraam, Mihaita Horodinca, Iulian Romanescu, and André Preumont. Computer controlled rotational mr-brake for wrist rehabilitation device. *Journal of intelligent material systems and structures*, 21(15):1543–1557, 2010.

[84] QH Nguyen and SB Choi. Selection of magnetorheological brake types via optimal design considering maximum torque and constrained volume. *Smart Materials and Structures*, 21(1):015012, 2011.

[85] Huanhuan Qin, Aiguo Song, Xin Zeng, and Suyun Hu. Design and evaluation of a small-scale multi-drum magnetorheological brake. *Journal of Intelligent Material Systems and Structures*, 29(12):2607–2618, 2018.

[86] Carlos Rossa, Adrien Jaegy, Alain Micaelli, and José Lozada. Development of a multilayered wide-ranged torque magnetorheological brake. *Smart Materials and Structures*, 23(2):025028, 2014.

[87] Huanhuan Qin, Aiguo Song, and Yiting Mo. Evaluation of a multi-drum magnetorheological brake via finite element analysis considering number of drums and fluid gap selection in optimization. *Journal of Intelligent Material Systems and Structures*, 30(5):778–787, 2019.

[88] Wan-Li Song, Dong-Heng Li, Yan Tao, Na Wang, and Shi-Chao Xiu. Simulation and experimentation of a magnetorheological brake with adjustable gap. *Journal of Intelligent Material Systems and Structures*, 28(12):1614–1626, 2017.

[89] Jung Woo Sohn, Han Gyeol Gang, and Seung-Bok Choi. An experimental study

on torque characteristics of magnetorheological brake with modified magnetic core shape. *Advances in Mechanical Engineering*, 10(1):1687814017752222, 2018.

[90] Mark R Jolly, Jonathan W Bender, and J David Carlson. Properties and applications of commercial magnetorheological fluids. *Journal of Intelligent Material Systems and Structures*, 10(1):5–13, 1999.

[91] Huanhuan Qin, Aiguo Song, and Yiting Mo. Performance evaluation of a hollowed multi-drum magnetorheological brake based on finite element analysis considering hollow casing radius. *IEEE Access*, 7:96070–96078, 2019.

[92] Huanhuan Qin, Aiguo Song, Zhan Gao, Yuqing Liu, and Guohua Jiang. A multi-finger interface with mr actuators for haptic applications. *IEEE Transactions on Haptics*, 11(1):5–14, 2017.

[93] Stuart A Bowyer, Brian L Davies, and Ferdinando Rodriguez y Baena. Active constraints/virtual fixtures: A survey. *Robotics, IEEE Transactions on*, 30(1):138–157, 2013.

[94] Russell H Taylor, Yong-yil Kim, Alan D Kalvin, David Larose, Betsy Haddad, Deljou Khoramabadi, Marilyn Noz, Robert Olyha, Nils Bruun, Dieter Grimm, et al. A model-based optimal planning and execution system with active sensing and passive manipulation for augmentation of human precision in computer-integrated surgery. In *Experimental Robotics II*, pages 177–195. Springer, 1993.

[95] Masamichi Sakaguchi, Junji Furusho, and Naoyuki Takesue. Passive force display using er brakes and its control experiments. In *Proceedings IEEE Virtual Reality 2001*, pages 7–12. IEEE, 2001.

[96] Davin K Swanson and Wayne J Book. Obstacle avoidance methods for a passive haptic display. In *2001 IEEE/ASME International Conference on Advanced Intelli-*

gent Mechatronics. Proceedings (Cat. No. 01TH8556), volume 2, pages 1187–1192. IEEE, 2001.

[97] Changhyun Cho, Munsang Kim, and Jae-Bok Song. Direct control of a passive haptic device based on passive force manipulability ellipsoid analysis. *International Journal of Control, Automation, and Systems*, 2(2):238–246, 2004.

[98] Mario Waldorff Gomes and Wayne John Book. Control approaches for a dissipative passive trajectory enhancing robot. Georgia Institute of Technology, 1997.

[99] Michael A Peshkin, J Edward Colgate, Wit Wannasuphoprasit, Carl A Moore, R Brent Gillespie, and Prasad Akella. Cobot architecture. *Robotics and Automation, IEEE Transactions on*, 17(4):377–390, 2001.

[100] R Brent Gillespie, J Edward Colgate, and Michael A Peshkin. A general framework for cobot control. *Robotics and Automation, IEEE Transactions on*, 17(4):391–401, 2001.

[101] Jinung An and Dong-Soo Kwon. Five-bar linkage haptic device with dc motors and mr brakes. *Journal of Intelligent Material Systems and Structures*, 20(1):97–107, 2009.

[102] Xin-Jun Liu, Jinsong Wang, and G Pritschow. Kinematics, singularity and workspace of planar 5r symmetrical parallel mechanisms. *Mechanism and machine theory*, 41(2):145–169, 2006.